

Solution Processed Low Dimensional Nanostructures for Optoelectronic and Photovoltaic Applications

**A Thesis Submitted to the AcSIR for the Award
the Degree of**

**DOCTOR OF PHILOSOPHY
In
CHEMICAL SCIENCES**



**By
Rounak Naphade
Registration Number: 10CC13A26030**

**Under the guidance of
Dr. Suresh Bhat
(Research Guide)
and
Dr. Satishchandra Ogale
(Research co-guide)**

**CSIR-NATIONAL CHEMICAL LABORATORY
PUNE – 411 008, INDIA**

Certificate

This is to certify that the work incorporated in this Ph.D. thesis entitled “**Solution processed low dimensional nanostructures for optoelectronic and photovoltaic applications**” submitted by **Mr. Rounak Naphade** to Academy of Scientific and Innovative Research (AcSIR) in fulfillment of the requirements for the award of the Degree of **Doctor of Philosophy in Chemical Sciences**, embodies original research work under my supervision. I further certify that this work has not been submitted to any other University or Institution in part or full for the award of any degree or diploma. Research material obtained from other sources has been duly acknowledged in the thesis. Any text, illustration, table etc., used in the thesis from other sources, have been duly cited and acknowledged.

Research Student

Rounak Naphade

Research Guide

Dr. Suresh Bhat

Research Co-guide

Dr. Satishchandra Ogale

Declaration

I hereby declare that the thesis entitled “**Solution processed low dimensional nanostructures for optoelectronic and photovoltaic applications**” submitted for the degree **Doctor of Philosophy** in Chemical Sciences to the Academy of Scientific & Innovative Research (AcSIR), has been carried out by me at the Physical and Materials Chemistry Division of National Chemical Laboratory, Pune under the guidance of **Dr. Suresh Bhat and co-guidance of Dr. Satishchandra Ogale**. Such material which has been obtained by other sources has been duly acknowledged in this thesis. The work is original and has not been submitted in part or full by me for any other degree or diploma to other University.

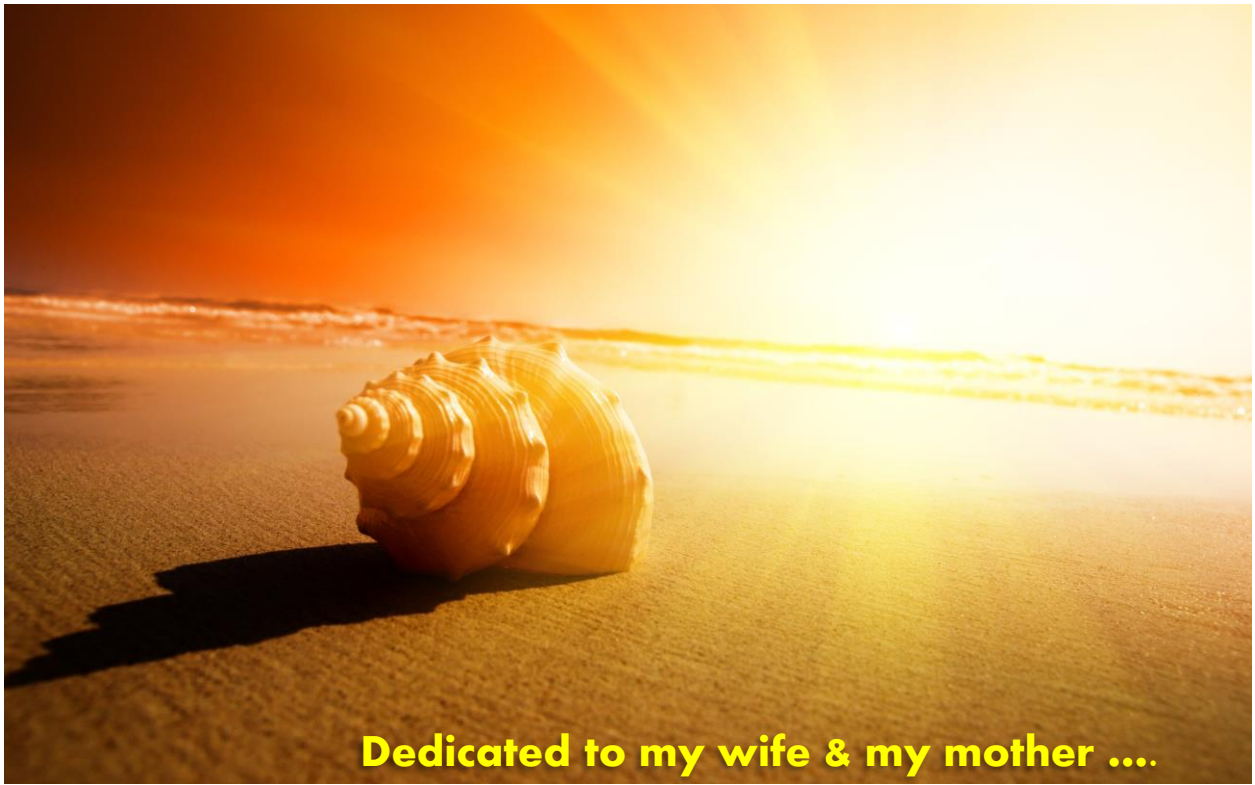
Date: 29th July 2016

Rounak Naphade

National Chemical Laboratory,

(Research Student)

Pune - 411008



Dedicated to my wife & my mother ...

Acknowledgements

This stage in my life would not have been possible without support and blessings of so many people. At this moment, I express my deep sense of gratitude towards everyone who made this memorable for me.

First, I wish to express my deepest sense of gratitude to Dr. Suresh Bhat, my research guide, for accepting to guide my research and helping me along the way through all my difficulties with his insightful academic and technical guidance. His excellent human qualities and friendly approach were important for my development as an individual.

I would also like to sincerely thank my friend, philosopher and guide Prof. Satishchandra Ogale for giving me an opportunity to work in his dynamic lab environment. He has always been a constant source of motivation for me during my PhD tenure. His dynamic presence and ability to think beyond conventional thinking has always surprised me as a science student. He always encouraged me to explore the new scientific ideas and critically evaluated the significance of such ideas. Through the coffee sessions and our Saturday group meetings, I have nurtured my scientific and professional skills. His constant support with endless patience has helped me during my whole PhD tenure. His personal excitement about science is a viral feeling, which will stay with me throughout my life.

I would also like to thank Dr. Mrs. Jyoti Jog for giving me the opportunity to start my research at NCL. I greatly appreciate the insights she provided in various studies, particularly in the areas of polymers and their nanocomposites and electrospinning process. I wish to express my heartfelt gratitude to her for her warm and friendly support throughout this journey.

I would like to acknowledge various funding agencies, namely the Department Biotechnology (DBT, and Council of Scientific & Industrial Research (CSIR) for research fellowships.

Further, I wish to thank Dr. S. Sivaram, (former Director of CSIR-NCL), Dr. Saurav Pal, (former Director CSIR-NCL), Dr. Ashwini kumar Nangia (Director, NCL), Dr. Anil Kumar, HOD, Physical and Materials Chemistry Division, and the former as well as

current HODs of the Polymer Science Division for the opportunity to work at CSIR-NCL and providing the infrastructure and research facilities. I sincerely thank my Doctoral Advisory Committee (DAC) members, Dr. P.P.Wadgaonkar, Dr. M.V. Badiger and Dr.V.Ravikumar for their timely discussions, guidance, and evaluations during my course work.

The technical and non-technical staff of the Polymer Science and Engineering and Physical Materials Chemistry divisions has also been very helpful.

I take this opportunity to thank Prof. Nitin Padture and Dr. Yuanyuan Zhou for their help in scientific discussions and manuscript preparations. I am also thankful to Dr. Rohan Fernandes and Dr. D.C.Kothari from Mumbai University for helping me in XPS characterizations.

I wish to further express my thanks to the student academic office staff for their constant help and guidance in throughout my course work at AcSIR. My very sincere thanks are also due to Dr.C.G.Suresh (former DAC chairman), Dr.C.J.Gadgil (DAC chairman), Mrs. Puranik, Mrs. Kolhe and Ms. Vaishali for the help and co-operation throughout this period. I also greatly admire the efficiency of the Deans of AcSIR (headquarters) and their staff.

I would like to acknowledge my coworkers and friends Dr. Rajesh Hyam, Dr. Tushar Jagdale, Dr.Anup Kale, Dr. Abhimanyu Rana, Dr.Vivek Dhas, Dr.Subas Muduli, Dr.Prasad Yadav Dr.Parvez, Dr.Mandakini, Dr.Lily, Dr.Datta, Dr.Meenal, Dr.Shruti, Dr.Abhik, Dr.Rohan, Dr.Onkar, Dr. Sarika Phadke, Dr. Shraddha, Dr. Anil, Dr. Dhanya, Dr. Pradeep, Dr. Satish, Aniruddha, Vishal, Satywan, Yogesh, Wahid, Umesh, Sambhaji, Nilima, Supriya, Mukta, Divya, Pooja, Poonam, Srashti, Ishita, Swati, Shreya for their support and for creating a wonderful laboratory environment. They all have been very helpful and friendly.

I would like to acknowledge Dr. Aditya Sadhanala and Ms. Emily from Cambridge University for helping me in my research work along with hosting us in my recent trip.

I take this opportunity to thank all my teachers from my primary school till my Master's degree for imbibing good values and knowledge in me.

I wholeheartedly thank my family Aai, Baba, aatya, dada, Vahini, for their unconditional love, constant support and for allowing me to pursue my ambitions. I would like to take this opportunity to thank my in-laws, Nilesh, Prajakta for keeping faith in me and offering their unconditional support with great patience. Without their positive support pursuing PhD after being married would have been a distant dream for me.

In the end a big thank you to my soul mate, Dipti. Without her patience and sacrifice this would never have been possible. In all these years she stood next to me, with me in some difficult situations but finally we have managed to reach at this point of life which we have dreamt together. During this process, she has been a real strength for me. Big thank you for gifting us our little bundle of joy 'Vihaan'. Thank you so much for being there for me all the time.

Finally a big thank you to almighty god for taking me and teaching me all the way through this.

Rounak Naphade

List of Abbreviations

1-D	One-Dimensional
2-D	Two-Dimensional
AM	Air Mass
AFM	Atomic Force Microscopy
BHJ	Bulk Heterojunction
CB	Conduction band
DRS	Diffuse Reflectance Spectroscopy
DSSCs	Dye sensitized solar cells
EIS	Electrochemical Impedance Spectroscopy
FE SEM	Field emission scanning electron microscopy
FTO	Fluorine doped tin oxide
FWHM	Full width half maximum
FF	Fill Factor
ITO	Indium doped Tin Oxide
J _{sc}	Short Circuit Current Density
J	Current Density
HR TEM	High resolution transmission electron microscopy
HOMO	Highest Occupied Molecular Orbital
HTM	Hole transporting material
IPCE	Incident photon-to-current conversion efficiency

ITO	Indium doped Tin Oxide
LH	Light harvesting
LHE (λ)	Light harvesting efficiency at wavelength λ
LUMO	Lowest Unoccupied Molecular Orbital
LED	Light Emitting Diodes
NF	Nanofibers
PL	Photoluminescence
PLD	Pulsed laser deposition
PEC	Photo-electrochemical
PV	Photovoltaic
P _{max}	Maximum power
SAED	Selected Area Electron Diffraction
SEM	Scanning electron microscopy
TCO	Transparent Conducting Oxide
TEM	Transmission electron microscopy
TTIP	Titanium tetraisopropoxide
UV	Ultraviolet
VB	Valence band
V _{oc}	Open circuit potential
XPS	X-ray photoelectron spectroscopy
XRD	X-ray diffraction

Content

Abstract	I-II
Chapter 1 Introduction	1-45
1.1 Energy: The New Research Frontiers	2
1.2 Types of renewable energy sources	4
1.2.1 Wind Energy	4
1.2.2 Hydropower	5
1.2.3 Geothermal Energy	6
1.2.4 Biomass and Biofuels	7
1.2.5 Solar Energy	8
1.3 Solar Photovoltaics	9
1.3.1 Generations of solar cells	10
1.3.2 Classic Silicon Solar cells	11
1.3.3 Thin film Solar cells	12
1.3.4 Organic/Hybrid Solar cells	13
1.4 Dye Sensitized Solar cells (DSSC)	15
1.4.1 Working principle	16
1.4.2 Basic components of DSSC	17
1.4.3 Performance parameters of DSSC	18

1.4.4 Kinetics of charge carriers in DSSC	21
1.5 Light Harvesting in DSSC	22
1.5.1 Light Scattering layer	23
1.5.1.1. Rayleigh Scattering	24
1.5.1.2. Mie Scattering	25
1.5.2 Use of nanostructures as light scattering agent	26
1.6. Introduction of Organic Inorganic Hybrid Perovskite semiconductors	27
1.6.1 Three dimensional perovskites (3D)	28
1.6.2 Two dimensional perovskites (2D)	30
1.6.3 Zero dimensional perovskites (0D)	33
1.7. Applications of Hybrid perovskites	33
1.7.1 Hybrid perovskites in solar cells	34
1.7.2 Hybrid perovskites in light emitting diode	35
1.8. Lead free perovskites	36
1.9. Plan for the thesis.	37
1.10 References	38

**Chapter 2 Experimental Methods, Characterization Techniques
and Device Fabrication 46-72**

Section I

Introduction	47
--------------	----

2.1 The electrospinning technique	47
2.2 Electrospinning	47
2.2.1 History of Electrospinning	49
2.2.2 Electrospinning process & working mechanism	50
2.2.3 Aligned nanofibers	50
2.2.4 Core shell electrospinning	51
2.2.5 Factors affecting electrospinning	52
2.2.6 Electrospaying process	53
2.2.7 Applications of electrospinning technology	54
2.3 Spin Coating	55

Section II

Characterization Techniques	56
Introduction	56
2.4 X-ray Diffraction (XRD)	56
2.5 UV-visible absorption spectroscopy	58
2.6 Photoluminescence (PL) spectroscopy	59
2.7 Microscopy techniques	60
2.7.1 Transmission electron microscopy (TEM)	60
2.7.2 Scanning electron microscopy (SEM)	61
2.7.3 Atomic force microscopy (AFM)	62
2.8 Raman spectroscopy	63

2.9 X-ray photoelectron spectroscopy (XPS)	65
2.10 Photothermal deflection spectroscopy (PDS)	66

Section III

Fabrication of Dye sensitized solar cells (DSSC) and Light emitting diodes (LED)

Introduction	67
2.11 Fabrication of DSSC	67
2.11.1 Substrate cleaning	67
2.11.2 Preparation of working electrode	67
2.11.3 TiCl ₄ treatment	68
2.11.4 Dye sensitization	68
2.11.5 Counter electrode preparation	68
2.11.6 Electrolyte solution preparation	69
2.11.7 DSSC device assembly	69
2.12 Fabrication of light emitting diode	69
2.13 References	70

Chapter 3 Plasmonic light harvesting by dye sensitized solar cells by Au-nanoparticles loaded TiO₂ nanofibers. 73-101

3.1 Introduction	74
3.2 Experimental Section	76

4.4.2 MAPbI ₃ based layered 2-D perovskites grown with Oleylamine.	110
4.4.3 MAPbBr ₃ based layered 2-D perovskites grown with Oleylamine	116
4.4.4 MAPbI _(3-x) Br _x mixed halide layered 2-D perovskites grown with oleylamine.	118
4.4.5 X-ray photoelectron spectroscopy (XPS) studies.	119
4.5 Conclusion	121
4.6 References	122
Chapter 5 Hybrid perovskite films with highly enhanced optical and electrical properties by addition of quaternary alkyl ammonium salt	125-138
5.1 Introduction	126
5.2. Experimental Section	127
5.2.1 MAPbBr ₃ film formation	127
5.2.2 Light emitting diode (LED) device fabrication	127
5.3 General Characterization	128
5.4 Result and Discussion	128
5.5 Conclusion	135
5.6 References	135
Chapter 6 Summary and future scope	139-144
6.1 Summary	140
6.2 Future Scope	142
List of Publications	145

Abstract

Currently there is considerable research emphasis on the development of one dimensional or two dimensional optoelectronically interesting nanostructures in the field of photo-voltaic and optoelectronics. Functional inorganic oxides and organic-inorganic hybrid perovskites clearly offer a natural platform in this arena with an added advantage of solution-based low temperature processing. It is further desirable that such nanostructures show applicability in the existing device geometries with improved output characteristics. Solution processed routes to make functional semiconducting nanomaterials is an interesting aspect to explore as different dimensions of nanostructures can be synthesized and tested in the photo-voltaic and optoelectronic device platforms. The present thesis deals with topics in this domain of interesting research.

A brief explanation of the methodologies used is given below in each chapter.

In the first work, we have discussed the role of plasmonic light harvesting in dye sensitized solar cells (DSSC). Significant enhancement in the performance of DSSC was reported with the use of Au nanoparticles loaded TiO₂ nanofibers in the light harvesting layer. The presence of gold nanoparticles shows considerable improvements in light harvesting and the electrochemical properties of TiO₂ nanofibers. A remarkable enhancement in efficiency by 25% is achieved with the gold loaded TiO₂ as light harvesting layer as compared to 12% by only a TiO₂ NF layer. The IPCE and impedance study of these devices showed commensurate results. Using impedance study we have also demonstrated decrease in transport resistance and increment in chemical capacitance of DSSC solar cell. Systematic optical analysis revealed the role of surface plasmon polariton modes distributed at the nanoscale shottky junctions in Au –TiO₂ nanofibers.

In the second work, we have shown the use of modified liquid in liquid electrospray process in conjunction with anti-solvent solvent extraction for the synthesis of low dimensional quantum structures especially 2-D nanosheets of CH₃NH₃PbI₃ and CH₃NH₃PbBr₃ based layered perovskites. In this chapter we have also shown the successful formation of CH₃NH₃PbBr₃ based 0-D quantum dots. The optical properties of

these, as formed, colloidal nanostructures have shown the band gap tunability over the entire visible range. The structural and morphological characterization revealed the role of oleylamine additive as capping agent in $\text{CH}_3\text{NH}_3\text{PbBr}_3$ and as an intercalation agent in $\text{CH}_3\text{NH}_3\text{PbI}_3$ based nanostructures. We have also studied the compositional tailoring by mixing the as formed perovskite precursors before electrospraying. This has shown tunability in luminescence over a broad range of visible spectrum.

In the third work, we present a novel additive mediated recrystallization approach for making highly luminescent perovskite films with less electronic disorder. In this case we have used quaternary ammonium halide based salts as an additive which are dispensed on to the perovskite films during formation. These salts were mixed in anti-solvent which was compatible with the perovskite formation. Our results showed that additive treated films had 250 times higher luminosity as compared to untreated films. The additive treated films show less electronic disorder in terms of Urbach energy which was reduced from 38meV to 18meV. This significant decrement suggests that additive treated films possess good optoelectronic properties as compared to the untreated samples. The photoluminescence quantum yield was enhanced from 1% (for untreated film) to 30% (for additive treated). Further we have demonstrated the use of this approach to make light emitting diode (LED) applications. The LED's made using additive treated films showed external quantum efficiencies higher than 0.3% and narrow emission full width half maxima.

Chapter 1

Introduction

This chapter gives an overview of the current international renewable and clean energy challenges and highlights the adverse effects of the currently used polluting fuels on environment and health. The importance of the abundantly available solar energy vs other renewable energy sources is discussed in detail. The different ways of harnessing and utilizing solar energy are also explained in brief. Towards the end, progress in solar photovoltaics (PV) is described which includes all the three generations of solar cells (starting from mono crystalline silicon solar cells to dye sensitized solar cells up to the recently developed perovskite solar cells). The current state of the art PV technologies are discussed. Recently emerged field of hybrid perovskites has grabbed great attention due to interesting intrinsic properties of perovskites. The different types of perovskites and their use in light emitting diode applications are explained in brief. Finally, the presentation of the outline of current thesis concludes this introductory chapter.

1.1 Energy: The New Research Frontier

The human civilization and socio-economic progress of human society has made huge impact on the availability of sustainable energy. Development of industrial, residential, commercial and transport sectors cannot be achieved without energy. The betterment of human life and society needs adequate energy resources for the next few decades. As per the survey done till last decade, the per capita energy consumption and demand is increased by 40%.^[1] The overall expected rise in energy consumption will increase by 2.12 lakhs of terawatts by 2030.^[2]

Our current primary energy sources are mainly fossil fuels like natural gas, coal, oil etc as seen from **Figure 1.1**. These energy sources are formed by vary slow and gradual decomposition of natural contents such as dead plants and animals in earth crust. Hence faster depletion of such energy sources is the main problem facing current generations. For instance, the reservoir of coal will last only for another 100 years but natural gas and oil reservoirs will deplete in another 70 and 50 years respectively.^[3]

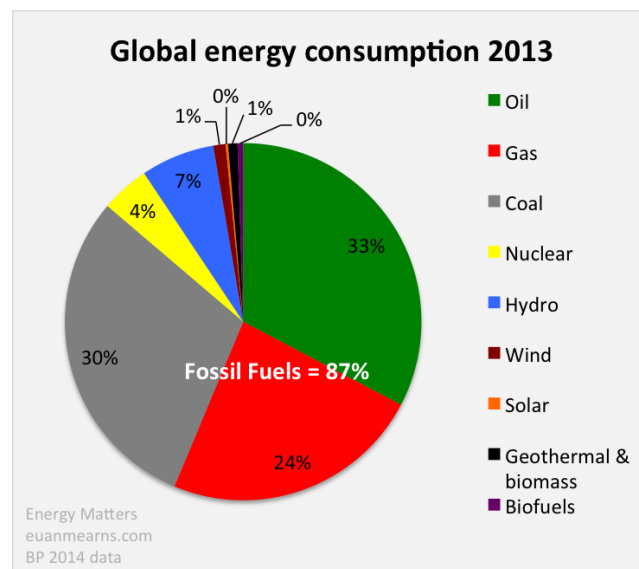


Figure 1.1 shows the global energy consumption

(<http://euanmearns.com/global-energy-trends-bp-statistical-review-2014/>)

However the human generations today are mainly dependent on such energy sources, the overuse of these sources are nowadays affecting the environment and surrounding creating enormous pollution. The electricity is mainly produced by burning the coal, similarly the overuse of automobiles and power plants releases the toxic gases into the environment such as CO₂, NO, CO, SO₂ which gives rise to serious health hazards as shown in **Figure 1.2**. In addition, suspended particulates cause air pollution. The nitrogen oxides and hydrocarbons can react to form tropospheric ozone, which is the major constituent of smog.

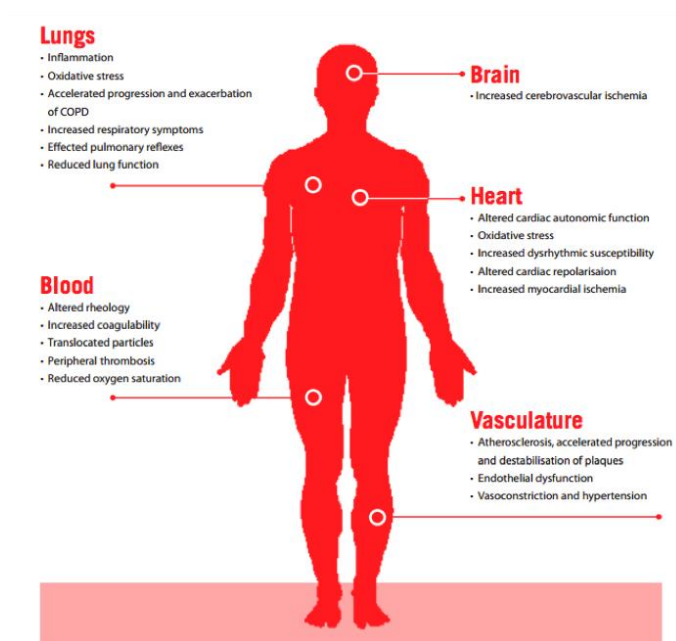


Figure 1.2 shows the health hazards of burning fossil fuels.

(<https://nwodniakenst.wordpress.com/>)

Release of such hazardous gases in environment has created the foremost critical issues such as global warming, sudden changes in climate, rising sea levels, melting of glaciers at poles which is causing frequent flood situations all over the world. In addition, depletion of ozone layer above the earth allows harmful UV rays to enter earth. This has led to serious health hazards over all the animal kingdom on the earth.^[4]

Thus to meet the increasing energy demands of future, we need to search for alternative energy resources. The major options include fossil fuel, nuclear power, and renewable energy. However, the use of fossil fuels inherently needs the secure storage of tons of CO₂ gas produced. Hence while managing the enhanced demands of energy, the damage to the environment has to be minimum.

Nuclear power is one viable option. However, we will need to construct 1GW (giga-watt) nuclear fission plant for the next 50 years on the earth. This seems next to impossible. Also, there are two important environmental concerns and potential negative impact for human health. This process involves radioactive products produced by nuclear fission inside power reactors and it requires careful disposal management. The other concern revolves around the making of nuclear weapons for mass destruction by various nations.^[5]

Renewable energy is a form of energy which can be derived from the available abundant sources such as from sun, wind, ocean, hydropower, biomass, geothermal resources, biofuels and hydrogen derived from renewable resources. Such energy sources are called as 'renewable' as they can be derived from natural resources which can be restocked in short time. Renewable energy resources are available in wide geographical areas, in contrast to other conventional energy sources. Rapid deployment of renewable energy sources would indeed result in significant energy security and economic benefits.

1.2. Types of Renewable Energy sources

The clean, green and low cost alternative of renewable energy sources includes, wind, hydro, biomass, geothermal and solar energy.

1.2.1 Wind Energy

Winds kinetic energy is utilized to rotate the wind turbines which further generate the electrical energy that powers up the either house or colony of houses in villages or hilly areas (**Figure 1.3**). This is the oldest and most explored renewable energy source. In this case the shaft is connected to a rotor which

rotates as per the wind speed. This generator then converts the kinetic energy of wind to the electrical

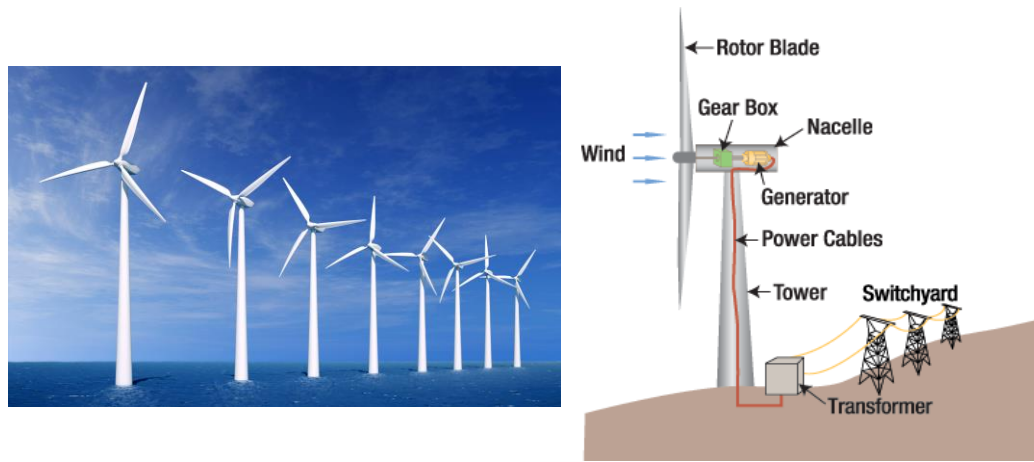


Figure 1.3 shows the schematic of electricity production from wind energy.

<http://energyinformative.org/windenergy>

<http://www.energynext.in/inox-wind-grabs-two-70-mw-wind-energy-projects/>

energy through application of electromagnetic field. This generated electricity is further converted in high voltages. It was first used to drive ships on the river Nile which is dated 7000 years ago. Today airflows are used to run wind turbines. Advanced wind turbine power range is from 600kW to 5 MW, but turbines with output power of 1.5–3 MW has been used for commercial purpose. Although this is greener route for energy production, earlier only 13% of electricity production was through wind energy route. But, in recent times this has expanded to 336GW.^[6] Around the globe Denmark is generating 40% of electricity from wind energy.^[7]

1.2.2. Hydropower

In Hydro-power the energy of falling water and running water is used to move turbines. The dams are established on the river side or by using back water of rivers. By this way the use of kinetic energy of falling water is used to rotate the high power turbines which ultimately convert the mechanical energy into

electrical energy.(**Figure 1.4**) This is the most acceptable renewable energy form; 16% of world energy production is achieved through this route. All the countries around globe are using hydroelectric power route for electricity production. China is a leading country with highest hydroelectricity producer at 721TW/hr. This is the most reliable approach for producing electricity. As this can be considered as the one time investment with less duration of payback time. In addition this is low cost and has no direct environmental pollution.^[8-9]

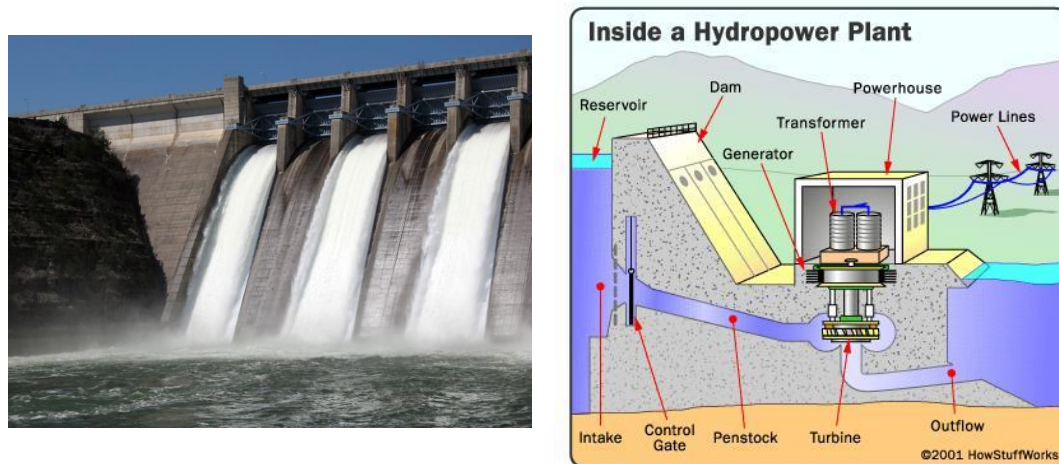


Figure 1.4 shows the schematic of hydropower production from running water.

<https://edinburghnapiernews.com/2012/03/05/mild-winter-boosts-hydro-power/>

<https://wiki.uiowa.edu/display/greenergy/Hydroelectric+Power>

1.2.3 Geothermal Energy

Geothermal energy is defined as the heat produced and stored in earth crust. This is also one of the renewable energy source. Many parts of the world such as United States (U.S), Indonesia, Philippines etc. In earth crust, 10^{31} joules of heat is stored which is 100 billion times of the today's world energy consumption. Country like Iceland is producing 50% of its electricity through geothermal power. In this case the steam of hot water and dry steam is allowed to flow through turbines to produce electricity. The concern about release of toxic gases

such as ammonia, carbon di-oxide (CO_2) and hydrogen gas (H_2). Such gases released from earth crust can have trace amounts of hazardous elements such as Arsenic, Antimony, Mercury etc.^[10]

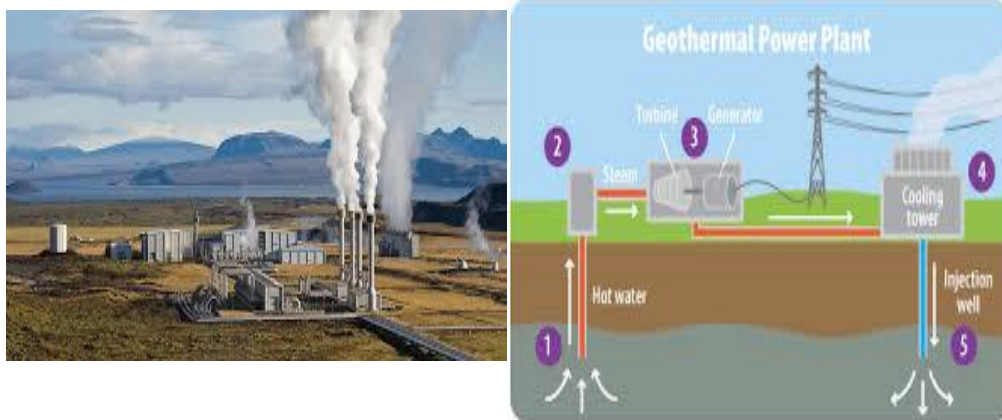


Figure 1.5 shows the electricity production diagram from geothermal energy.

<https://www3.epa.gov/climatechange/kids/solutions/technologies/geothermal.html>

http://www.ucsusa.org/clean_energy/our-energy-choices/renewable-energy/how-geothermal-energy-works.html#.V48gJ9R97Gg

1.2.4 Biomass and Biofuels:

Biomass is biologically derived material like wood, agricultural waste, animal and human waste etc. The energy from this biomass is called as ‘biopower’ as it has stored energy which can be released as heat. Wood is invariably the largest source of energy obtained from biomass. **Figure 1.6** shows the biomass resources and schematic of biofuel production from biowaste. The most conventional approach is direct combustion of wood to produce high pressure steam. The biomass is burnt in excess of air to heat water. This water is further converted into steam to run turbine. United State is producing 50 billion KW/hr from biomass. In particular U.S. is mainly emphasizing on growing crops like ‘switch grass’ and

‘bigblue stem’ which can be further harvested till 10 years. The grasses like sugar can and elephant grasses in wet and hot climates in India, Hawaii, and Florida.

The main advantage of using this renewable energy source is that it can be used to indirectly clean up the industrial, agricultural and municipal waste. The only drawback here is the initial investment in such power plants is very high. In addition biomass leads to emission of toxic gases in air. ^[11]

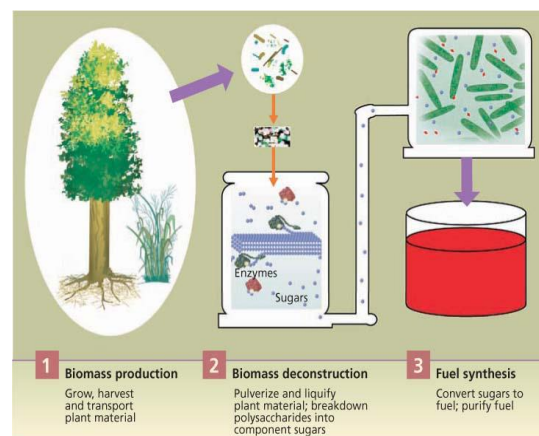


Fig. 1. Stages of converting biomass to biofuel. Images adapted from DOE Genome Programs (<http://genomics.energy.gov>).

Figure 1.6 shows the process of biofuel generation from biomass resources.

<http://www.biomassinnovation.ca/biomassandbioenergy.html>

<http://calag.ucanr.edu/Archive/?article=ca.v063n04p178>

1.2.5 Solar Energy

Among all the renewable energy options the most viable choice to meet our energy demand is solar energy as it is available in plenty and free of cost. The power of the sun striking the earth is 120,000 TW per annum. This abundant solar energy can be easily converted into useful electricity through light harvesting devices. Such devices can be classified as follows:

- ❖ Solar Energy to Electricity (Photovoltaic)
- ❖ Solar Energy to Solar fuel (H₂) (Photoelectrochemical water splitting)

- ❖ Solar based thermoelectric devices
- ❖ Solar heaters.

Current thesis mainly deals with the first topic of photovoltaic and in particular about solar light harvesting. The direction of the work here was to mainly emphasize on synthesizing the light harvesting agents which can be implemented in existing solar cell architectures to enhance the overall light to current conversion efficiency. The use of nanoscience and solar energy has combination that has made the rapid emergence of novel technologies. In the following sections the brief introduction of photovoltaics is discussed along with the basic working principle, fundamental issues, and challenges pertaining to these applications is presented.

1.3 Solar Photovoltaics

The idea of conversion of solar energy into useful electricity is emerged from the discovery of ‘Photo-voltaic effect’ observed by Becquerel in 1839.^[12] It was defined as ‘when light is shined on the interface between two solids or liquid systems the photo voltage is generated across the interface. Hence all the photo-voltaic devices are termed as p-n junction systems’.

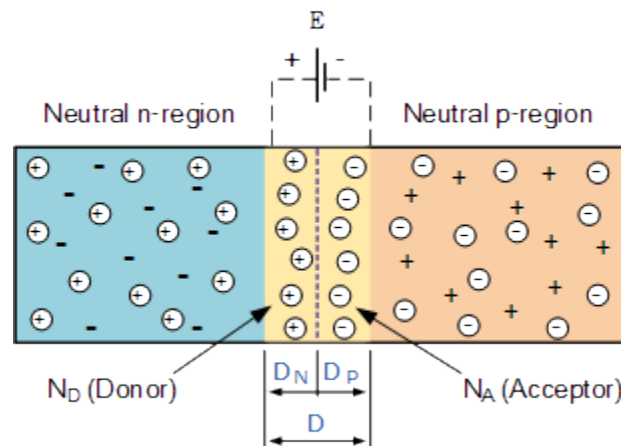


Figure 1.7 shows the p-n junction formation at the interface.

http://www.electronics-tutorials.ws/diode/diode_2.html

At such interface, the electrons from n-type semiconductor diffuses to p-type semiconductor and holes in vice a versa direction. This diffusion continues till the large number of charge densities is created across the interface. This is called as ‘built-in potential’. This built-in potential further expands and produces ‘potential barrier’ which is also called as ‘depletion region’. This is schematically explained in **Figure 1.7** In photo-voltaic solar cell, when light is incident on such interface, the free electrons and holes are created with in and around the depletion region. The built in potential at the interface, drives these charges in the opposite direction leading to a photo-voltage. In this case, the p and n junctions are connected to external load which carries the current.

The first practical demonstration of such concept was established in 1954 using silicon solar cells. This photo-voltaic device showed 6% power conversion efficiency.^[13] Further this concept and technology has been modified in several ways resulting in many generations of silicon solar cells. Non-silicon based approaches were also explored and developed over the years.

1.3.1 Generations of Solar cells

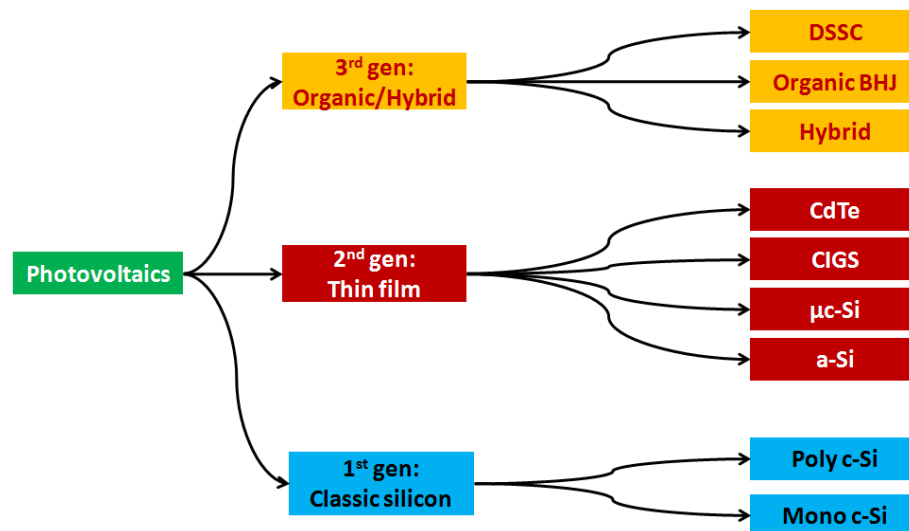


Figure 1.8 shows the development of Solar cell generations ^[14]

<http://www.heliatek.com/technologie/organische-photovoltaik/?lang=en>.

Figure 1.8 Shows the evolution and development of solar cell generations. To begin with in this section we will discuss the development of first and second generation solar cells in brief. However the current thesis deals with the third generation solar cells, hence the later part is covered in detail.

1.3.2 Classic Silicon Solar cells (First Generation)

90% of current electricity production through photo-voltaic devices comes from these first generation solar cells. These solar cells are single junction solar cells which are typically made either from single-crystalline (c-Si) or poly-crystalline (mc-Si) silicon wafers as shown in **figure 1.9**. These solar cells shows 18-20% power conversion efficiencies for c-Si and 12-14% for mc-Si ^[15] These type of solar cells are robust and most reliable and hence they dominate in current photo-voltaic device based business market. The main drawback is the availability of high purity silicon wafers. In addition the production of silicon wafers is extremely expensive. Hence the overall cost for these solar cells is very high and it affects the further expansion of this technology. This led the researchers to come up with new concept of solar cells which are called as ‘thin film solar cells’.

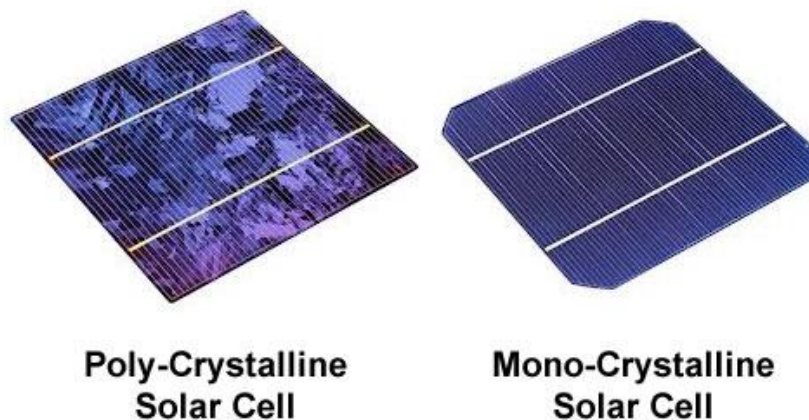


Figure 1.9 images of poly-crystalline and mono-crystalline silicon solar cells.

<http://www.tindosolar.com.au/learn-more/poly-vs-mono-crystalline/>

1.3.3 Thin Film Solar cells (Second Generation)

This type of solar cells utilizes amorphous silicon (a-Si). Cadmium telluride (CdTe). Copper indium gallium sulfides (CIGS) etc as shown in **figure 1.10**. Thin film solar cells are also single junction based devices. These materials are coated on to the low cost glass substrates and further exposed to solar radiations. These materials have better solar spectrum absorption as compared to silicon solar cells. These solar cells can work efficiently in poor light conditions. Till today, CdTe (20%),^[16] CIGS (20%)^[17] based thin film solar cells has shown promising photovoltaic conversion efficiencies. These materials can also be coated on to the flexible and light weight substrates for flexible device applications. Although evolution and development of this solar cells has reduced the cost up to some extent but on commercial scale still this materials lacks in producing high efficiency large area devices. The main problem is poor material reproducibility and uniform thin film formation over large active area. In addition, these materials are toxic and harmful to biological environment.

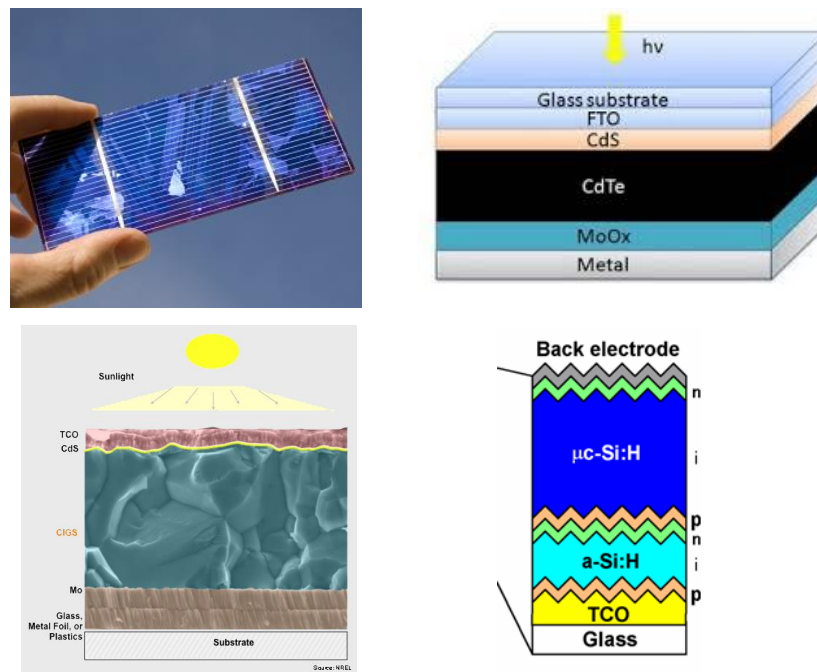


Figure 1.10 shows different classes of thin film solar cells.

<http://www.solar-facts-and-advice.com/CIGS-solar-cell.html>

http://www1.gifu-u.ac.jp/~solar/module_e.html

<http://www.che.rochester.edu/Projects/tanglab/research/cdte.html>

<http://phys.org/news/2011-03-laser-pulses-crystallize-amorphous-silicon.html>

1.3.4 Organic/Hybrid Solar cells (third generation solar cells)

This third generation solar cells are mainly multi-junction solar cells. These solar cells use either organic materials (polymers, small molecules etc.) or organic materials in conjunction with the inorganic materials for photo-voltaic device fabrication. Hence this generation solar cells are either called as ‘organic solar cells’ or ‘hybrid solar cells’. The main advantage of these solar cells is that, they are inexpensive and can be easily adopted in flexible device technology.^[18]

Figure 1.11 shows the layer by layer architecture and bulk heterojunction type organic solar cells.

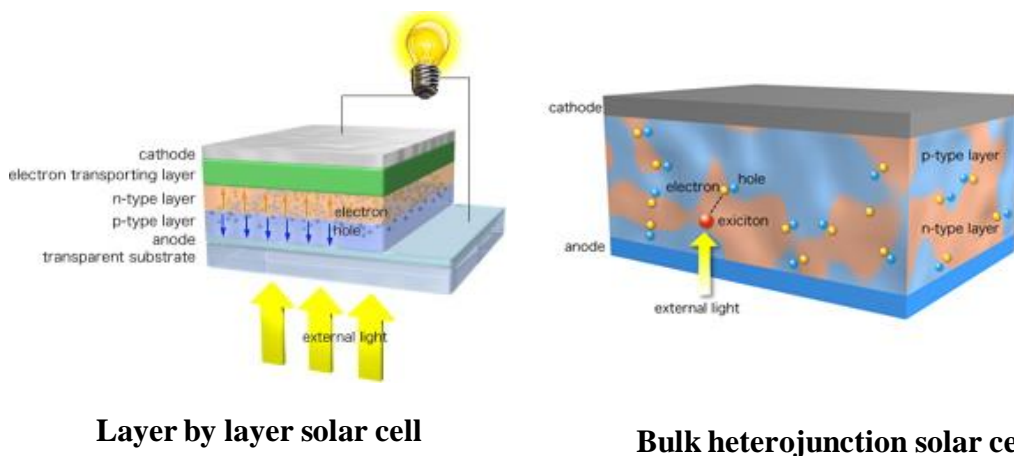


Figure 1.11 shows the layer by layer and bulk heterojunction architecture of organic solar cells.

http://www.cstf.kyushu-u.ac.jp/~adachilab/lab/?page_id=3927

The development of organic solar cells is described here in brief. The single layer organic solar cell was made by sandwiching photo-active polymer (PPV) between two conducting electrodes (ITO and Al). Under sun light illumination, the exciton is separated at the two electrodes due to difference in their work function. This

solar cell gave 0.1% conversion efficiency.^[19] Similarly, bilayer organic solar cells were also explored by making bilayer of PPV and C₆₀ molecule as electron donor and electron acceptor respectively. This type of solar cells showed 1% efficiency.^[20] The main reason for low efficiency is the short diffusion length of charge carriers which leads to excess of recombination. Further the third approach, bulk heterojunction (BHJ) solar cell was introduced. In this case, the electron donor and electron acceptor are mixed together to form a blend. The constitution of blend is appropriately chosen such that, the diffusion length of exciton matches well with the thickness of photo-active layer. In this case, due to favorable work functions of conducting electrodes, the electron and holes are pulled in the opposite direction generating photo-voltage and current. A very good example of BHJ solar cell is Spiro-OMeTAD as hole transport medium and Silicon nanorods as electron transporter with a power conversion efficiency of 10.3 %^[21]

In addition to organic photovoltaics, in this generation hybrid solar cells were also developed in which both organic and inorganic semiconductors are simultaneously used for making multi-junction solar cells. In this case, the organic part is conjugated polymers, dyes etc which mainly absorbs the solar radiation and transports the holes while the electron transport occurs mainly through inorganic part. These hybrid solar cells are mainly classified as : Polymer solar cells, Dye sensitized solar cells (DSSC) and Quantum dot solar cells (QDSC). Polymer solar cells mainly involve the photo-active polymers such as P3HT, MEH:PPV etc which has extended conjugation.^[22] These polymers are also mixed with quantum dots such as CdS, CdSe etc. to produce hybrid solar cells termed as 'polymer-nanocomposite solar cells'. Such nanocomposite approach helps in better charge transfer processes. Amongst this third generation technologies of solar cells, the Dye sensitized solar cells stand out the most promising technology for their unique device architecture and the major part of current thesis deals with the architectural modifications of DSSC solar cells. The DSSC technology is discussed in more details in next sections.

1.4 Dye Sensitized Solar cells (DSSC)

This is one of the most popular third generation solar cells as it is the most efficient technology at a low cost. In early 90's the sensitization of wide band gap semiconductors were very popular in terms of charge transfer process investigations. This basic idea was converted into the real device by a seminal publication which was published in Nature in 1991 by Brian O' Regan and Michael Gratzel.^[23] In this report, they have showed the use of porous TiO₂ film sensitized with the dye molecules as an electrode for solar cells. Due to high porosity the large surface area was available for dye adhesion and which lead in tremendous enhancement in the photocurrent. In this report, the authors have managed to show the 7.1% power conversion efficiency which later pushed to 13%^[24] by collective efforts. Over the year the device architecture is also been improved. These solar cells have also shown remarkable performances on large area applications as well.

1.4.1 Working Principle:

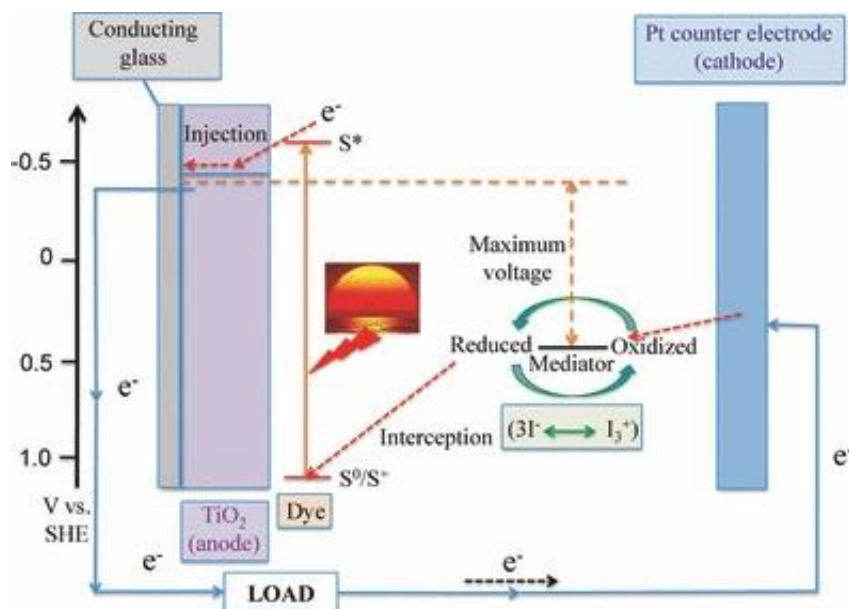


Figure 1.12 shows energy level diagram of DSSC. Reprinted with permission from ref. no. 25

In this device architecture, there are two electrodes viz photo-anode (Working electrode) and photo-cathode (Counter electrode) as shown in the **Figure 1.12**. The working electrode comprises the metal oxides such as TiO_2 , ZnO and SnO_2 based nanoparticles film coated onto the transparent conducting oxide (TCO). This film is further loaded with dye molecules which are used as sensitizers. The counter electrode is platinum coated on TCO. These two electrodes are pressed together and liquid electrolyte is poured in between which helps to access the holes in external circuit. In principle, when light is irradiated on DSSC, the dye molecules absorb solar radiation and gets excited, this result in transfer of electron from HOMO of dye molecule to LUMO. Later the excited electron is transferred to the conduction band of TiO_2 on to which these dye molecules are anchored. Further this injected electron from dye molecule to TiO_2 follows a diffusion mechanism and gets transferred to the TCO through TiO_2 nanoparticles. Meanwhile, the oxidized dye molecule gets regenerated by electron which is supplied by redox couple of iodine/triiodide species of electrolyte.

1.4.2 Basic components of DSSC:

The architecture of DSSC is shown in **figure 1.13**. It consists of several components as follows

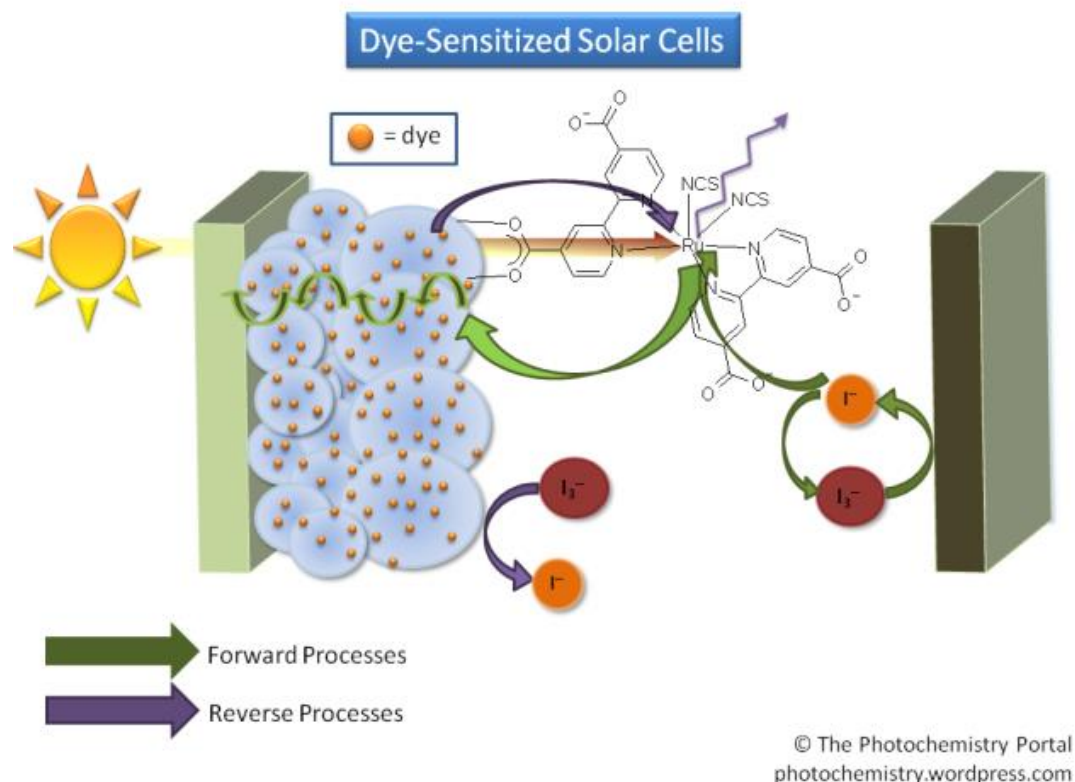


Figure 1.13 schematic architecture of DSSC.

<https://photochemistry.wordpress.com/2009/08/17/dye-sensitised-solar-cells-dssc/>

- **Transparent conducting Oxide (TCO) substrates:** Fluorine doped tin oxide (FTO) coated glass is widely used as the TCO for DSSC fabrication. Such glass substrates offer very low sheet resistance of 10-15Ω/cm with the visible light transparencies greater than 70%. This substrate is also used for counter electrode formation.
- **Working Electrode:** working electrode is devised by coating 10-15μm thick porous metal oxide (for e.g. TiO₂) nanoparticle film. Different morphologies of TiO₂ such as one dimensional nanofibers, nanowires, nanorods, nanotubes and two dimensional nanosheets have great potential

for high performance DSSCs.^[26] In addition, metal oxides such as ZnO and SnO₂ have also been used as working electrodes.^[27-28]

- **Sensitizers:** The dye molecules used here should be able to absorb light over a entire visible spectrum. Working electrode is dipped in dye solution for dye anchoring. Standard dyes used for high efficiency solar cells are N719 and N3.^[29]
- **Counter electrode:** It is generally platinum nanoparticles coated FTO substrate. Other materials such as functionalized graphene,^[30] carbon nanofibers,^[31] sulfides, carbides^[32] conducting carbon cloth^[33] have also been explored as counter electrode.
- **Electrolyte:** It is a redox couple dissolved in organic solvents which is used to regenerate the oxidized dye molecules. Iodide/triiodide (I⁻/I₃⁻) is used as electrolyte for DSSC which gives very low fundamental energy loss.^[34] Variety of other redox couples such as Br⁻/Br₃⁻, SCN⁻/(SCN)₂, SeCN⁻/(SeCN)₃⁻, and Co(II)/Co(III) complex.^[35]

1.4.3 Performance parameters for DSSC

In this section, we have discussed the important parameters that characterize the photo-voltaic performance of DSSC. A typical J-V curved obtained during DSSC measurement is shown in **figure 1.14**

- Open Circuit Voltage (V_{oc}) :

This photo-generated voltage is the difference between the Fermi level of TiO₂ and the electro-chemical potential of the electrolyte. The mathematical expression for V_{oc} is given as

$$V_{oc} = E_{CB}/q + kT/q \ln (n/N_{CB}) - E_{redox}/q \quad (\text{Volts})$$

Where E_{CB} is the conduction band edge energy for TiO₂. 'n' is the concentration of injected electrons in TiO₂. E_{redox} is the redox potential of electrolyte used. Therefore we can conclude that, the maximum Voc is DSS is mainly dependant on the dye molecule absorbance as it decides the value of 'n'. The semiconductor

quality of TiO_2 will be functional in deciding the value of trap state density (N_{CB}). Experimentally V_{oc} can be measured by measuring the potential difference between working and counter electrodes when cells are illuminated under sunlight. The condition of infinite load is considered between two electrodes when no current flows in external circuit. It can also be obtained by taking X - intercept of J-V curve.

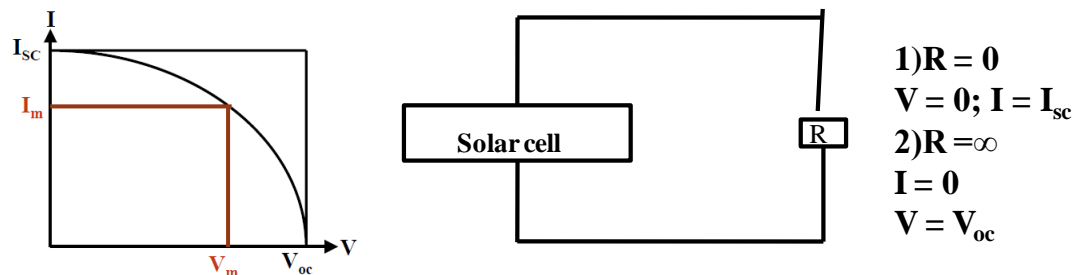


Figure 1.14 shows the J-V curve and parameters of solar cell characterizations.

- Short circuit current density (J_{sc}) :

This condition is achieved at zero load resistance between working and counter electrode under illumination. It is the Y-intercept of J-V curve. The J_{sc} values are mainly dependent of the spectral response of sensitizers. J_{sc} is majorly affected by the side reactions taking place in the solar cells under illumination such as recombination, back electron transfer, slow diffusion of electrons etc. Therefore dye designing with the appropriate HOMO-LUMO levels and maximum visible light absorption coefficients is the ongoing research area in DSSC.

- Fill Factor (FF):

It is the ratio of maximum power output from solar cells to the product of open circuit voltage (V_{oc}) and short circuit current density (J_{sc}). The fill factor can be expressed as

$$\mathbf{FF = V_{\text{max}} * I_{\text{max}} / V_{\text{oc}} * I_{\text{sc}}}$$

V_{max} and J_{max} can be obtained by the maximum power point on J-V curve of solar cells. The fill factor represents the degree of rectangular nature of J-V curve. Fill factor of solar cells is also dependent on two important factors viz series resistance (R_{sc}) and shunt resistance (R_{SH}). The series resistance is obtained by the sheet resistance of TCO, bulk resistance of solar cells and contact resistance. Hence as the R_{sc} value increases the J_{sc} and V_{oc} values drops down which in turn affects the overall fill factor. The series resistance can be calculated by taking the reciprocal of slope of J-V curve at V_{oc} condition. The recombination of charges leads to loss of photo-current; the resistance to this recombination is called as shunt resistance. (R_{SH}). The resistance to recombination of photo-generated charge carriers should be as high as possible in order to achieve maximum power conversion efficiency. R_{SH} can be obtained by taking the inverse of slope on J-V curve at J_{sc} condition.

- Efficiency:

Mathematically it is the ratio of maximum obtainable power from DSSC to the input solar radiations power.

$$\text{Efficiency (\%)} = (V_{oc} * I_{sc} * FF) / P_{in}$$

The standard condition for the efficiency measurement of DSSC is under AM1.5 Global solar irradiance (100mW/cm²) and at a temperature of 25⁰C.

- Incident Photon to current conversion efficiency (IPCE):

The incident photon to current conversion efficiency measures the efficiency of solar cells in terms of producing photo-generated charge carriers at a given wavelength over the It is the numeric ratio of incident photons to the no of charge carriers generated as a function of excitation wavelength.

The mathematical expression for IPCE is given as,

$$IPCE(\lambda) = 1240 * J_{sc} / \lambda * \Phi$$

J_{sc} is the short circuit current density (mA/cm^2), λ is the excitation wavelength (nm) and Φ is the incident radiation flux (W/m^2). In the case of DSSC this term can be defined as,

$$\text{IPCE}(\lambda) = \text{LHE}(\lambda) * \Phi(\text{inj}) * \eta(\text{coll})$$

Where $\text{LHE}(\lambda)$ is defined as the light harvesting efficiency of photons at a given wavelength (λ), $\Phi(\text{inj})$ is the electron injection efficiency of the excited dye molecules to the oxide conduction band and $\eta(\text{coll})$ is the fraction of injected charges to the total number of excited charges which are successfully reached to the back contact.

1.4.4. Kinetics of charge carriers in DSSC

Under illumination, the kinetic competition between the carrier generation and its recombination decides the efficiency of solar cells. At different time scales, various photo generated processes takes place in solar cells. The kinetics of various processes is shown in **figure 1.15**.

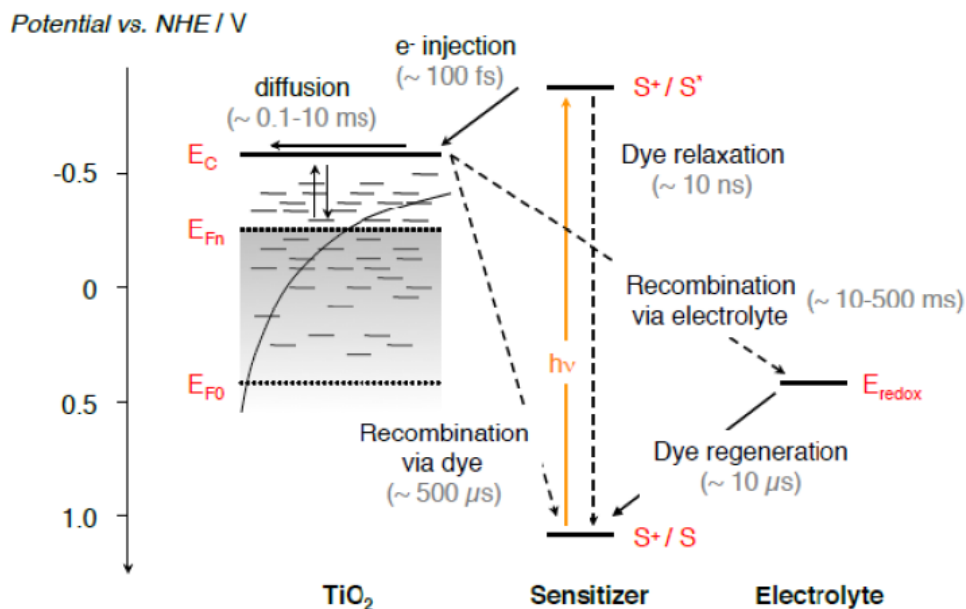


Figure 1.15 kinetic of various processes involved in DSSC. Reprinted with permission from ref no. 36

From this figure we can see, upon illumination, the dye molecules gets excited and injects the photo-excited electrons in the CB of TiO₂. This process takes about 100 femtoseconds. Further the dye molecules gets relaxed in few tens of nanoseconds and the regeneration of dyes occurs within few microseconds. Thus the electron injection is a faster process compared to regeneration of dyes which mainly avoids recombination of photo generated charge carriers. The injected electron in TiO₂ has to travel the whole thickness before reaching to an electrode. It has been demonstrated that, the injected electrons pass through TiO₂ by the diffusion mechanism.^[37-38] Hence the electron transport to the conducting electrode is a very slow process and hence it is mainly called as rate determining step. These injected electrons face many resistances in terms of surface states, grain boundaries of TiO₂ matrix. In addition to this, the recombination of charge carriers is also one of the major drawback for high performance DSSC. To overcome these drawbacks one dimensional nanostructures such nano-rods, nanofibers, nanotubes or nanoneedles kind of morphologies of metal oxides needs to be explored.^[39] In case of such one dimensional (1D) nanostructures electron diffusion length can be increased much higher than the nanoparticles. In addition, such 1D nanostructure has lower number of grain boundaries and defects as compared to nanoparticles which facilitates the electron transport and reduces the interfacial recombination.

1.5 Light Harvesting in DSSC

This section briefly explains the modifications in the device architectures of DSSC in order to enhance the overall light trapping inside the device. The ability to trap the light efficiently enhances the overall performance of the DSSC.

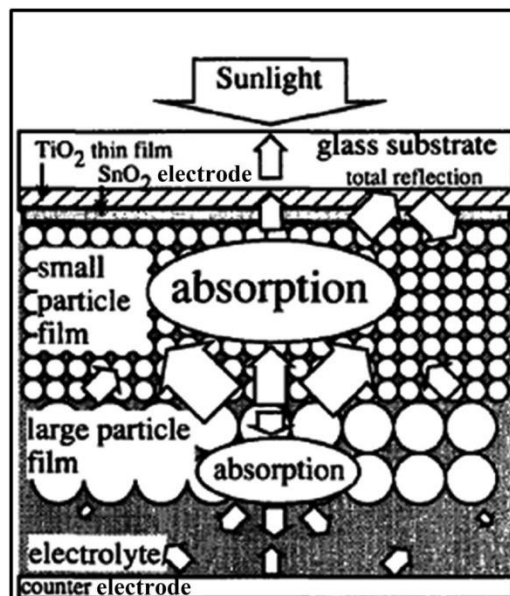


Figure 1.16 shows the double layer structure of DSSC. Reprinted with permission from ref no 41.

As mentioned in **figure 1.16** the first thin layer coated on to the TCO is called as electron blocking layer which prevents the back contact of liquid electrolyte with conducting electrode. On top of that, the mesoporous layer of TiO_2 nanoparticles of about 15-20 nm is coated. The thickness of this layer is about 12-15 μm . The formation of this layer is very crucial as it mainly governs the overall performance of DSSC. The third layer coated on top of mesoporous layer is usually called as ‘light scattering/harvesting layer’ which is made up of either bigger sized TiO_2 nanoparticles (up to 400 nm) or other structural morphologies of TiO_2 such as , nanofibers, nanoflowers, nano-beads, nano-leaves etc. This configuration of DSSC is called ‘double layered structures’.^[40] This type of architectures is mainly shown to improve the overall photocurrent of the device.

1.5.1. Light Scattering layer

As the efficiency of DSSC is mainly dependent on the efficient trapping of light inside the device; the engineering in the device architecture of DSSC was implemented firstly by Akira Usami et al.^[41] wherein they demonstrated the use of larger TiO_2 nanospheres as light scattering layer. The importance of such layer is

that it can interact with the visible light and can trap the light efficiently inside the mesoporous layer of TiO₂. This increases the overall path length of light inside the device resulting in more absorption of light by dye molecules. In scale up of DSSC based devices, the decrease in the overall efficiency is a big challenge hence implementation of light harvesting layer is an effective and practical approach

Light is a form of energy which has dual particle and wavelike nature. Scattering of light is defined as a process in which the light is redirected when it encounters an obstruction. Based on this approach the light scattering process is fundamentally classified into two theoretical approaches such as Rayleigh scattering and Mie scattering.

1.5.1.1. Rayleigh Scattering theory:

This theory was formulated by the British physicist Lord Rayleigh. This theory describes the elastic scattering of light (electromagnetic radiation) by non-absorbing spherical particles which are much smaller in dimensions than the incident wavelength. This is an elastic scattering process hence it does not affect the state of matter after scattering. This type of scattering is predominately observed in the gases. In elastic scattering process, the frequency of scattered light is similar to the incident radiation. In Rayleigh scattering the scattering cross section (σ) is given as $\frac{2\pi r^6}{\lambda^4}$ where 'r' is particle radius and ' λ ' is the scattering wavelength.

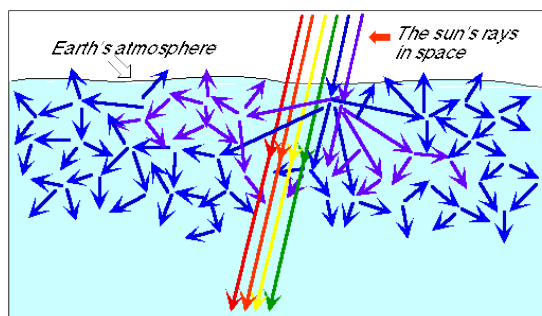


Figure 1.17 shows the blue color sky and the schematic process of Rayleigh scattering

Rayleigh scattering of sun light due to tiny dust particles in the atmosphere is the main reason for blue color of the sky. In atmosphere the randomly located particles interact with the sun radiations, the Rayleigh scattering cross section is inversely proportional to the fourth power of wavelength. (λ^{-4}) Which means the short wavelength will scatter more as compared to the longer wavelength in the solar spectrum. Due to ozone layer, the UV component of the solar spectrum gets absorbed in the outer sphere. Hence among the visible spectrum blue light scattering cross section is very high. This is the main reason sky appears like blue. This phenomenon is successfully used optical fibers based technology.

1.5.1.2. Mie Scattering theory:

Mie theory is used for explaining the light scattering behavior from particles of materials which either absorb light or non-absorbing in nature. When the particle size becomes larger i.e. around 10% of the incident radiation wavelength then the Rayleigh theory does not come into account. Mie theory is applied to find the intensity of scattered radiation when the particle sizes are comparable to the incident wavelength. The solutions to find Mie scattering efficiency is given by

$$Q_{\text{scattering}} = \frac{(\sigma)_{\text{scattering}}}{\pi r^2}$$

Where (σ) scattering is mathematical function denoted as

$$\sigma_{\text{sct}} = \sum_{n=0}^{\infty} (2n + 1) (|a_n|^2 + |b_n|^2)$$

Where a_n and b_n mathematical functions.

The application of these mathematical solutions has later helped in understanding various forms of materials such as biological tissues, latex paints, colloidal systems like milk, metamaterials etc. This theory is used to optically characterize the normal tissue cells and cancerous tissue cells.

1.5.2 Use of nanostructures as light scattering agent:

Hore et al demonstrated the very novel aspect of creating the scattering centers inside the TiO₂ film for efficient light harvesting in solar cells. They have shown the use of Polystyrene beads as sacrificial layer inside the TiO₂ paste. Upon sintering these beads was melted and the spherical voids were created inside the mesoporous TiO₂ film matrix. Such voids act as good light scattering sites resulting in overall 25% enhancement in the solar cell efficiencies.^[42] Similarly later use of TiO₂ nanowire-nanoparticle composites, nanofiber-nanoparticle composites was also explored.^[43-44] Inclusion of such one dimensional TiO₂ nanostructures have shown better light scattering abilities. P. Joshi et al has shown that the combination of TiO₂ nanofibers and TiO₂ nanoparticles results in enhancement of the light harvesting ability of the photo anode without sacrificing the dye loading.^[45] Later various groups have worked on different TiO₂ morphologies in order to achieve high performance DSSC. Nakayama et al showed use of electrophoretically deposited TiO₂ nanotubes as light scattering agent and achieved 7.53% overall efficiency.^[46] Introduction of corn like TiO₂ nanowires also resulted in 7.1% efficiencies for solar cells.^[47] Yoshikawa et al used electrospun 1D TiO₂ nanofibers as light scattering agent and an efficiency of 8.14% was reported on 0.25cm² active area.^[48]

In present thesis, we have mainly emphasized on the light harvesting aspect of DSSC by incorporating one dimensional nanofibers of TiO₂ and gold loaded TiO₂ nanofibers.

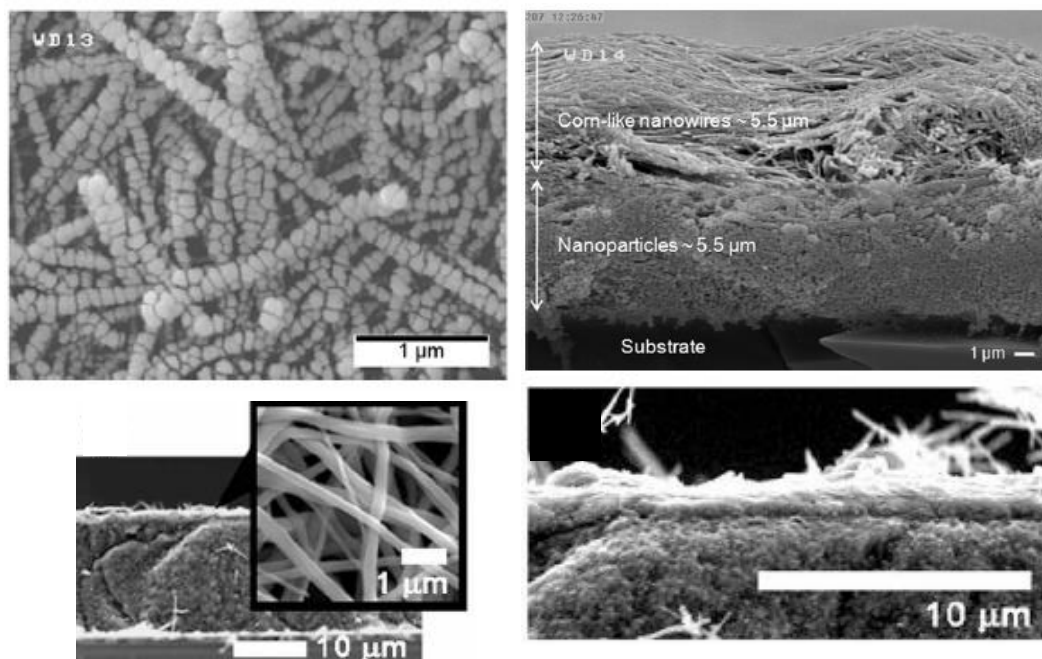


Figure 1.18 shows the various DSSC architectures using one dimensional TiO₂ as light scattering layer. Reprinted with permission from ref no. 49

1.6 Introduction to Organic Inorganic Hybrid Perovskite semiconductors

Perovskite is a class of crystal structure which possesses same structure as that of calcium titanate (CaTiO₃). This compound was discovered by Russian mineralogist Lev Perovski in 1839.^[50] The perovskite can be broadly classified as zero, two and three dimensional systems.^[51] But the crystal structure with the general formula ABX₃ (3-D perovskites) or A₂BX₄ (2-D perovskites) are actively investigated. In addition there are other crystal structures also present such as A₆BX₅ (1D crystal framework) and A₄BX₆ (0D framework) but such systems are less explored. In all the above mentioned crystal structures, A can be inorganic or organic cation, B is the metal cation and X is an anion either from halogen family or oxygen. The class of inorganic perovskite crystal systems (ABO₃) has shown

successful applications as high $-k$ dielectrics, ferroelectric materials, piezoelectric materials etc.^[52]

Recently Organic inorganic hybrid perovskite are also been explored in the context of optoelectronic applications. They have inorganic halide framework connected through organic molecules. They are of mainly two types: three-dimensional perovskites (3D) and two dimensional layered perovskite (2D)

1.6.1. Three dimensional Perovskite (3D):

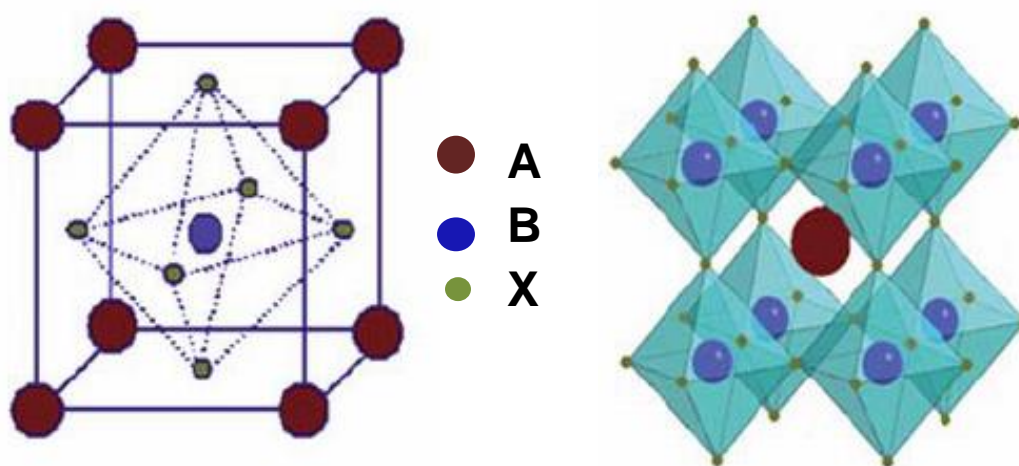


Figure 1.19 shows the unit cell arrangement and extended crystal structure formed by corner shared octahedrons of BX_6 units. Reprinted with permission from ref. no. 53

In case of three dimensional (3-D) perovskites with crystal structures ABX_3 A is organic cation, B is metal ion and X is halogen. The organic cation ‘A’ used is a small monovalent moiety such as Methylammonium ($CH_3NH_3^+$), formamidinium ($HN=CHNH_3^+$) or inorganic cation such as Cs^+ is used in this case.^[54-55] The general crystal structure for 3D perovskite is shown in **figure 1.19**. The perovskite framework consists of BX_6 octahedra with A cations occupying the holes within the structures and counterbalances the charge of BX_3 . This class of perovskites is nowadays referred as ‘perovskites’ by scientific community. In the recent past,

researchers in the optoelectronic domain are actively investigating these perovskites for their fascinating optoelectronic properties.

In the year 2012, use of these materials in the solar cells as an absorber layer suddenly realized the power conversion efficiencies above 10% which is now above 20% (NREL certified) by the end of June 2016.^[56-57] This class of materials has contributed in this sudden rise of efficiencies. These materials are economically cheap and it can be easily processed by low temperature solution processed routes. Later various optoelectronic applications have been explored including solar cells, Light emitting diodes (LEDs), Lasers and water splitting.^[58-61]

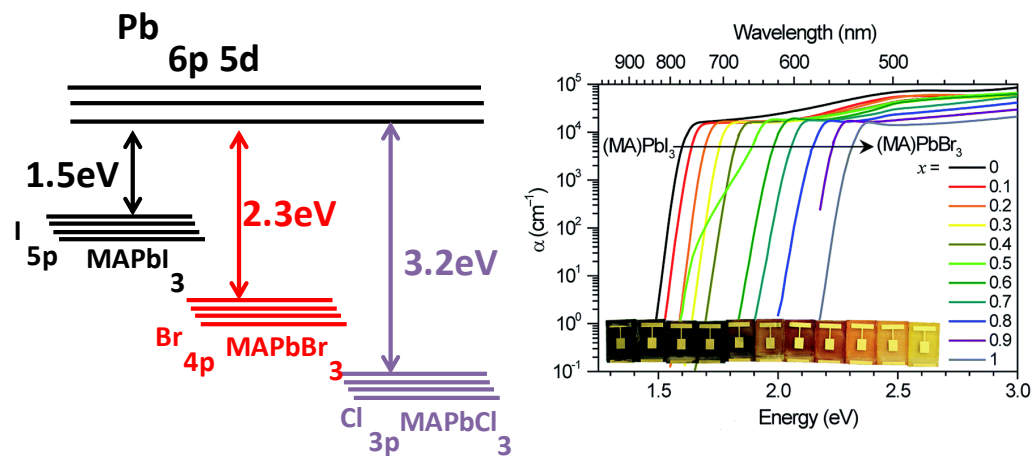


Figure 1.20 (a) shows the band diagram for methylammonium lead halide (MAPbX₃) based perovskite. Figure 1.20 (b) shows the band gap tuning of MAPbI_(3-x)Br_x based mixed halide perovskite. Figure 1.20 (b) is reprinted with the permission from ref. no. 62

In addition to the easy solution processability of these perovskites, they possess excellent optical and electronic properties. In addition, these perovskites have low defect densities and very low non-radiative recombination and high photoluminescence quantum yield. **Figure 1.20 (a)** shows the band gap formation in Methylammonium lead halide based perovskites. The conduction band is mainly contributed by the Pb (6p and 5d) orbitals whereas the halogen atoms

contribute in valance band formation. Hence these hybrid perovskites possess easy band gap tunability. Partial halide ion substitution is a very easy approach for band gap tuning in these perovskites. M.D. McGhee et al has shown band gap tuning in Methylammonium lead iodide and Methylammonium lead bromide based perovskites.^[58] **Figure 1.20 (b)** shows the band gap tuning from 2.3eV to 1.5eV by doping of Br⁻ ion in MAPbI₃ based perovskite.

1.6.2 Two dimensional layered perovskite (2D):

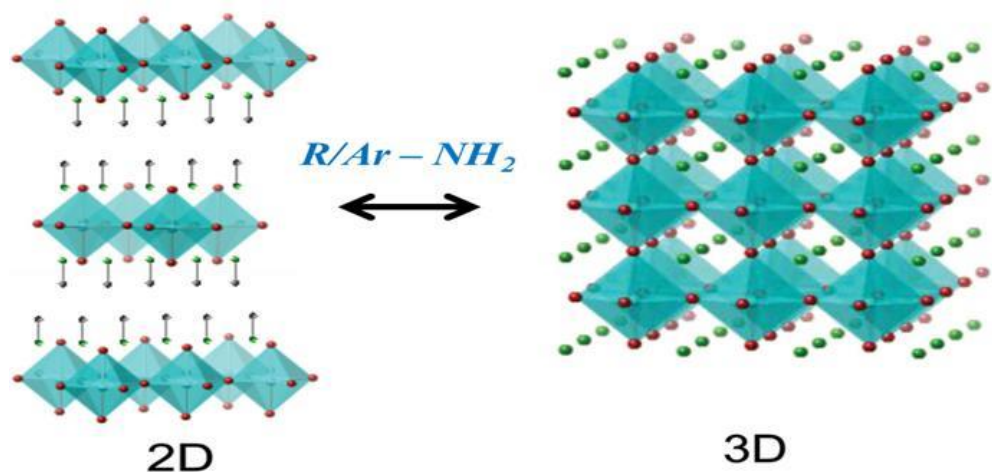


Figure 1.21 shows the interconversion between 2-D layered perovskites and 3-D perovskites. Reprinted with permission from ref no. 65

This class of perovskites is extensively studied by David Mitzi et al mainly in the context of light emitting diodes and field effect transistors.^[63-64] The crystal structure ABX_3 for 3-D perovskites is rigid whereas the lower dimensional perovskites are more flexible and allows easy access to the structural tunability. If the 3-D perovskite crystal structure is cut into the slices and these slices are connected via long alkyl chain amines based ligands as shown in **figure 1.21**, then resulting class of perovskites is called as ‘Two dimensional layered perovskites’ (2-D perovskites)

This class of perovskites has no structural limitations and it allows the use of variety of long chain alkyl amines.

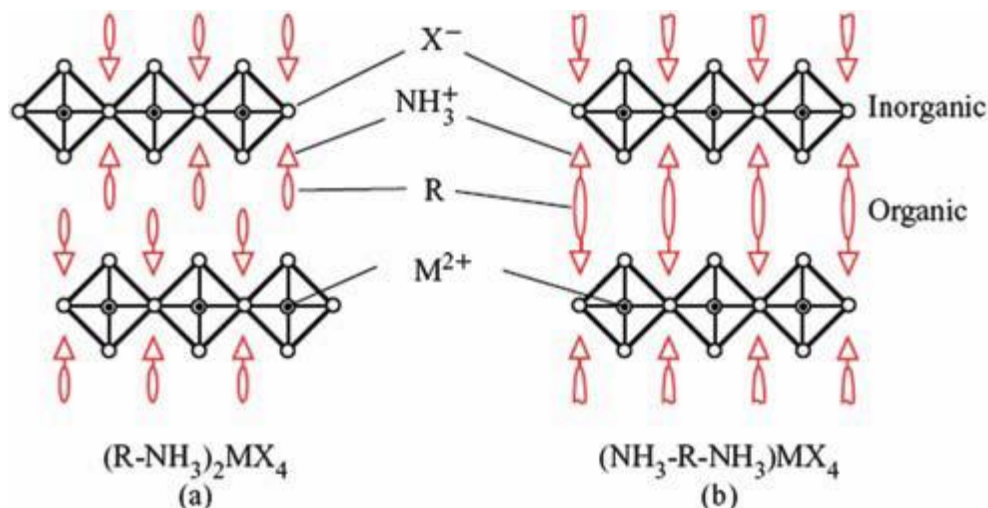


Figure 1.22 shows the layered perovskite structure with mono-amine ($R-NH_3$) and di-amine (NH_3-R-NH_3) as intercalating organic molecules. Reprinted from ref. no. 53

The most common organic cations used for 2-D perovskite are mono- or di-ammonium cations which gives general formulas as $(RNH_3)_2BX_4$ or $(NH_3RNH_3)BX_4$, as shown in **figure 1.22**. The inorganic metal halide semiconductors form a layer which is separated by the large band gap organic molecules as spacer. These 2-D perovskite are naturally self-assembled in layered arrangement where the corner shared BX_6 octahedrons are separated by the intercalating organic molecules. The overall arrangement results in alternate stacking of inorganic layers and organic molecules interaction.

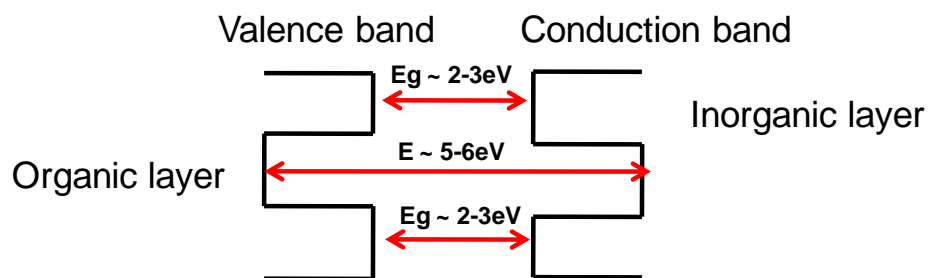


Figure 1.23 shows the quantum well structure formation due to alternate arrangement of inorganic and organic layers in 2-D layered perovskites.

The dielectric mismatch between inorganic material and organic molecules has resulted in the formation of multiple quantum well structures as shown in **figure 1.23**. These types of quantum well structures demonstrate very high room temperature exciton binding energy (300- 400 meV). Such systems show narrow absorption and emission bandwidths. The photoluminescence in such systems is mainly due to exciton formation and recombination.

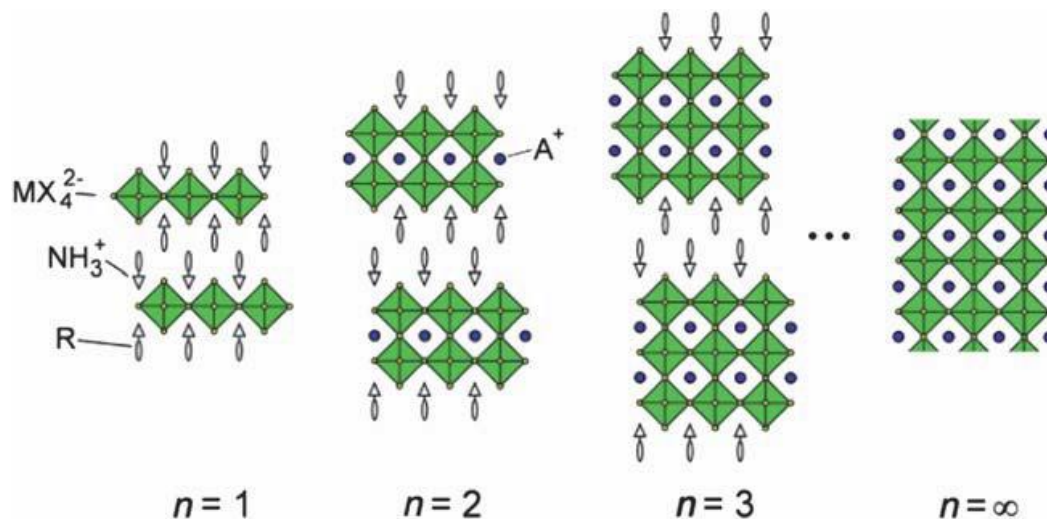


Figure 1.24 shows the schematic presentation of layered perovskites with general formula $A'_2A_{n-1}BnX_{3n+2}$ Reprinted with permission from ref no. 53

Higher order layered perovskites which are combination of 3D and 2D characteristics can also be obtained when mixture of cations is used for intercalation. The general formula can be rewritten as $A'_2A_{n-1}BnX_{3n+2}$ where A' is (CH_3NH_3^+ , Cs^+ or $\text{HN}=\text{CHNH}_3^+$ which is capable of forming 3D perovskite) and A can be long alkyl chain amine (R-NH_2) for intercalation.

These kinds of system provide structural freedom which generates new possibilities to manipulate the photo physical and electronic transport properties beyond conventional 3D perovskite systems.

transport properties. Various solution processible routes and film deposition processes are explored for controlling the morphologies of these semiconductors. This section covers the different optoelectronic applications of hybrid perovskite based materials.

1.7.1 Hybrid Perovskites in Solar cells:

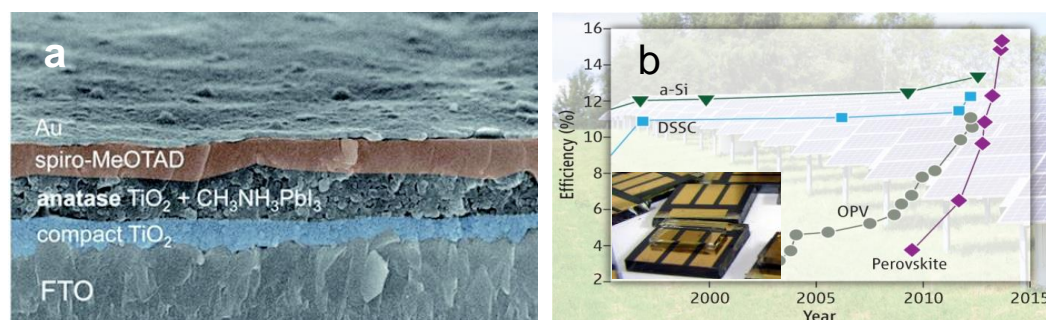


Figure 1.26 (a) shows the FE-SEM cross section image of perovskite thin film solar cell and (b) shows the efficiency progress chart for last 20 years. Reprinted with permission from ref no 68 and 69.

3-D perovskites are most commonly explored class of perovskites for solar cell applications. Methylammonium lead halides (MAPbX₃ where X can be Iodine, bromine and chlorine) are most commonly used materials. The optical band gap of these perovskites is in between 1.5eV to 3eV depending on the halide content. Methylammonium lead iodide (MAPbI₃) with a band gap of 1.5-1.6eV is intensely investigated for solar cell fabrication as it absorbs the entire visible spectrum. **Figure 1.26 (a)** shows the FE-SEM cross section of perovskite solar cell. **Figure 1.26 (b)** shows the efficiency of jump for perovskite solar cells in last 5 years. In 2009, Prof. Miyasaka's group for the first time showed the use of this class of materials as light absorbers in DSSC architecture. In this report, they used 8-12 μ m thick TiO₂ film and perovskite precursor were spin coated. This group has reported 3.8% power conversion efficiency for MAPbI₃ based perovskite solar cells with liquid electrolyte.^[70] Further Prof. N.G.Park and co-workers improved this efficiency via optimization of TiO₂ surface and reported 6.5% efficiency with liquid electrolyte.^[71] Later in 2012, Prof Henry Snaith's group

from Oxford University used solid state hole transporting material spiro-OMeTAD and demonstrated 10% power conversion efficiency. ^[72]

Later upon detail investigation of properties of perovskites it was realized that, the charge extraction rates were significantly faster than conventional dye sensitized based solar cells. Hence later mesoporous Al_2O_3 was used to construct the perovskite based solar cells. Al_2O_3 is insulating in nature. The results based on these solar cells demonstrated that, photocurrent was unaffected while the open-circuit voltage was increased by 200-300 mV. This solar cell showed 10.9% efficiency. ^[73]

Many methodologies were later explored such as, two step deposition ^[74] vacuum assisted thermal evaporation ^[75], Pulse laser deposition ^[76] hot spinning process ^[77] to improve the morphology and coverage of perovskite thin films.

Recent development in the field of perovskite based solar cells has shown the remarkable certified efficiency of 22%

1.7.2 Hybrid Perovskites in Light emitting diode:

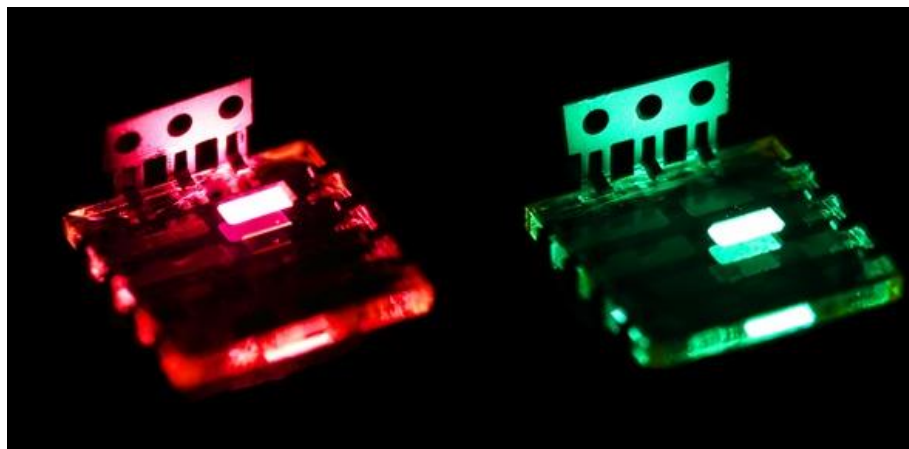


Figure 1.27 shows the Light emitting diodes fabricated using MAPbI_3 (red) and MAPbBr_3 (green) as emissive layer. Reprinted with permission from ref no. 78

Perovskites are also making their definitive progress as promising light emitting diode materials. The ability of easy band gap tunability and the amplified spontaneous emission has helped in demonstration of light emitting diodes in the infra-red region to green wavelength region.^[78] One of the major concept recently emerge goes on to convey the message that, a good solar cell should be a good LED.^[79] Hence hybrid perovskites have transitioned from a good solar cell material to a good light emitter. The intrinsic properties of this semiconductor such as high photoluminescence quantum yield (greater than 70%), high color quality and easy color tunability makes them suitable alternative for the next generation LED applications. In addition, these materials can be easily solution processed which reduces the cost of manufacturing as well. Compared with the existing LED technologies such as Quantum dot based light emitting diodes (QLEDs) or Polymer based light emitting diodes (PLEDs) the perovskite based LEDs are much easier in terms of fabrication of devices. The device fabrication methodologies in this case can be easily transferred on to the large scale applications.

The intrinsic properties of these hybrid perovskites such as high electronic mobilities, high optical absorption and emission, ambipolar charge transport, high photoluminescence quantum yield, low exciton binding energies (In case of 3D perovskites) have made them very suitable for light emitting diode applications.

In this thesis, we have mainly emphasized on modifying the perovskite luminescence ability by using a novel additive mediated solvent recrystallization approach.

1.8 Lead free Perovskites:

Lead (Pb) being a toxic element, uptake of the high performing Pb based optoelectronic devices (solar cells, lasers and LEDs) is difficult. Therefore, looking for Pb free perovskite alternatives is a new challenge for perovskites based optoelectronics community.^[80] Recently, Pb-free alternatives such as use of Tin (Sn), Germanium (Ge), Bismuth (Bi) have been actively investigated^[81-82]

Solar cells based on $\text{CH}_3\text{NH}_3\text{SnI}_3$ perovskite have been shown remarkable performance. The open circuit voltages obtained using these cells are close to their Shockley–Queisser Limits ^[83], Recently, bandgap tunability similar to the Pb based perovskites by variation of the halide and the cation has been demonstrated in Sn based perovskites ^[82]. This opens up new opportunities for research in optoelectronic devices.

1.9 Plan for the thesis:

Photo-voltaic and optoelectronic device based research aimed at making high efficiency low cost solar cells, and highly luminescent light emitting diode (LED) based devices is a rapidly evolving area of research. The rapid growth in device performance is realized through the use of low dimensional nanostructures which possess unique properties and influence the device performance. The present thesis deals with exploration of various solution processible routes for making the nanostructures which are useful in the photo-voltaic and optoelectronic applications.

The **second** chapter presents the methods of synthesis, characterization and device fabrication used in this work, namely electrospinning. Different measurements used to study the structural and optical properties of nanostructures are discussed as well.

The **third** chapter presents the synthesis TiO_2 and gold nanoparticles loaded TiO_2 nanofibers by electrospinning process. Further these nanofibers were used as light harvesting agent in DSSC application. Use of Au- TiO_2 nanofibers demonstrated the overall 25% enhancement in the solar cell efficiency as compared to the control solar cell.

The **fourth** chapter presents the use of modified liquid in liquid electro spray process in conjunction with anti-solvent solvent extraction for the synthesis of low dimensional quantum structures especially 2-D nanosheets of $\text{CH}_3\text{NH}_3\text{PbI}_3$ and $\text{CH}_3\text{NH}_3\text{PbBr}_3$ based layered perovskites. The optical properties of these, as

formed, colloidal nanostructures have shown the band gap tunability over the entire visible range. We have also studied the compositional tailoring by mixing the as formed perovskite precursors before electrospraying. This has shown tunability in luminescence over a broad range of visible spectrum.

The **fifth** chapter presents we present a novel additive mediated recrystallization approach for making highly luminescent perovskite films with less electronic disorder. Quaternary alkyl ammonium halide salt solution was dispensed on to the perovskite films during formation. Our results showed that additive treated films had 250 times higher luminosity as compared to untreated films. The additive treated films show less electronic disorder in terms of Urbach energy which was reduced from 38meV to 18meV. The photoluminescence quantum yield was enhanced from 1% (for untreated film) to 30% (for additive treated). Further we have demonstrated the use of this approach to make light emitting diode (LED) applications.

The **sixth** chapter presents the conclusions of the work presented in this thesis and the future scope for further work.

1.10 References:

- 1) <http://ourfiniteworld.com>
- 2) Energy Information Administrator, Report on 'World Consumption of Primary Energy by Energy Type and Selected Country', 2006.
http://www.iea.org/publications/freepublications/publication/key_world_energy_stats-1.pdf
- 3) Renewable energy, Environmental centre, University of Colorado,
<http://www.colorado.edu/center/energy-us/renewable-energy>
- 4) <https://www.nrdc.org>

5) European Commission, The Energy Challenge of the 21st Century: The role of Nuclear

Energy, http://europa.eu.int/comm/research/rtdinfo_en.html

6) <https://www.edfenergy.com/energyfuture/generation-wind>

7) http://en.wikipedia.org/wiki/Wind_power

8) <http://www.edfenergy.com/energyfuture/generation-hydro>

9) <http://en.wikipedia.org/wiki/Hydroelectricity#Advantages>

10) http://en.wikipedia.org/wiki/Geothermal_energy#Economics

11) Union of Concern scientist, Science for healthy planet and safer world, <http://www.ucsusa.org/>

12) A.E. Becquerel, C. R. Acad. Sci. 1839, 9, 561- 567.

13) a) A. Goetzberger, J. Luther, G. Willeke, Solar Energy Materials and Solar Cells 2002, 74, 1-11; b) Y. J. Lee, B. S. Kim, S. M. Ifitiquar, C. Park, J. Yi, Journal of the Korean Physical Society 2014, 65, 355-361.

14) Heliatek, Development history of photovoltaics,

<http://www.heliatek.com/technologie/organische-photovoltaik/?lang=en>.

15) M. A. Green, K. Emery, Y. Hishikawa, W. Warta, E. D. Dunlop, Prog. Photovolt: Res. Appl. 2011, 19, 565-572.

16) M. Gloeckler, I. Sankin, Z. Zhao, IEEE Journal of Photovoltaics, 2013, 3, 1389–1393.

17) A. D. Compaan, Solar Energy Materials & Solar Cells, 2006, 90, 2170–2180.

18) Kaduwal, Deepak, Birger Zimmermann, and Uli Würfel. Solar Energy Materials and Solar Cells 120 (2014): 449-453.

- 19) S. Karg, W. Riess, V. Dyakonov, M. Schwoerer, *Synthetic Metals*, 1993, 54, 427-433.
- 20) J. J. M. Halls, K. Pichler, R. H. Friend, S. C. Moratti, A. B. Holmes, *Appl. Phys. Lett.*, 1996, 68, 3120-3122.
- 21) J. J.M. Halls, R.H. Friend, M. D. Archer, R. D. Hill, *Clean electricity from photovoltaics*. London: Imperial College Press. pp. 377–445. ISBN 1860941613.
- 22) B. Reeja-Jayan and A. Manthiram, *RSC Adv.*, 2013, 3, 5412-5421.
- 23) B. Oregan, M. Gratzel, *Nature* 1991, 353, 737.
- 24) S. Mathew, A. Yella, P. Gao, R. Humphry-Baker, B. F. E. Curchod, N. Ashari-Astani, I. Tavernelli, U. Rothlisberger, M. K. Nazeeruddin, M. Gratzel, *Nature Chemistry* 2014, 6, 242.
- 25) Woronowicz, Kamil, Saquib Ahmed, Archana A. Biradar, Ankush V. Biradar, Dunbar P. Birnie, Tewodros Asefa, and Robert A. Niederman. *Photochemistry and photobiology* 88, no. 6 (2012): 1467-1472.
- 26) Deepak, T. G., Anjusree, G. S., Thomas, S., Arun, T. A., Nair, S. V., & Nair, A. S. (2014). 4(34), 17615-17638.
- 27) K. Keis, E. Magnusson, H. Lindstrom, S.E. Lindquist, A. Hagfeldt, *Solar Energy Materials and Solar Cells*, 2002, 73, 51–8.
- 28) E. Ramasamy, J. Lee, *J. Phys Chem. C*, 2010, 114, 22032–7.
- 29) M. Gratzel, *Inorg. Chem.* 2005, 44, 6841-6851.
- 30) J. D. R.-Mayhew, D. J. Bozym, C. Punckt, and I.A. Aksay, *ACS Nano*, 2010,4, 6203-6211.

- 31) Sebastián, D., Baglio, V., Girolamo, M., Moliner, R., Lázaro, M. J., & Aricò, A. S. (2014). *Journal of Power Sources*, 250, 242-249.
- 32) H.K. Mulmudi, S. K. Batabyal, M. Rao, R. R. Prabhakar, N. Mathews, Y- M Lam and S. G. Mhaisalkar, *Phys. Chem. Chem. Phys.*, 2011, 13, 19307–19309.
- 33) Tathavadekar, M., Biswal, M., Agarkar, S., Giribabu, L., & Ogale, S. (2014). *Electrochimica Acta*, 123, 248-253.
- 34) S. Y. Huang, G. Schlichthorl, A. J. Nozik, M. Gratzel, A.J. Frank *Journal of Physical Chemistry B*, 1997, 101, 2576–82.
- 35) T. Daeneke, Y. Uemura, N.W. Duffy, A.J. Mozer, N. Koumura, U. Bach, L. Spiccia, *Advanced Materials*, 2012, 24, 1222-1225.
- 36) Wenger, Sophie. "Strategies to Optimizing Dye-Sensitized Solar Cells." (2010).
- 37) J. Bisquert and V. S. Vikhrenko, *J. Phys. Chem. B*, 2004, 108, 2313– 2322.
- 38) A. C. Fisher, L. M. Peter, E. A. Ponomarev, A. B. Walker and K. G. U. Wijayantha, *J. Phys. Chem. B*, 2000, 104, 949–958.
- 39) H. Y. Chen, D.B. Kuang and C.-Y. Su, *J. Mater. Chem.*, 2012, 22, 15475–15489.
- 40) Deepak, T. G., Anjusree, G. S., Thomas, S., Arun, T. A., Nair, S. V., & Nair, A. S. (2014). *RSC Advances*, 4(34), 17615-17638.
- 41) A. Usami, *Chem. Phys. Lett.*, 1997, 277, 105.
- 42) S. Hore, P. Nitz, C. Vetter, C. Prah, M. Niggemann and R. Kernab, *Chem. Commun.*, 2005, 2011-2013
- 43) Y. Sanehira and S. Uchida, *Kagaku Kogyo*, 2004, 55, 796.
- 44) Y. Dzenis, *Science*, 2004, 304, 1917.

- 45) P. Joshi, L. Zhang, D. Davoux, Z. Zhu, D. Galipeau, H. Fong and Q. Qiao, *Energy Environ. Sci.*, 2010, 3, 1507.
- 46) K. Nakayama, T. Kubo and Y. Nishikitani, *Jpn. J. Appl. Phys.*, 2008, 47, 6610.
- 47) A. M. Bakhshayesha, M. R. Mohammadia, H. Dadara and D. J. Fray, *Electrochim. Acta*, 2013, 90, 302.
- 48) S. Chuangchote, T. Sagawa and S. Yoshikawa, *Appl. Phys. Lett.*, 2008, 93, 033310-033313.
- 49) Deepak, T. G., G. S. Anjusree, Sara Thomas, T. A. Arun, Shantikumar V. Nair, and A. Sreekumaran Nair. *RSC Advances* 4, no. 34 (2014): 17615-17638.
- 50) H.-R. Wenk and A. Bulakh, Cambridge University Press, 2004.
- 51) Mitzi, D. B. (2007). *Progress in Inorganic Chemistry*, Volume 48, 1-121.
- 52) López-Juárez, Rigoberto, Federico González, and María-Elena Villa. INTECH Open Access Publisher, 2011.
- 53) Cheng, Ziyong, and Jun Lin. *CrystEngComm* 12, no. 10 (2010): 2646-2662.
- 54) Weber, D. Z. *Naturforsch., B: J. Chem. Sci.* 1978, B33, 1443–1445.
- 55) Mitzi, D. B.; Liang, K. J. *Solid State Chem.* 1997, 134, 376–381.
- 56) Lee, M. M., Teuscher, J., Miyasaka, T., Murakami, T. N., and Snaith, H. J. (2012) *Science*, 338(6107), 643-647.
- 57) Zhou, H., Chen, Q., Li, G., Luo, S., Song, T. B., Duan, H. S., ... & Yang, Y. (2014). *Science*, 345(6196), 542-546.
- 58) Deschler, F., Price, M., Pathak, S., Klintberg, L. E., Jarausch, D. D., Higler, R., S. Hüttner, T. Leijtens, S.D. Stranks. H.J. Snaith, Atatüre, M. R.H.Friend (2014). *The journal of physical chemistry letters*, 5(8), 1421-1426.

- 59) J. Burschka, N. Pellet, S.-J. Moon, R. Humphry-Baker, P. Gao, M. K. Nazeeruddin, and M. Grätzel, *Nature*, vol. 499, no. 7458, pp. 316–319, 2013.
- 60) G. Xing, N. Mathews, S. S. Lim, N. Yantara, X. Liu, D. Sabba, M. Grätzel, S. Mhaisalkar, and T. C. Sum, *Nat. Mater.* 2014, vol. 13, no. 5, pp. 476–80.
- 61) J. Luo, J.-H. Im, M. T. Mayer, M. Schreier, M. K. Nazeeruddin, N.-G. Park, S. D. Tilley, H. J. Fan, and M. Grätzel, *Science*, 2014, 345,(6204) 1593–1596.
- 62) Hoke, E. T., Slotcavage, D. J., Dohner, E. R., Bowring, A. R., Karunadasa, H. I., & McGehee, M. D. (2015). *Chemical Science*, 6(1), 613-617.
- 63) Mitzi, D. B. (2004). *Journal of Materials Chemistry*, 14(15), 2355-2365.
- 64) Mitzi, David B., C. A. Feild, W. T. A. Harrison, and A. M. Guloy. *Nature*,(1994): 467-469.
- 65) González-Carrero, S., Galian, R. E., & Pérez-Prieto, J. (2015). *Particle & Particle Systems Characterization*, 32(7), 709-720.
- 66) Y. Takeoka, K. Asai, M. Rikukawa, K. Sanui, *Chem. Lett.* 2005, 34, 602.
- 67) Papagiannouli, I., Maratou, E., Koutselas, I., & Couris, S. (2014). *The Journal of Physical Chemistry C*, 118(5), 2766-2775.
- 68) Lee, Jin-Wook, Taek-Yong Lee, Pil J. Yoo, Michael Grätzel, Subodh Mhaisalkar, and Nam-Gyu Park. *Journal of Materials Chemistry A* 2, no. 24 (2014): 9251-9259.
- 69) Hodes, Gary. *Science* 342, no. 6156 (2013): 317-318.
- 70) Kojima, Akihiro, Kenjiro Teshima, Yasuo Shirai, and Tsutomu Miyasaka. *Journal of the American Chemical Society* 131, no. 17 (2009) 6050-6051.
- 71) Im, Jeong-Hyeok, Chang-Ryul Lee, Jin-Wook Lee, Sang-Won Park, and Nam-Gyu Park. *Nanoscale* 3, no. 10 (2011) 4088-4093.

- 72) Lee, Michael M., Joël Teuscher, Tsutomu Miyasaka, Takuro N. Murakami, and Henry J. Snaith. *Science* 338, no. 6107 (2012): 643-647.
- 73) Snaith, Henry J. *Advanced Functional Materials* 20, no. 1 (2010): 13-19.
- 74) Burschka, Julian, Norman Pellet, Soo-Jin Moon, Robin Humphry-Baker, Peng Gao, Mohammad K. Nazeeruddin, and Michael Grätzel. *Nature* 499, no. 7458 (2013): 316-319.
- 75) Liu, Mingzhen, Michael B. Johnston, and Henry J. Snaith. *Nature* 501, no. 7467 (2013): 395-398.
- 76) Bansode, Umesh, Rounak Naphade, Onkar Game, Shruti Agarkar, and Satishchandra Ogale. *The Journal of Physical Chemistry C* 119, no. 17 (2015): 9177-9185.
- 77) Nie, Wanyi, Hsinhan Tsai, Reza Asadpour, Jean-Christophe Blancon, Amanda J. Neukirch, Gautam Gupta, Jared J. Crochet et al. *Science* 347, no. 6221 (2015): 522-525.
- 78) Tan, Zhi-Kuang, Reza Saberi Moghaddam, May Ling Lai, Pablo Docampo, Ruben Higler, Felix Deschler, Michael Price et al. *Nature nanotechnology* 9, no. 9 (2014): 687-692.
- 79) O. D. Miller, E. Yablonovitch, and S. R. Kurtz, "IEEE J. Photovoltaics, vol. 2, no. 3, pp. 303–311, Jul. 2012.
- 80) M. A. Green, A. Ho-Baillie, and H. J. Snaith, *Nat. Photonics*, vol. 8, no. 7, pp. 506–514, Jun. 2014.
- 81) C. C. Stoumpos, C. D. Malliakas, and M. G. Kanatzidis, *Inorg. Chem.*, vol. 52, no. 15, pp. 9019–38, Aug. 2013.
- 82) F. Hao, C. C. Stoumpos, D. H. Cao, R. P. H. Chang, and M. G. Kanatzidis, *Nat. Photonics*, vol. 8, no. 6, pp. 489–494, May 2014.

- 83) N. K. Noel, S. D. Stranks, A. Abate, C. Wehrenfennig, S. Guarnera, A. Haghighirad, A. Sadhanala, G. E. Eperon, S. K. Pathak, M. B. Johnston, Annamaria Petrosino, L. Herz, and H. Snaith *Energy Environ. Sci.*, vol. 7, no. 9, pp. 3061–3068, Aug. 2014.

Chapter 2

Experimental Methods, Characterization Techniques and Device Fabrication

This chapter covers the synthesis techniques, characterization tools, device fabrication and device testing protocols used in this thesis. The process of electrospinning for making nanofibers and later colloidal systems is discussed at length. The modification of electrospinning process used in this thesis is discussed in later part. Characterization techniques used for elucidation of the structure, composition and optical properties of materials are covered in details. The Dye sensitized solar cell (DSSC) and Perovskite based light emitting diode (LED) fabrication protocol is given towards the end of this chapter.

Introduction: Researchers are deeply interested in studying the structural and optical characteristics of materials in order to apply it further for related applications. To know these properties, various spectroscopy techniques have been explored which can derive the structure and other interesting information from the product. Also, the characterization of a material is very essential to determine its quality and composition. This chapter gives a description of the various experimental techniques used in carrying out the different experiments reported in this thesis.

Section I

2.1 The Electrospinning Technique

One dimensional nanostructures possess very own advantages such as, high aspect ratio, unidirectional electronic transport and continuous channels. The synthesis of one dimensional nanostructure can be easily achieved by various chemical synthesis routes such as hydrothermal synthesis, vapor phase growth, self-assembly approach, and electrospinning. Electrospinning is very versatile and popular technique for making one dimensional nanostructures at research lab scale as well as at industrial scale. In this section we have discussed the brief history, working principle, different categories of electrospinning and the applications in various fields.

2.2: Electrospinning

Since the last decade electrospinning has emerged out as technologically viable manufacturing process. Using this method we can produce continuous one dimensional nanofibers (NFs). Research community as well as industries in various sectors such as tissue engineering, energy storage, photovoltaic, flexible electronics, and membrane science are using this versatile process^[1] Nanofibers ranging from few nanometers upto several microns can be produced using this technique. This method is also applicable for natural as well as synthetic polymers and its composite with ceramic nanofibers.

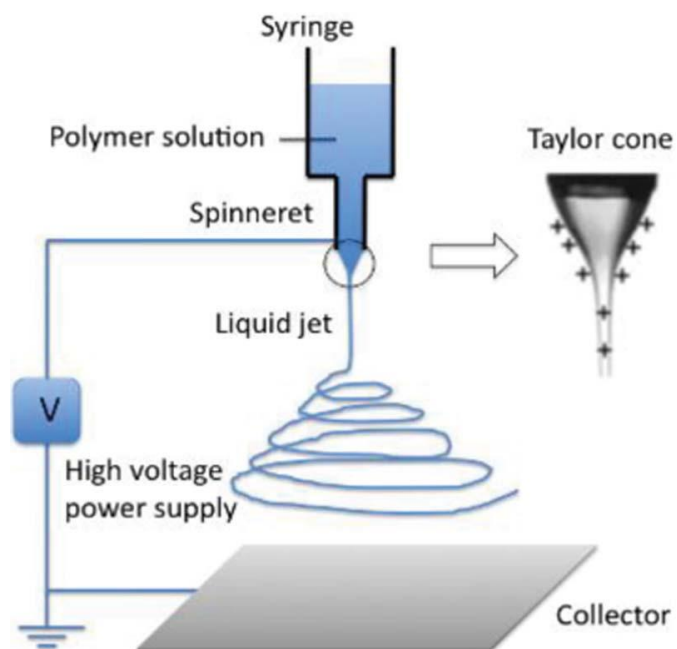


Figure 2.1: Electrospinning set up. Reprinted with permission from reference No 28.

Further this process has shown promising applications for making isolated single nanofiber as well as aligned mesh of nanofibers.. The **figure 2.1** shows the nanofibers formation process. The dimensions of these nanofibers are even orders of magnitude less than human hairs. Such nanofibers possess very surface area to volume ratio making them suitable for range of applications.



Figure: 2.2 The electrospinning jet and NF formed on collector^[2] Reproduced by the permission from ref no. 2

2.2.1 History of Electrospinning

The weaving process or the spinning tools are known since many centuries. Especially in India, the mechanical spinning tool was used to make fabrics.^[3] In literature reports suggest that, electrospinning is established since 1745, at that time it was known as electrostatic spinning.^[4] Later around 1902, scientist J.F. Cooley and W.J. Morton, patented this process of electrospinning.^[5,6] In 1934, Anton Formhals developed this process towards its commercialization.^[7,8] The first commercialized application of this technique was in the filtration membrane domain.^[9] Later many contributions explored this technique for variety of applications. Numerous patents and research publications were reported in the following years which reflect the versatility of this technique in research domains.

2.2.2 Electrospinning process & working mechanism

The electrospinning set up usually consists of,

- a. High voltage DC power source
- b. Syringe pump
- c. Syringe with needle. The positive terminal is connected to syringe tip.
- d. Collector which is grounded.

The current electrospinning set ups are either horizontal or vertical in arrangements. The diameter of nanofibers is mainly dependent on the needle diameter as it decides the volume of fluid droplet. The applied voltage lies in the range of 10-50kV. The distance between needle tip and collector can be adjusted as per the requirement. In the presence of applied electric field the polymer fluid droplet gets stretched and it results in nanofibers.. The concentration of polymer solution can be adjusted based on the molecular weight of polymer. Polymer solution is loaded in the syringe which is further fixed in the syringe pump.. When the polymer droplet experiences the electric field, the drop gets stretched up and results in cone formation. This cone is called as ‘Taylor cone’. In presence of high electric field the droplet stretching and jet formation results in nanofibers of polymers which gets deposited on to the collector. During the stretching process due to sudden elongation of polymer droplet the quick evaporation of solvent takes place. As synthesized nanofibers through this process are mainly randomly oriented and in the form of self-supporting mat.

2.2.3 Aligned Nanofibers

During electrospinning due to Taylor cone formation randomly oriented fiber mats are deposited. Alignment of nanofibers in certain direction has always been a challenge for researchers. Towards this, rotating cylindrical collectors in the form of drums, circular disks have been explored. The first use of rotating collector was demonstrated by Boland et al.^[10] In coming years many different possibilities were explored for fiber alignment. An interesting approach of using electrodes with a small gap was demonstrated by Li *et al* to align the fibers in between the

gap. ^[11] Using this way single fiber based nanodevices can be made. Later various advantages such as ‘near field electrospinning’, ‘core-shell nanofibers’ using co-axial syringe is also been investigated.

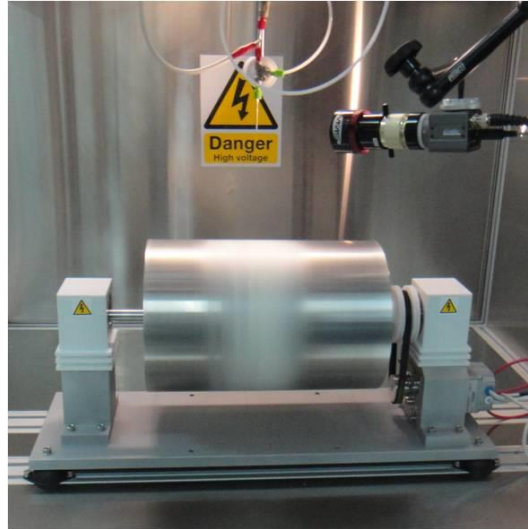


Figure: 2.3 show the formation of aligned nanofibers using rotating drum collector.

<http://www.yflow.com/electrospinning-equipment/professional-electrospinning-equipment-packs/>

2.2.4 Core shell Electrospinning

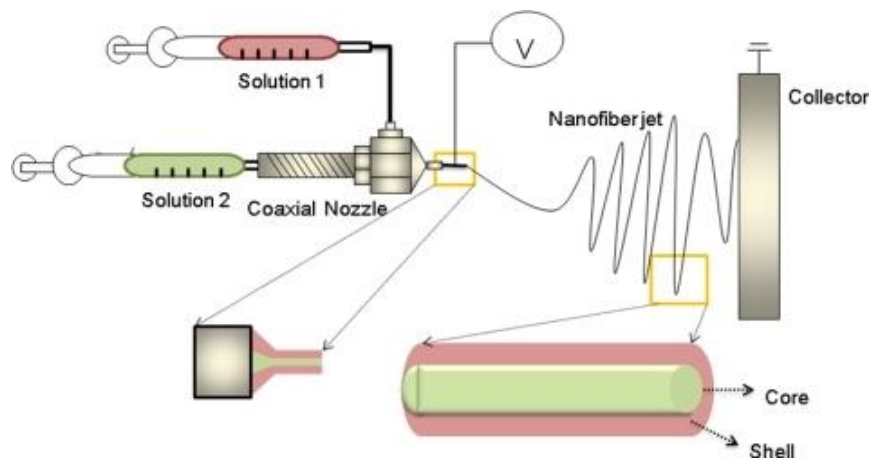


Figure 2.4 shows the schematic of core shell electrospinning process. Reprinted with permission from ref no. 14

It consists of two independent syringes filled with different polymer solutions. Use of concentric nozzle connects the two syringes and the polymer droplets as core shell comes in the applied electric field. In applied electric field, the individual polymer jet forms core and sheath to produce core-shell nanofibers. This process is very effective in terms of applications for e.g. insertion of bioactive drugs inside the core materials can be helpful for wound healing applications.^[12-13]

2.2.5 Factors affecting electrospinning

Two prime parameters decide the formation of smooth nanofiber namely intrinsic and extrinsic parameters. Intrinsic parameters include the polymer solution properties such as polymer concentration conductivity, viscosity, In addition to this, surface tension, molecular weight of polymer and solvent boiling point are also important factors. By considering the above parameters the basic criteria include the choice of appropriate solvent for the polymer dissolution. The complete polymer chain entanglement has to take place in order to form homogenous and uniform solution. The solvent should preferably possess lesser boiling point, for the quick solvent evaporation during electrospinning. The polymer molecular weight also plays an important role, as high molecular weight polymer structures entangle due to their long chain structures. The chain entanglement is a critical parameter for stabilizing the jet during bending and stretching of polymer liquid drop in electric field. Thus, the molecular weight should be optimum in order to control the flow of the polymer solution. The viscosity and polymer concentration also affects the fiber formation in the similar manner. The conductivity of the solution is also important parameter which critically decides the fiber formation process. Under the applied electric field, the solution with higher conductivity experiences more elongation; this reduces the fiber diameter as well as bead formation, if any. The surface tension also controls the fiber formation, by eliminating the beads in the fibers.

The external parameters also have impact on the electrospinning process. These include the volumetric feed/flow rate, needle tip-to collector distance, electric

field and the needle diameter. The applied electric voltage is one of the crucial factors in the formation of Taylor cone. The applied voltage mainly affects the fiber diameter or sometimes it may lead to bead formation also. ^[15] The applied voltage mainly affects the elongation/stretching of the drop. ^[16] The feed rate of the polymer solution is another important parameter; this affects the solidification process of the nanofiber. The slower feed rate is always preferred as it allows the sufficient time for solvent evaporation and stretching of the liquid drop for formation of bead free nanofiber. ^[17] The distance between the needle and collector also affects the fiber formation process during electrospinning. If this distance is short, the nanofiber does not have enough time for solidification whereas if the distance is too long, the bead formation possibility increases.

2.2.6 Electrospaying process

In this process instead of polymer solution any liquid solution is used. In polymer solutions polymer chains forms entangled network which leads to stretching in presence of applied electric field and generates polymer nanofibers. But in other solutions of inorganic salts or small organic molecules such entangled networks are absent. When such solutions are subjected to very high electric field, the liquid droplets breaks and it forms a fine aerosol. The liquid jet also forms Taylor cone in this case. This process is very useful in many technological applications. It is mainly used as ion source for mass spectrometry. Similarly liquid metal ion sources are used in ion implantation and focused ion beam (FIB) instruments. This technique is widely used in nanotechnology to deposit the monolayer of particles on the nanostructured surfaces. Drug nanoparticles are prepared using this method. Similarly in some air purifiers this technique is used.



Figure 2.5 shows the formation of aerosol under application of electric field.

<http://www.bioinicia.com/technology-2/>

2.2.7 Applications of electrospinning technology

Since the discovery, various groups have contributed towards the rapid development in the field of electrospinning technology. The current progress is chiefly towards the applications of the NF in various areas as can be seen from the **figure 2.6**. The electrospun NFs are found to be useful mainly in the nanotechnology areas such as, heterogeneous catalysis, biomedical applications such as drug delivery, tissue engineering, water purification membranes. Using this method variety of metal oxides and metal Chalcogenide families have also been explored. This technique in recent years has also shown its suitability in charge storage, optoelectronic applications, water splitting, etc.^[18] In addition to this, the polymer NFs gives high mechanical strength and flexibility which are useful for currently growing flexible electronic devices based research as well.

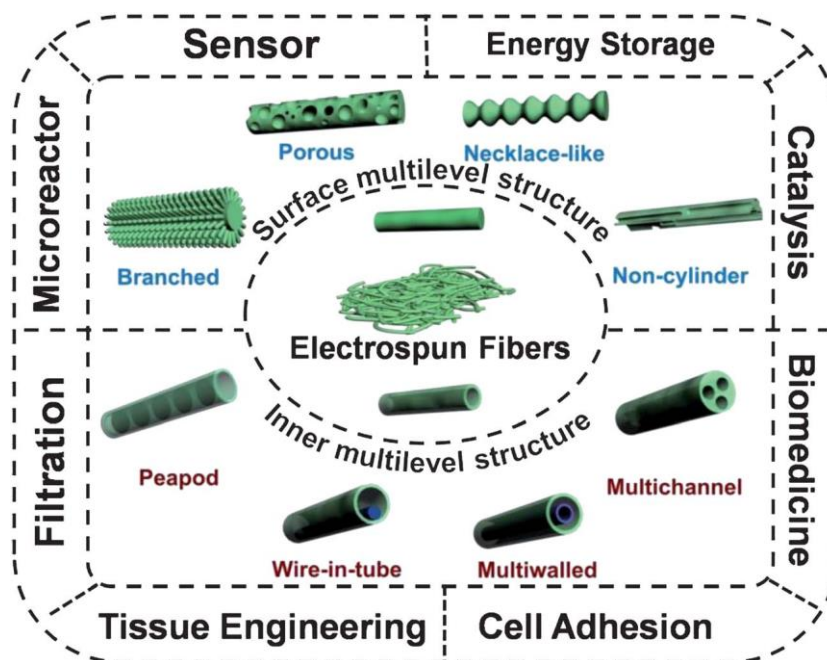


Figure: 2.6 Applications of electrospun nanofibers in various fields. Reprinted with permission from ref no. 18

2.3 Spin Coating

Spin coating is used to deposit thin films of various materials such as polymers, metal oxide suspensions, proteins etc. on to the smooth and flat surface.^[19]

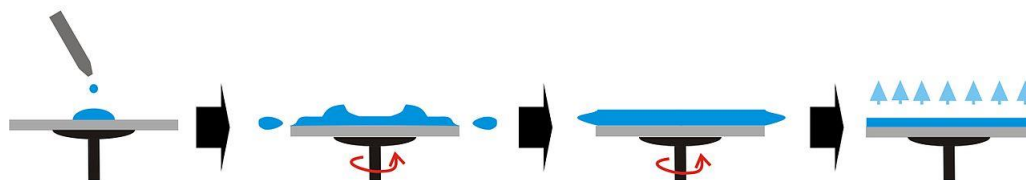


Figure: 2.7 The process of spin coating

<http://www.spincoater.com/what-is-spin-coating.php>

A viscous solution is drop-casted onto the clean substrate and then the substrate is rotated at fixed rotations for given time. Number of rotations in one minute is

abbreviated as 'RPM'. Depending on the desired thickness of the film RPM can be adjusted.. During spin coating, solution is spread in the outward direction, due to centrifugal force. Excess amount of solution spills out and solvent evaporation takes place simultaneously. As the solvent evaporates the viscosity of desired material increases on the substrate. Hence the adhesion to the substrate is improved and film is formed. This process also provides an advantage of making multilayered structures. The film thickness and the uniform coverage of film are mainly dependent on the solution properties such as viscosity, surface tension, solvent evaporation rate etc.

Section II: Characterization Techniques

Introduction:

For optoelectronic applications the nanomaterials should be initially characterized for its structural optical and electrical properties. This information is crucial to use them in devices. In this section we discuss various characterization techniques used for the research work.

2.4 X-ray Diffraction (XRD)

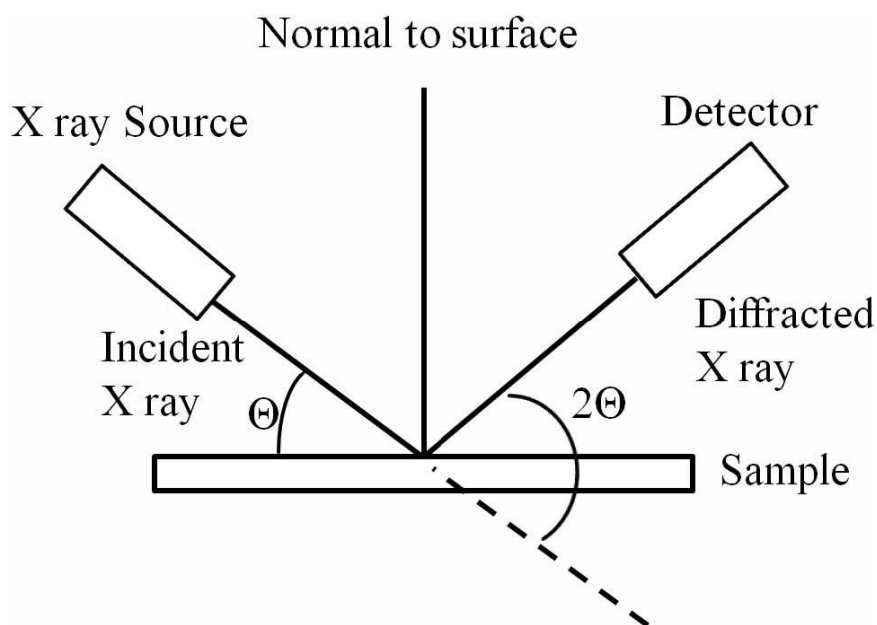


Figure: 2.8 The working principle of XRD

X-ray diffraction (XRD) is a technique used to study the crystal structure and phase analysis of materials. This technique is also helpful in analyzing very basic important properties of materials such as, crystallite size, lattice parameters, preferred orientation of polycrystalline materials, orientation of single crystals, defects in the systems; strain etc.^[20] This technique is suitable for materials bulk phase materials, thin films of materials as well for powdered samples. In case of nanomaterials, the changes in XRD pattern as compared to their bulk counterparts gives us valuable information about nature of strain present in the material.

In XRD, a collimated monochromatic beam of X-rays is incident on the sample. In this case, the constructive interference of x-rays is observed only at certain angle θ which are closely related to the (hkl) planes, where the path difference is an integral multiple (n) of wavelength (λ). Based on this, Bragg's equation is given by,

$$n\lambda = 2d\sin\theta$$

Where ' λ ' is the wavelength of incident X-radiation, 'd' is interplanar spacing between crystal planes, ' θ ' is the scattering angle and 'n' is called as order of diffraction.

In nanostructured materials, X-rays are diffracted by oriented crystallites to satisfy Bragg's law. One can calculate the inter-planar distance if the values of θ and λ are already known. This XRD can be operated in various modes such as θ -2 θ scan mode, θ -2 θ rocking curve, and Φ scan. In θ -2 θ scan mode, the X-rays falls on to the sample surface making an angle of θ while the detector motion is coupled in such a way that it always makes an angle of 2 θ with incident X-rays. The Schematic view of X-ray diffraction is shown in **Figure 2.8**

The incident X-rays may reflect in many directions but only be measured which share a common normal to give constructive interference, so we will require,

$$\text{Angle of incidence } (\theta_1) = \text{angle of Reflectance } (\theta_2)$$

This condition can be achieved by moving the detector twice as fast as the source.

In nanostructured materials, the smaller grain size generated the significant strain on the surface and hence the peak broadening or peak position shift is observed as compared to their bulk counterparts. From XRD data of nanomaterials, one can calculate the change in interplanar spacing (d) and the crystallite size. The crystallite size is usually calculated using Scherrer's formula given as

$$D = k\lambda/\beta\cos\theta$$

Where 'k' is Scherrer's constant ~ 0.9 'β' is full width half maximum (FWHM).

XRD technique is very less sensitive towards low 'z' elements. It is therefore mostly used for high 'z' materials. For low 'z' materials neutron or electron diffraction is commonly used.

In the present work the XRD patterns are recorded on to the PAN-analytical Philips X'Pert PRO powder diffractometer at National chemical Laboratory, Pune. For all the cases, we have used Cu K α X-ray source of wavelength = 1.542 \AA .

2.5 UV-Visible absorption spectroscopy

UV-Vis spectroscopy records the transmitted or reflected light from the sample and presents information about the absorption signals due to electronic transitions.

The spectroscopy is also called as electronic spectroscopy. The electronic spectra of molecules are quite complex and are observed due to absorption of UV and visible regions of electromagnetic spectrum. In semiconductors, when the incident photon energy exceeds the band gap energy of the material, absorption occurs and signal is recorded by the spectrometer whereas in metals when the surface free electrons vibrate coherently with the incident frequency then resonant absorption takes place. This spectrometer can operate in two modes (i) transmission and (ii) reflection mode. In transmission mode usually thin films and colloidal NPs, well-dispersed in solvent are used. While in reflectance mode, opaque thin films and NPs which are not dispersible in solvents is analyzed.

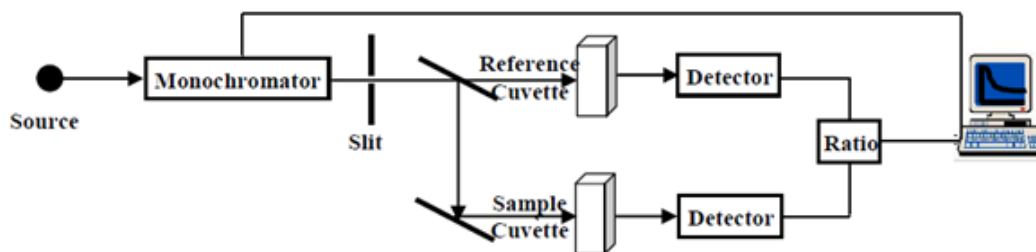


Figure 2.9 Representation of UV-Visible spectrophotometer in transmission mode.

In UV-Visible absorption spectroscopy, light from a suitable source is transmitted through a monochromator to yield light of desired energy. The emerging light is then passed through the sample under study and finally to a detector (**Figure 2.9**). Typically, the light from the source is split into two beams by a chopper; one beam passes through the sample, whereas the other through the reference. The detector, which is often a photodiode, alternates between measuring the sample beam and the reference beam. Most of the double beam instrument has two detectors, where the sample and reference beams are recorded at the same time. The two beams are recombined in a single optical path via the use chopper which blocks one beam at a time.

2.6 Photoluminescence (PL) Spectroscopy

Photoluminescence (PL) is the spontaneous emission of photons after the absorption light by the material. Photoluminescence is a very important tool to characterize the optoelectronic properties of semiconductors as PL spectroscopy can access certain energy level which otherwise cannot be detected using UV-Vis absorbance spectroscopy. In order to observe luminescence in solid sample the material should possess certain band gap so that the transition from excited state to lower state can lead to luminescence. Typically in semiconductor samples the electron-hole pairs are created upon illumination with electromagnetic radiations with energy greater than the band gap of semiconductor. Depending on the lifetime of excited states the electrons recombine with holes which lead to emission of photons. The emitted photons may or may not have energy equal to

the band gap of semiconductor depending on absence or presence of non-radiative recombination. Therefore the analysis of intensity of PL spectrum as a function of wavelength can lead to important information about the energy levels and defect levels in the sample. PL can be classified as fluorescence or phosphorescence based on the lifetime of electronic states participating in the radiative emissions from the sample. In fluorescence the sample emits light of longer wavelength than the wavelength of absorbed light with typical luminescence lifetime range between 10^{-8} - 10^{-5} seconds. However in case of phosphorescence the luminescence lifetime can range from milliseconds to hours. The PL spectrum of a semiconducting sample is analyzed on basis of peak positions in PL and their intensities. The intensity of a peak in photoluminescence spectrum can depend on the intensity of the excitation radiation and also on the rate of radiative and non-radiative decays.



Figure 2.10 shows possible luminescence pathways in semiconductor

Different pathways in which the radiative decay can take place in a semiconducting sample are shown in **Figure 2.10**. The presences of defect states in particular affect the wavelength of emitted photons in luminescence.

2.7 Microscopy Techniques

2.7.1. Transmission Electron Microscopy (TEM)

Transmission electron microscope (TEM) allows examination of materials from micron scale down to atomic resolution.¹⁰ In a TEM, under ultra-high vacuum conditions electrons are released from an electron gun by thermionic or field emission method and go through the microscope column by means of accelerating voltage between 200 and 300 kV. Later electrons are aimed to a double/triple

electromagnetic lens system to illuminate the nanometer thin specimen. Electrons are scattered as they pass the sample, due to electrostatic potentials of its atoms. Result of incoherent electron scattering as well as (coherent) electron diffraction (ED) produces image contrast. It is also possible to study crystal structure by electron diffraction study. The schematic of TEM is shown in **Figure 2.11**

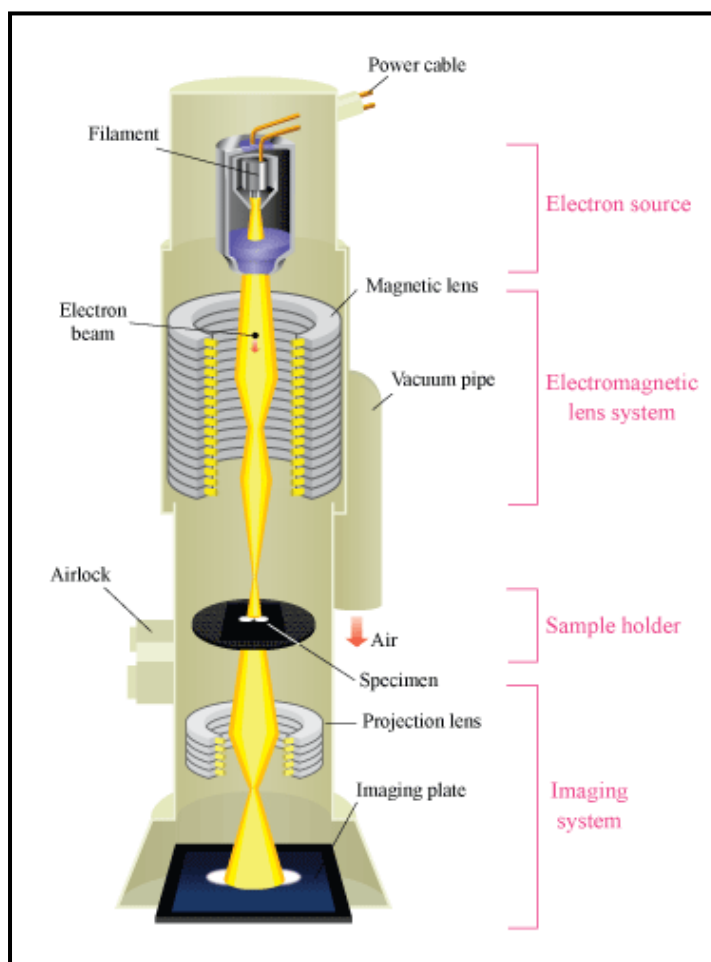


Figure: 2.11The schematic outline of TEM

http://www.hk-phy.org/atomic_world/tem/tem02_e.html

2.7.2. Scanning Electron Microscopy (SEM)

Scanning electron microscope is one of the most repeatedly used characterization tools due to large depth of focus, high resolution and ease of applicability for morphological analysis. Here a well-focused mono-energetic ($\sim 25\text{KeV}$) beam is

incident on a solid surface (1 nm in diameter) of the material and scanned back and forth. This type of scanning is called as 'Raster scanning'. Backscattered electrons and secondary electrons are important for SEM application; The intensity of secondary electrons is mainly dependent on the atomic number of elements present in the specimen. This also helps in generating the brightness of the spot.. The electron beam is scanned over the specimen surface which is synchronized with the cathode ray tube (C.R.T). The signals are collected from various points and the map area is displayed on C.R.T. screen. In short, information about the sample's surface topography, composition is obtained. The ray diagram ^[21] of SEM is shown in **Figure 2.12**. In the present work the Scanning electron images are recorded on FEI-Nova Nano SEM at National Chemical Laboratory, Pune.

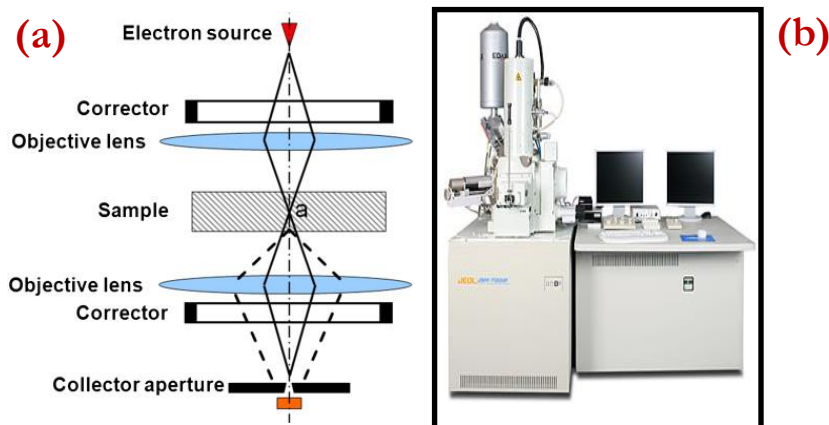


Figure 2.12 (a) Pictorial represent the principle of scanning electron microscope [Reproduced with permission from ref no. 21] and (b) photograph of (FEI-Nova Nano SEM machine).

2.7.3. Atomic Force Microscopy (AFM)

Atomic force microscopy (AFM) is as an important technique for the topography/morphology analysis. In the case of layered materials this technique can be used to determine the number of stacked layers.^[22] AFM has also been verified as a helpful tool to determine the mechanical properties of graphene based materials. Moreover AFM has helped in the study and understanding

mechanical properties of DNA, proteins and cells, polymers. AFM allows studying 3D profiling of sample surfaces at the atomic scale. This is possible by determining the forces between a probe (<10 nm), and the sample surface. Typical proximity is ~ 0.2 – 10 nm. Initially the probe is supported on a cantilever (typically made of Si_3N_4 or Si). Laser beam from the cantilever is reflected towards a sensitive photodiode (detector), where the cantilever deflections are monitored. These deflections are take place as the tip moves over

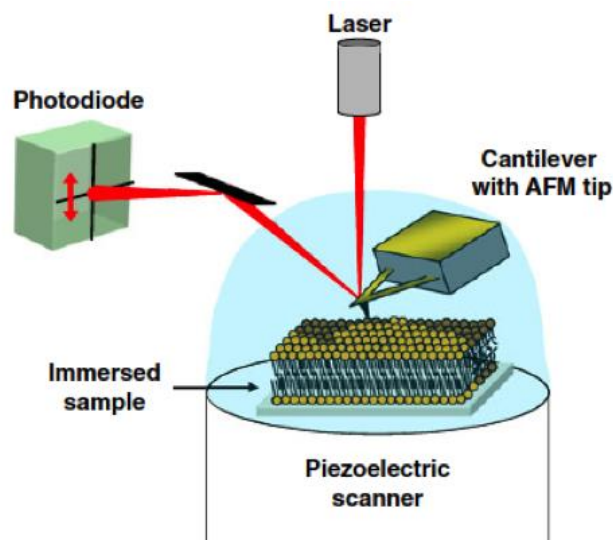


Figure 2.13 AFM set up.

http://physwiki.ucdavis.edu/Wikitexts/University_of_California_Davis/UCD%3ABiophysics_241/AFM_on_Membranes

the sample. A 3D image of the sample under study is occurred by recording the deflections along z axis, as a function of the sample's lateral positions. A typical set up of an AFM is shown in **Figure 2.13**

2.8 Raman Spectroscopy

In contrast with other conventional spectroscopic tools, Raman spectroscopy deals with the scattering of light and not with its absorption.^[23] In Raman analysis the sample is exposed to a laser source whose wavelength is either in ultraviolet, visible or near infrared light range. The scattered light is collected with a series of

lenses and finally forwarded towards a spectrophotometer to get a spectrum known as Raman spectrum. If the frequency of scattered light is having same energy as the incident light, the process is known as elastic collision or termed Rayleigh scattering. On the other hand if the collision is inelastic, the scattered photon will have either a higher or lower energy termed as Raman scattering. This scattering is further divided into two types: Stokes scattering; and Anti-Stokes scattering. In Stokes scattering the frequency of scattered light is decreased while in anti-stokes scattering it increases. The shift in Raman is specific and gives very important information about vibrational-rotational changes in the sample.

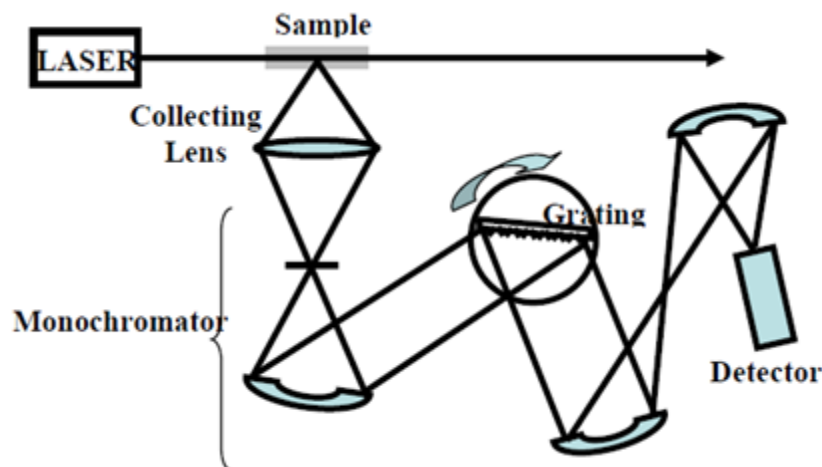


Figure 2.14 Basic diagram for Raman spectrometer.

Raman Spectrometer (**Figure 2.14**) consists of a Laser beam (very narrow, monochromatic, coherent and powerful) that is passed through a transparent cell, consist of narrow quartz tube filled with the sample. The scattered light is collected by a lens and passed into a grating monochromator. The signal is measured by a photomultiplier tube (PMT) and further upon amplification Raman spectrum is plotted.

2.9 X-ray Photoelectron Spectroscopy (XPS)

The foundation to electron spectroscopy was laid way back in the year 1887 when Heinrich Hertz discovered the photoelectric effect. However, it took more than half a century further to establish the photoelectron spectroscopy as a technique. In 1950, Kai Siegbahn reported the first successful study of photoelectron spectroscopy for which he received the Nobel Prize for Physics in 1981.^[24] They named this technique as Electron Spectroscopy for Chemical Analysis (ESCA). Later it got modified to X-ray photo electron spectroscopy (XPS). XPS is widely used for identification of compounds and changes in its chemical structure. For example, an oxide exhibits a different spectrum than a pure element (SiO_2 on Si for example).

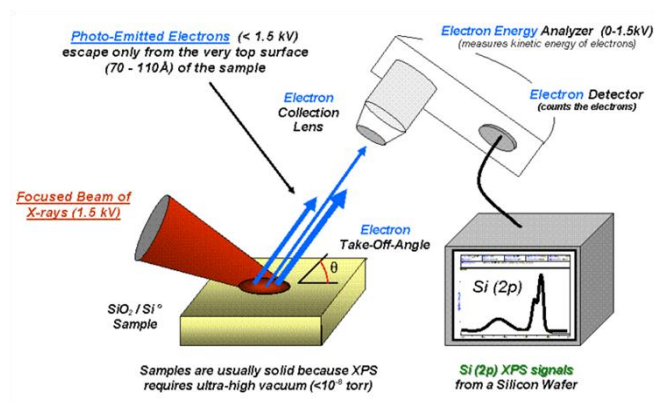


Figure 2.15 basic diagram for XPS

http://en.wikipedia.org/wiki/X-ray_photoelectron_spectroscopy.

Elements are identified by the peak positions on the XPS spectrum. Concentration determination using Peak heights and peak areas can be used with appropriate correction factors. An XPS spectrum is obtained by irradiating a sample with X-ray beams and measuring the kinetic energy and number of electrons ejected from the surface of the sample. This technique requires ultra-high vacuum (UHV) conditions. X-ray photoelectron spectroscopy helps to measure the empirical formula, chemical state, elemental composition, and electronic state of elements exist in a sample. The basic diagram for XPS system is shown in **Figure 2.15**

2.10 Photo-thermal deflection spectroscopy

Photothermal deflection spectroscopy (PDS) technique was first proposed in 1981 by Jackson et.al.^[25] The working principle of this technique is based on ‘mirage effect’. In general, the rays of light passing through a medium at low angles refract their straight path due to thermal gradient induced in the medium. This can be experienced on sunny days when an illusion of water is observed on a road at a distance. This refraction of light is mainly used in the working of PDS technique.

PDS is highly sensitive absorption technique which can measure absorption coefficients of down to 1cm^{-1} or absorbance down to 10^{-5} .^[26] Such high sensitivity is achieved at room temperature. PDS techniques are mainly of two types: transverse and collinear PDS respectively. Both the systems have tunable monochromatic excitation source at a fixed wavelength and probe laser to probe the absorption in the sample at a given excitation wavelength. In case of collinear PDS, the excitation and probe laser sources go through the sample and are arranged in such a way that they overlap each other in the sample. While in transverse PDS configuration, the excitation source is normal to the plane of the sample and the probe laser is perpendicular to the excitation beam path. We have used transverse PDS technique for analysis in this thesis.

This technique is very important to understand the optical and electronic properties of the semiconductors in thin film form. In real semiconductor, absorption beyond band edge takes place and it later shows exponential decay below the band gap. These exponentially decaying tail states are known as Urbach tail. The absorption coefficients (α) for semiconductors is given as follows

$$\alpha \propto \exp\left[-\frac{E - E_g}{E_0}\right] \quad \text{for direct band gap semiconductor}$$

$$\alpha \propto \exp\left[-\frac{E - E_g}{E_0}\right]^2 \quad \text{for indirect band gap semiconductor}$$

The term Urbach energy (E_g) gives information about the structural order in a material. The Urbach energy can be calculated from the inverse slope of the linear fit to the Urbach tail in the absorption spectra plotted on natural logarithmic scale.

Section III: Fabrication of Dye sensitized solar cells (DSSC) and Light emitting diodes (LED)

This section covers the details of fabrication protocols used for DSSC and perovskite based light emitting diodes which are demonstrated in this thesis. The fabrication of high efficiency DSSC and LED based devices is composed of multiple steps which are either interlinked or independent of each other for obtaining high reproducibility.

2.11 Fabrication of DSSC

2.11.1 Substrate Cleaning

For DSSC fabrication we have used fluorine doped tin oxide (F:SnO₂, FTO) with 80% transparency and 12Ω/sq. sheet resistance. FTO glass was cut into 2 * 2 cm square pieces and cleaned thoroughly by sonicating them in different solution sequentially as follows:

- Soap solution for 15 minutes.
- Rinse with deionized water.
- Sonicate in isopropanol for 15 minutes.
- sonicate in acetone for 15 minutes.

2.11.2 Preparation of working electrode

Blocking layer of TiO₂: A compact layer of TiO₂ thin film (about 50 nm) is coated on to the cleaned FTO substrate by spin coating process. This compact layer act as hole blocking layer which avoids the recombination of liquid electrolyte with the photo-injected electrons. To prepare blocking layer 1mL of titanium tetraisopropoxide (TTIP) is mixed with 5mL ethanol and 0.5mL glacial acetic acid. This solution was spin coated on to the substrate at 2500 rpm for about 1 minute. Later the FTO substrates were annealed at 450⁰C for 1 hour.

TiO₂ Photoanode deposition (Doctor Blading process): commercially available TiO₂ (sigma Aldrich) of 21 nm size are mixed with ethyl cellulose (Sigma

Aldrich) as binder and α -terpineol (ACROS) as surfactant. Many steps are involved in this paste making protocol. The details of this process are given in reference no 27. Using this method we can make uniform film with about 40-50% optical transparency which was beneficial for us to study the light harvesting ability of our TiO_2 and $\text{Au}:\text{TiO}_2$ nanofibers.

For 'Doctor Blading' the FTO substrates were masked with scotch tape. The TiO_2 paste was poured on one of the edge and then spread over till the other end using glass rod or glass slide. The as coated film was allowed to dry in air for 10 minutes then heated at 450°C for one hour.

In order to apply light harvesting layers TiO_2 nanofiber paste was also prepared using above mentioned protocol. After sintering of TiO_2 nanoparticles film we have coated TiO_2 nanofibers paste by doctor blading. Films were further annealed at 450°C for one hour.

2.11.3 TiCl_4 treatment: 0.5mM TiCl_4 solution was prepared by pouring 0.55mL of TiCl_4 in ice made from 100mL of DI water. Later the ice is allowed to melt completely. Doctor bladed TiO_2 films are dipped into this solution and then subjected to 70°C for 30 mins. This step provides the pore filling inside the TiO_2 nanoparticulate film and also gives good connectivity between the nanoparticles which is essential for better charge transport. After TiCl_4 treatment films are again annealed at 450°C for 30 mins

2.11.4 Dye Sensitization: For anchoring of dye molecules the films are then soaked in dye solution for 24 hours. This step converts the white TiO_2 film in the dark red colored dye loaded film. We have used N719 dye in the present thesis. 0.5mM dye solution is prepared by dissolving the N719 dye in tert.-butyl alcohol and acetonitrile solvent (50:50 v/v)

2.11.5 Counter Electrode preparation: Counter electrode is prepared by drop casting ethanolic solution of 0.6M H_2PtCl_6 on FTO substrate. The solution was dried at room temperature and later annealed at 450°C for 15 mins in air. This step reduces platinum salts to Pt nanoparticles.

2.11.6 Electrolyte solution preparation : The I/I_3^- redox couple was prepared by dissolving 0.05M lithium iodide (LiI), 0.05M Iodine (I_2), 1M 1-propyl-2,3-dimethyl-imidazolium iodide (DMPII), and 0.5M 4-tertbutylpyridine (TBP) in acetonitrile/valeronitrile solution (v/v 1:1).

2.11.7 DSSC device assembly: To study the performance of DSSC device the working electrode and counter electrode is assembled together. Dye loaded TiO_2 film was scratched mechanically to achieve the working area of 0.25cm^2 . The bare FTO part on the working electrode is masked with the cello tape to prevent the contact of electrolyte with FTO. $100\mu\text{L}$ of electrolyte is injected between working and counter electrode and both the ends were tightly packed by clips. the J-V curves were measured using Newport solar simulator connected to Keithley I-V meter.

2.12 Fabrication of Light emitting Diode: Patterned ITO glass was washed by sonicating in Acetone and isopropanol sequentially for 15 minutes. Oxygen plasma treatment was given for about 1 minute to cleaned substrate. 50nm PEDOT-PSS compact layer was deposited by spin coating aqueous PEDOT-PSS solution at 5000 rpm for 30 seconds. Further films were annealed at 100°C for 30 minutes. A very thin layer of Al_2O_3 is deposited by spin coating ethanolic solution of Al_2O_3 by spin coating. Further films are annealed at 100°C for 15 minutes. Later TBAB treated perovskite films are deposited as mentioned in the film fabrication protocol. A 50 nm electron injection layer comprised of 2:1 blend of 2,2',2''-(1,3,5-Benzinetriyl)-tris(1-phenyl-1-H-benzimidazole) (TPBi) and poly{[N,N'-bis(2-octyldodecyl)-naphthalene-1,4,5,8-bis(dicarboximide)-2,6-diyl]-alt-5,5'-(2,2'-bithiophene)}(N2200). Later LiF/Al (2-3nm/100nm) electrodes were thermally evaporated as a top electrode.

2.13 References

- 1) Huang, Zheng-Ming, Y-Z. Zhang, M. Kotaki, and S. Ramakrishna. Composites science and technology 63, no. 15 (2003): 2223-2253.
- 2) Dalton, Paul D., Cédryck Vaquette, Brooke L. Farrugia, Tim R. Dargaville, Toby D. Brown, and Dietmar W. Hutmacher. Biomaterials Science 1, no. 2 (2013): 171-185.
- 3) Greiner, Andreas, and Joachim H. Wendorff. Angewandte Chemie International Edition 46, no. 30 (2007): 5670-5703.
- 4) G. M. Bose, Recherché sur la cause et sur la véritable thorie de l'électricité, Wittenberg, 1745
- 5) J. F. Cooley, US 692,631, 1902.
- 6) W. J. Morton, US 705,691, 1902.
- 7) A. Formhals, US 1,975,504, 1934.
- 8) W. Simm, K. Gosling, R. Bonart, B. von Falkai, GB 1346231, 1972.
- 9) M. Jacobsen, Chemiefasern/Textilind. 1991, 36 – 41.
- 10) E. Boland, G. Wnek, D. Simpson, K. Pawlowski, G. Bowlin, Journal of Macromolecular Science, Part A. 38 (2001) 1231-1243.
- 11) Dan Li, Yuliang Wang, and Younan Xia, Nano Letters 2003 3 (8), 1167-1171.
- 12) S. N. Reznik, A. L. Yarin, E. Zussman, L. Bercovici, Phys. Fluids 2006, 18, 062101.
- 13) J. H. Yu, S. V. Fridrikh, G. C. Rutledge, Adv. Mater. 2004, 16, 1562 – 1566.
- 14) Shin, Song-Hee, Odnoo Purevdorj, Oscar Castano, Josep A. Planell, and Hae-Won Kim. Journal of tissue engineering 3, no. 1 (2012): 2041731412443530.

- 15) Sener, A.G.; Altay, A.S.; Altay, F., *Electrical and Electronics Engineering (ELECO)*, 2011 7th International Conference on , vol., no.,pp.I-324,I-328, 1-4 Dec. 2011
- 16) Koyal Garg and Gary L. Bowlin *BIOMICROFLUIDICS* 5, 013403 2011
- 17) Darrell H. Reneker', Alexander L. Yarin *Polymer*, Volume 49, Issue 10, 13 May 2008, Pages 2387–2425
- 18) Wu, Jing, Nü Wang, Yong Zhao, and Lei Jiang. *Journal of Materials Chemistry A* 1, no. 25 (2013): 7290-7305.
- 19) W. W. Flack, D. S. Soong, A. T. Bell, and D. W. Hess, *J. Appl. Phys.*, 1984, 56, 1199.
- 20) *Elements of X-ray Diffraction*, ed by B.D. Cullity, Addison Wesley Publishing Co. 1978.
- 21) Peng Wang, G.Behan, A.I. Kirkland, P.D. Nellist, E.C. Cosgriff, A.J.D'Alfonson, A.J. Morgan, L.J.Allen, A.Hashimoto, M.Takeguchi, K.Mitsuishi, M.Shimojo, *Ultramicroscopy*, 2011, 111, 877.
- 22) Y. Hernandez, V. Nicolosi, M. Lotya, F. M. Blighe, Z. Sun, S. De, I. T. McGovern, B. Holland M. Byrne Y. K. Gun'Ko J. J. Boland P. Niraj G. Duesberg S. Krishnamurthy, R. Goodhue, J. Hutchison, V. Scardaci, A. C. Ferrari and J. N. Coleman, *Nat. Nanotechnol.*, 2008, **3**, 563.
- 23) D. A. Long, *Raman Scattering*, Mcgraw Hill Book Company, New York, **1977**.
- 24) C. Nordling, S. Hagströmand K. Siegbahn, *Z. Phys.*, 1964, **178**, 433.
- 25) W. B. Jackson, N. M. Amer, A. C. Boccara, and D. Fournier, *Appl. Opt.*, vol. 20, no. 8, pp. 1333–1344, 1981.
- 26) A. Sadhanala, F. Deschler, T. H. Thomas, S. E. Dutton, K. C. Goedel, F. C. Hanusch, M. L. Lai, U. Steiner, T. Bein, P. Docampo, D. Cahen, and R. H. Friend, *J. Phys. Chem. Lett.*, vol. 5, no. 15, pp. 2501–2505, 2014.

- 27) Ito, Seigo, Peter Chen, Pascal Comte, Mohammad Khaja Nazeeruddin, Paul Liska, Peter Pechy, and Michael Grätzel. Progress in photovoltaics: research and applications 15, no. 7 (2007): 603-612.
- 28) Sapountzi, Eleni, Mohamed Braiek, Carole Farre, Madjid Arab, Jean-François Chateaux, Nicole Jaffrezic-Renault, and Florence Lagarde. Journal of The Electrochemical Society 162, no. 10 (2015):B275-281.

Chapter 3

Plasmonic Light harvesting of Dye sensitized solar cells by Au-nanoparticles loaded TiO₂ nanofibers.

In this work, We report significant enhancement in the performance of dye sensitized solar cells by using in situ Au nanoparticle (Au NP) loaded TiO₂ nanofibers (Au: TiO₂ NFs) as the light harvesting (LH) layer as compared to the use of only TiO₂ nanofibers (NF) as the LH layer. The Au NP: TiO₂ nanofibers are prepared by electro-spinning via a precursor mixture whereby nanostructured porous TiO₂ nanofibers are formed and get in situ loaded with only 4-5 nm AuNPs. The as-synthesized nanofibers are characterized by x-ray diffraction, Raman, Photoluminescence (PL) and Mott-Schottky analysis. The presence of gold nanoparticles shows considerable improvements in light harvesting and the electrochemical properties of TiO₂ nanofibers. A remarkable enhancement in efficiency by 25% is achieved with the Au NF LH layer as compared to 12% by NF layer, over the value without any light harvesting layer. The IPCE and impedance analyses reveal commensurate improvements. The impedance study shows a decrease in the transport resistance (R_{TiO_2}) and an increment in the chemical capacitance and life time of the solar cell. Systematic analyses of the optical properties suggest that the enhanced light harvesting by Au NP loaded TiO₂ nanofibers is caused by the role of plasmon-polariton modes at the distributed nanoscale Schottky junctions in the Au:TiO₂ nanofibers.

*The content of this chapter has been published in “*Journal of Material Chemistry A*, 2014, 2(4), 975-984. Reproduced by permission of The Royal Society of Chemistry

3.1. Introduction

In optoelectronics, in general, and photovoltaics in particular, use of nanostructures of precious metals (high electron density) has been attracting considerable attention lately in view of the associated novel plasmonics effects and other beneficial factors related to light scattering, fluorescence, charge transfer, and local field enhancement.^[1-5] Such metal nanostructures allow controlled manipulation of optical absorption and scattering phenomena over the visible spectral range of interest to photovoltaic devices.^[6] Plasmonic effects have been used to enhance the performance of the conventional as well as next generations of solar cells designs.^[7] Moreover, novel plasmonic solar cell concepts have been proposed and are being actively investigated. A number of interesting phenomena have also been reported in the context of the optical response of an ensemble of metal nanoparticles depending on their size, shape, distributions, and the properties of the embedding matrix. This latter work is still primarily in the realm of fundamental science and has not yet been fully and effectively examined in the domain of light harvesting (LH) commensurate with its projected promise. To the best of our knowledge there are hardly any reports on the specific aspect of plasmonic functionalization of light-harvesting architecture in the dye sensitized solar cell context other than a recent interesting work on the use of topologically ordered gold nanoparticles as counter electrode in order to enhance the light trapping in the TiO₂ film. This strategy has shown an enhancement in efficiency by 17%.^[8] In this work we have examined the AuNP related light harvesting aspect in some details by employing in situ formed Au nanoparticle (AuNP) loaded anatase TiO₂ nanofibers prepared by electro-spinning as a LH top layer in a dye sensitized solar cell (DSSC) assembly and have compared its effects with a similar layer but without Au NPs. Electro-spun nanofibers without AuNPs have been shown to yield beneficial LH effects in some previous interesting studies.^[9] In neither case have we used Au NPs in the active layer as done in some previous works.^[10-11] We find a remarkable 25% enhancement in the photoconversion efficiency

with the inclusion of AuNPs in the LH layer. We have used a number of characterizations to reveal the possible causes of this enhancement and in the process identified some new interesting effects. Since an LH layer can be applied in different solar cell architectures, the effect reported here may be applicable to other photovoltaic systems as well. Within the last year there have been exciting new developments reported by Grätzel & coworkers and Snaith & coworkers in the field of sensitized solar cells using a hybrid perovskite ($\text{CH}_3\text{NH}_3\text{PbI}_3$ or $\text{CH}_3\text{NH}_3\text{PbI}_2\text{Cl}$) system which exhibits high optical absorption and conversion efficiency.^[12-13] In a related recent remarkable development, Grätzel and coworkers have shown a record efficiency close to 15% for a perovskite based system by the sequential deposition route.^[14] This advance appears to be a game changer for this family of excitonic solar cells and rapid scientific developments pushing the efficiency to even to higher values are expected in the near future. We believe that some of the plasmonic light harvesting ideas discussed in this paper could be beneficial in this regard. Although not in the top LH layer, metal nanoparticles such as gold (Au), Silver (Ag) have been used in the DSSC active layer architectures with beneficial effects.^[15-16] The corresponding surface plasmon induced enhancements in the solar cell performance have been reported and discussed in the literature. Indeed, some design strategies have also been suggested in order to effectively harvest the photons by metal nanoparticles.^[17] Metal nanoparticles (above 40 nm) are considered best light scatterers as compared to large semiconducting nanoparticles.^[18] At lower sizes, metal nanoparticles absorb light efficiently and generate localized surface electron density oscillations known as surface plasmons. For instance, S.Chang et al. have shown enhancement in the sub-wavelength region after incorporating gold nanorods in the active device layer.^[19] Muduli et al. have shown a remarkable conversion efficiency enhancement with Au/TiO₂ plasmonic nanocomposites in the active layer.^[20] TiO₂ nanofibers (without metal nanoparticles) have also been used as the top LH layer once again with beneficial effects. Indeed, Chaungchote et al. have reported impressive 8.14% conversion efficiency (electrode area 0.25cm²) by

using TiO₂ nanofibers as the scattering layer.^[21] Similarly Zhu et al. have shown the use of rice-grain shaped TiO₂ as the best scattering layer with maximum achievable conversion efficiency of 7.45%.^[22] Our work departs from these interesting works in terms of the effective use of Au NPs inside the LH nanofibers for realizing enhanced quality factors in DSSC. In the process we identify and suggest an interesting role of surface plasmon-polariton modes at the distributed nanoscale AuNP/TiO₂ interfaces in the LH layer in the efficiency enhancement.

3.2. Experimental Section

3.2.1. Synthesis of Au/TiO₂ nanofibers:

1g of polyvinyl pyrrolidone (PVP Sigma Aldrich mol wt 13, 00,000 g/mol) was dissolved in 8ml of absolute ethanol (AR Grade). After complete dissolution, 10 μ L of conc. HNO₃ was added. 2ml of Titanium tetra-isopropoxide (TTIP,) was added in the resulting solution and the mixture was further stirred for 2 hrs. After ensuring homogeneity, this solution was subjected to high electric field of about 10 kV for eletrospinning. The tip to collector distance was fixed at 15 cm and the feeding rate was 1mL/hr. The composite fibers thus obtained were dried in an oven at 70⁰C for 5 hrs and then calcined at 500⁰C for 2 hrs at a heating rate of 10C/min. In order to make Au/TiO₂ composite nanofibers the same protocol was followed but an ethanolic solution of HAuCl₄.3H₂O (Sigma Aldrich) was added as gold precursor after acid addition. The ratio of Au :Ti was kept fixed as 1 mol % in the final solution. Thus the AuNPs grew in situ in our fibres during the formation of TiO₂.

3.2.2. Photo-anode preparation:

Fluorine doped tin oxide (FTO) substrates (Solaronix Co. Sheet resistance 7 Ω m-2) were cleaned by sonicating in DI water, and detergent solution for 15 min and then rinsed with ethanol. TiO₂ nanoparticles of about ~ 20 nm were synthesized by the hydrothermal method.^[23] Screen printing paste of these nanoparticles was prepared as mentioned in the reference.^[24] Screen printing

pastes of TiO_2 and Au/TiO_2 nanofibers were also prepared by the same procedure. The homogeneous suspension of TiO_2 nanoparticles paste was dispensed on FTO by doctor blading technique to prepare a semi-transparent nanocrystalline photoanode. The TiO_2 electrode was calcined at 450°C for 1 h to remove the organic components. These photoanodes were then treated with TiCl_4 at 70°C for 30 min and then sintered at 450°C for 30 min. Finally a scattering layer of TiO_2 (NF Cell) or Au/TiO_2 NF (Au NF Cell) was formed and the films were sintered at 500°C for 30 min. The thickness of active layer was kept as $10\mu\text{m}$ and that of harvesting layer $2\mu\text{m}$. The TiO_2 electrode with $12\mu\text{m}$ thickness was also prepared as a reference (NP Cell). These electrodes were then soaked in 0.5 mM N719 dye solution (Solaronix Co.) at room temperature for about 24 hrs. The films were then washed with ethanol and dried. The counter electrode Pt coated FTO was prepared by drop casting a solution of hexacholoplatinate (H_2PtCl_6) and further annealing at 350°C for about 15 min. The cell was assembled by sandwiching the active photoanode and the counter electrode. The space in between was filled by the electrolyte which consists of 0.1 M lithium iodide(LiI), 0.05M iodine(I_2), 0.6M 1-hexyl2,3-methylimidazolium iodide and 0.5M 4-tertbutylpyridine in acetonitrile and valeronitrile (1:1 v:v).

3.3 General Characterization:

The morphology of calcined nanofibers was observed with Scanning electron microscopy. (SEM). High resolution transmission microscopy images (HR-TEM) and SAED pattern were also recorded using tecnai 300 (T-30). The UV-Vis diffuse reflectance spectra (DRS) of nanofibers and solar cell films were recorded in the integrated sphere mode using JASCO V-570 spectrophotometer. The photoluminescence was recorded using HORIBA fluoromax-4C with an excitation wavelength of 330 nm. The J-V characteristics of the assembled DSSCs were measured under exposure to AM1.5, 100 mW/cm^{-2} simulated solar spectrum (Solar simulator, Newport). A standard silicon solar cell was used as a reference for calibration purposes. (SER No. 189/PVM 351). Electrochemical

impedance measurements were carried out using AUTOLAB PGSTAT 30 under light illumination using 10mV ac voltage at applied bias potential ranging from 0.6 -0.75 V in the frequency domain of 1MHz to 0.01Hz. Mott-Schottky plots were also recorded using AUTOLAB PGSTAT 30 under dark conditions. IPCE measurements were performed with the same cell assemblies on Newport IPCE system over the range of 350 nm to 800 nm.

3.4 Results and discussion:

3.4.1 TiO₂ nanofibers and Au: TiO₂ nanofibers characterization:

Electrospinning is a very versatile technique for making 1D elongated structures.^[25] In our case, TiO₂ nanofibers were prepared by calcinating the polymer fibers containing titanium and gold precursors. The calcination process involves the evaporation of organic component and encourages crystallization of TiO₂ nanoparticles. The mean size of TiO₂ nanoparticles which assemble into the elongated quasi-1D fiber form is mainly precursor concentration dependant. In the case of TiO₂/Au nanofibers, the concentration of gold precursor is very low compared to the Ti precursor. Hence while electrospinning these gold ions get distributed in the polymeric fiber fairly uniformly without getting agglomerated. This results in the in situ formation of TiO₂/Au composite nanofibers after calcination. These nanofibers are composed of nanosized TiO₂ with embedded tiny gold nanoparticles dispersed uniformly in the semiconducting oxide matrix. The gold content in the composite nanofibers was further evaluated using EDAX analysis and it showed 1% gold nanoparticles content. **Figure 3.1(a) & (b)** show the SEM images of electrospun TiO₂ and Au/TiO₂ nanofibers. The diameter of most nanofibers is about ~150 nm, though a few fibers with lower diameter are also seen.

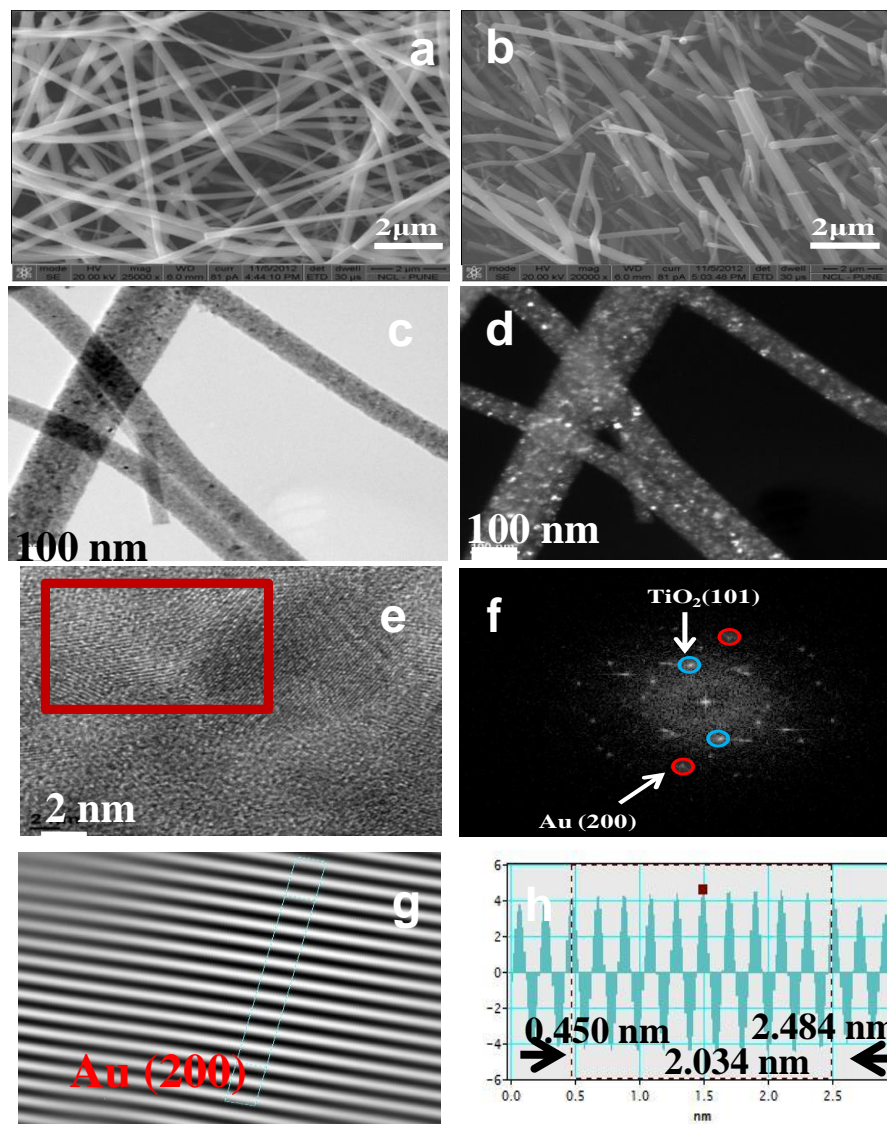


Figure 3.1 (a-b) show the FE-SEM images of TiO₂ NF and Au: TiO₂ NF. **Figure 3.1(c)** shows the dark field image of Au- TiO₂ NFs shown in figure 3.1(d). **Figure 3.1(e)** shows the HR-TEM image of Au-TiO₂ NF at higher magnification. The FFT image of marked portion is shown in **Figure 3.1(f)**. **Figure 3.1 (g-h)** show the Au (200)-specific inverse-FFT pattern and the corresponding lattice spacing.

In order to confirm the presence of gold nanoparticles we recorded dark field (Z-contrast enhancing HAADF) transmission electron image of Au TiO₂ NF **Figure 3.1(d)** to be compared with **Figure 3.1(c)** which clearly shows the bright

spots indicating the presence of gold nanoparticles distributed in the TiO_2 nanoparticle-assembled fiber matrix. **Figure 3.1(e)** shows the HR-TEM image of Au TiO_2 NF. A Fast Fourier transform (FFT) pattern generated for the marked portion is shown in **Figure 3.1(f)**. It shows several diffraction spots representing TiO_2 and gold lattice planes. Since many key planes of the two material systems have close lattice parameters,^[26] we focused on the (200) planes of Au which stands out separately and clearly from TiO_2 . The inverse FFT image generated from the red marked spots indicated in **Figure 3.1(f)** is shown in **Figure 3.1(g)** and the corresponding lattice spacing is indicated in **Figure 3.1(h)**. The observed d-value of 2.034 nm unambiguously identifies the Au (200) planes, completely distinguished from TiO_2 system. Elemental analysis was also performed with FE-SEM (EDAX) which clearly brought out the presence of Au. The elemental mapping of Au TiO_2 nanofibers is presented in **Figure 3.2**.

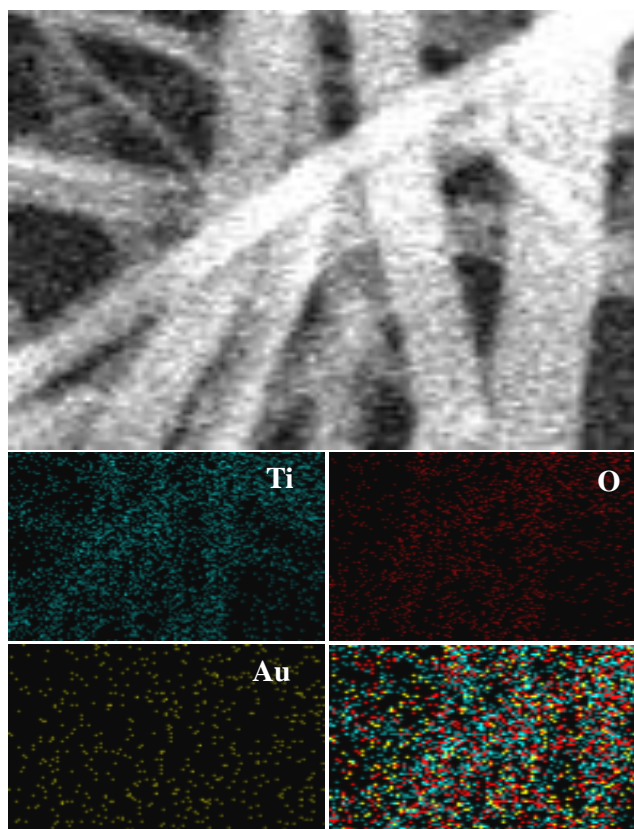


Figure 3.2(a) show the FE- SEM image of Au TiO_2 nanofibers with elemental mapping for gold (Au) Titanium (Ti) and oxygen (O) atoms obtained from the energy dispersive X-ray analysis.

The size of AuNPs is also found to be in the range of 5-10 nm. The X-ray diffraction patterns for TiO₂ NFs and Au: TiO₂ NFs in **Figure 3.3(a)** show that both the nanostructures have anatase phase. [JCPDS 21-1272] In the case of the TiO₂/Au nanofibers broadening of peaks with a slight shift towards lower 2θ (higher-d-value) is observed which can be attributed to the strain on the lattice due to AuNP incorporation. The XRD pattern generally gives the information of long range order of structural arrangements. In order to understand the local imperfections and crystalline defects in Au/TiO₂ composite nanofibers we used more sensitive technique such as Raman spectroscopy. **Figure 3.3 (b)** shows the Raman spectra of TiO₂ NFs and Au:TiO₂ NFs. The Raman active vibration modes E_g (144cm⁻¹), A_{1g} (395cm⁻¹), B_{1g} (514cm⁻¹) and an overtone of E_g (639cm⁻¹) is observed.^[27] The lower energy E_g mode at 144cm⁻¹ clearly confirms the anatase crystalline frame work of the TiO₂ NF and Au:TiO₂ NF. The observed decrease in the intensity for this E_g band for AuNP case is mainly due to surface adsorbed gold nanoparticles.^[11] The absorption of peaks in higher frequency region becomes weaker and broad for the case of Au/TiO₂ nanofibers. This broadening suggests increase in crystalline defects in the framework after gold incorporation. Such crystalline defects serve as additional photoelectron trapping centers in the solar cells which will suppress the charge recombination.^[28] This result was consistent with the XRD results which also confirm the broadening of diffraction peaks suggesting the gold nanoparticles induced lattice strain in TiO₂ framework. This correlation between macro and micro level analysis techniques also confirms the distribution of gold nanoparticles in TiO₂ matrix. **Figure 3.3 (c)** shows the diffuse reflectance spectra (DRS) obtained for the as-synthesized powders. The sharp decrease in reflectance around 340 nm corresponds to the band edge absorption of TiO₂. Additionally, a long tail in visible region with a dip centered at 570 nm is observed only in Au: TiO₂ NFs case. In order to observe this plasmonic contribution we have used simple Kubelka-Munk theory.^[29] Using two flux approximation, this theory introduces two parameters as S and K which relate to the strength of scattering and absorption of the fibers. Y. Borensztein et al.^[30]

have stated the relationship between the parameters S and K with the reflectance of the opaque sample recorded in the integrating sphere assembly. The relationship is given by,

$$\frac{K}{S} = \frac{(1 - R)^2}{2R} \text{----- (1)}$$

We have used the same equation to observe the SPR contribution from gold nanoparticles. **Figure 3.3 (d)** shows the graph of the ratio (K/S) Vs wavelength (nm). It clearly shows the presence of the broad SPR peak centered at 570 nm contributed by the gold nanoparticles. The absorption of visible radiation in the Au/TiO₂ nanofibers is increased over the range of 400 nm to 1000 nm. This confirms the better light harvesting ability of Au/TiO₂ nanofibers as compared to the only TiO₂ nanofibers in the visible and near IR region. It is interesting that the SPR peak in our sample is rather broad and red-shifted (570 nm) as compared to the usual SPR peak observed around 520-530 nm in the case of tiny spherical Au nanoparticles.^[31] Towards this end it is important to note that in our case the Au nanoparticles are embedded in porous TiO₂ fibers with faceted TiO₂ nanoparticles. Thus, they are not uniformly capped all around, but are contacted by TiO₂ surface facets in specific directions. Also, they need not be exactly spherical in view of the concurrent growth of TiO₂ and Au NPs during phase evolution. These factors lead to anisotropy of electron density and therefore red and blue shifted modes. As is known from studies on anisotropic Au nanosystems, the red shift in anisotropic systems can be quite substantial.^[32] Moreover, in view of the size distribution of Au NPs and the differing local environments experienced by different particles, there would be considerable broadening of SPR.

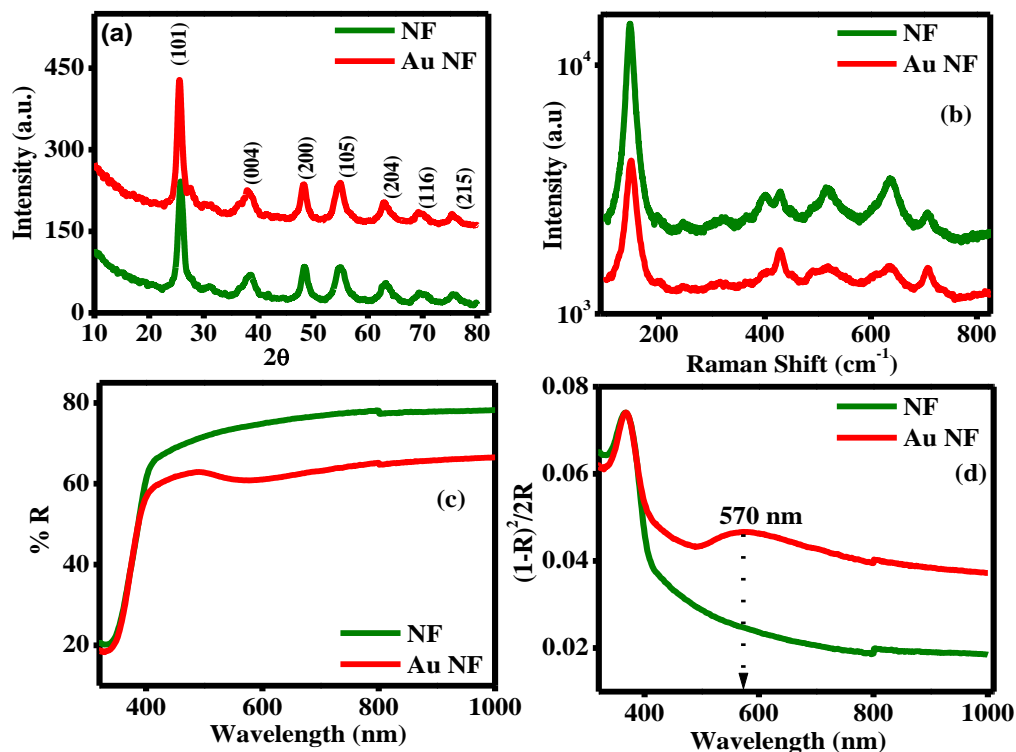


Figure 3.3 (a) show the X-ray diffraction, (b) Raman spectra, (c) Diffused reflectance spectra of TiO₂ NF and Au: TiO₂ NF, (d) show the graph of Ratio (K/S) Vs Wavelength (nm).

3.4.2 Photoluminescence and Mott-Schottky analysis:

As stated earlier we used the NFs and Au: TiO₂ NFs as scattering layers in dye sensitized solar cells and compared their performance. Through various characterizations we could conclude that the use of gold nanoparticles in the harvesting layer is beneficial for both the enhanced light harvesting as well as the improved electrochemical performance of the device. In our study we used 2 μ m thick harvesting layer wherein some dye molecules are also adsorbed. On illumination under sun light this harvesting layer also contributes in the overall device performance. Hence to investigate the optical and electrochemical advantages of gold incorporation in the harvesting domain we performed a comparative photoluminescence study (PL) and Mott Schottky analysis (MS). Towards this end, single layer (2 μ m) of TiO₂ NFs and Au: TiO₂ NFs films were

doctor bladed onto the FTO glass and then annealed at 450°C for 1 hr. These films were used directly without dye loading for further analysis. **Figure 3.4 (a)** shows the photoluminescence (PL) spectra for the TiO₂ nanofibers and Au/TiO₂ nanofibers obtained by exciting the fibers at 360 nm wavelength.

The PL emission intensity can be related to the recombination dynamics of the excited electron and hole pairs. In the Au NF case the two characteristic hump centered at 3.15 eV and 3.3eV are clearly observed that are absent in only NF case. The peak in the region of 3.1-3.3 eV is mainly attributed to the band edge luminescence of TiO₂, and it confirms an enhancement in the photogenerated charge carriers in the presence of gold nanoparticles.^[33] In Au:TiO₂ NF case the luminescence spectrum was not found to be too different as compared to the TiO₂ NF case but the increase in the intensity clearly suggests a greater number of charge carriers in the Au NF case. This enhancement in the band edge luminescence also confirms the shift of Fermi energy towards more negative value and suggests a better charge transporting ability of Au NFs compared to TiO₂ NFs. The inset of **figure 3.4(a)** shows the difference of Au NF and TiO₂ NF case which mainly shows an enhancement in the direct band transition in the presence of gold nanoparticles. The gold nanoparticles thus enhance the separation of electron-hole pair and also suppress the recombination by modifying the defect-related band states.

Figure 3.4 (b) shows the Mott Schottky analysis of the pure NF and Au: TiO₂ NF films in the presence of electrolyte (I/I_3^-). For Mott Schottky analysis we prepared the electrolyte consisting of 0.05M I₂ (Iodine) and 0.5M LiI (Lithium iodide). The positive slope shows the n-type behavior of TiO₂ and Au/TiO₂ nanofibers. The flat-band potential can be obtained by the intercept on x-axis by the linear region of the curves. The flat band potentials observed in our study were -0.9 V and -0.66 V (Vs Ag/AgCl) for TiO₂ NF and Au:TiO₂ NF case respectively. The flat-band potential for Au: TiO₂ NF is clearly shifted to more negative values. The Fermi energy of gold nanoparticles lies below the conduction band (CB) of TiO₂.^[34] The shift towards more negative value indicates the shift of local density of states (DOS) towards the valance band as

compared to the pure TiO₂ NF case. This negative shift is more favorable for the dye sensitized solar cells performance. The rate of electron injection depends on the difference between the LUMO level of dye and CB maximum of TiO₂.^[35] This favorable negative shift will enhance the electron injection rate from the dye to TiO₂ in the case of Au: TiO₂ NFs due to the presence of gold nanoparticles. The slope of the linear region of MS plot is inversely proportional to the electron density in the sample.^[36] The lower slope values obtained for Au: TiO₂ NFs case suggest the enhanced electron density in the Au: TiO₂ NFs case as compared to only TiO₂ nanofibers. The presence of gold nanoparticles can act as electron sink and hence avoid the recombination of the charges with the electrolyte. This enhanced electron density suggests better charge storing ability of Au: TiO₂ NFs as compared to only TiO₂ NF. Hence use of these nanofibers in light harvesting layer can serve dual purpose of light harvesting as well as suppressing the recombination rate of the photogenerated charge carriers within the LH layer. The shift in conduction band minimum is also favorable for electron injection from dye molecules.

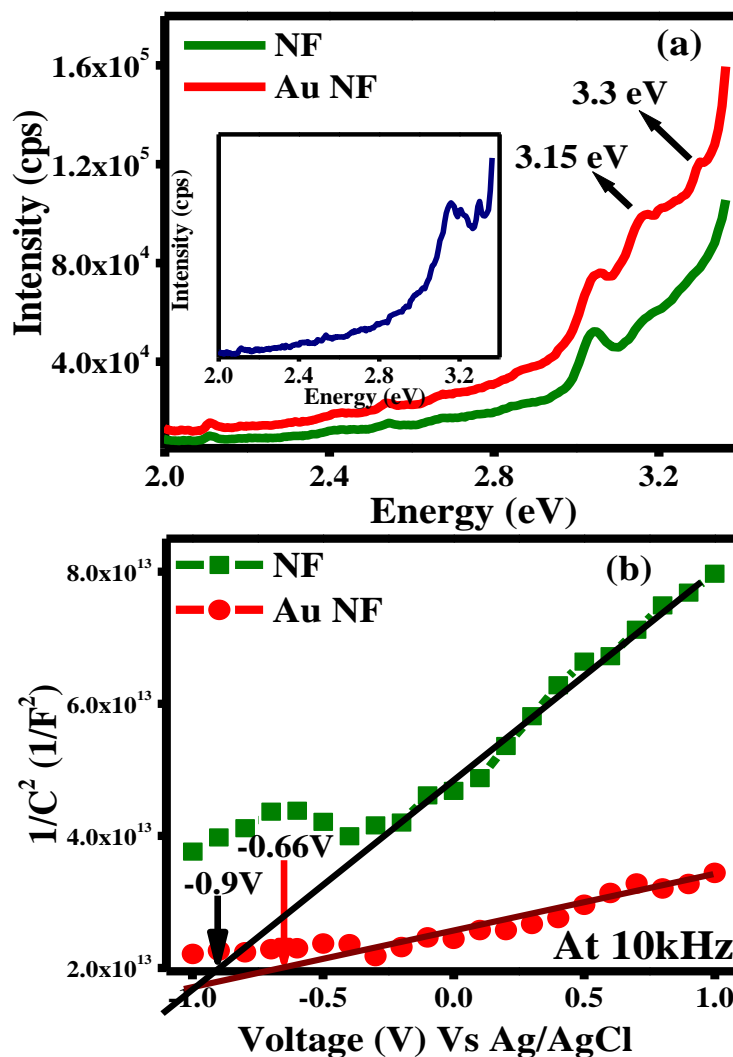


Figure 3.4 (a) show Photoluminescence analysis and (b) show the Mott-Schottky analysis of TiO_2 NF and Au: TiO_2 NF.

3.4.3 Photovoltaic Characterizations:

Figure 3.5 (a) shows the J-V characteristics of the devices measured with an active photoanode area of 0.25 cm^2 under the standard AM 1.5 simulated sunlight. Table 1 gives the measured solar cell parameters. Compared to the case of TiO_2 NP cell without any LH layer ($\eta = 6\%$) the efficiency is enhanced to 6.7% with the use of the TiO_2 NF LH layer in DSSC. This performance improvement is reflected in an increase in the short circuit current density and fill factor of the device, consistent with previous reports.^[22] When Au: TiO_2 NFs

are employed as the top LH layer the enhancement in the current density is quite significant. Additionally the fill factor of the device is also seen to improve considerably. This clearly shows that Au: TiO₂ NFs further enhance the current generation in the device and also help in reducing the recombination.

There is a general concern about the electrolyte attack on metal nanoparticles such as the Au NPs in our case. Towards this end it is useful to point out that in our case due to the in situ formation of Au NPs concurrently with nano-assembled TiO₂ fibers, Au NPs are mostly incorporated in the bulk, though some concentration on the surface is unavoidable. Since our fibers are dense, the inner Au NPs will be fairly well protected from the electrolyte attack but further engineering is clearly needed to address this issue.

Case ID	Voc (V)	Jsc (mA/cm ²)	FF (%)	η %	Dye Loading (mol/cm ³)
NP Cell	0.74	13.47	60.6	6.03	1.52x 10 ⁻⁶
NF Cell	0.76	13.9	63.5	6.76	1.37 x 10 ⁻⁶
Au NF Cell	0.77	15.1	66.8	7.77	1.12 x 10 ⁻⁶

Table 1: Photocurrent Density - Voltage Characteristics for NP Cell, NF cell and Au NF Cell.

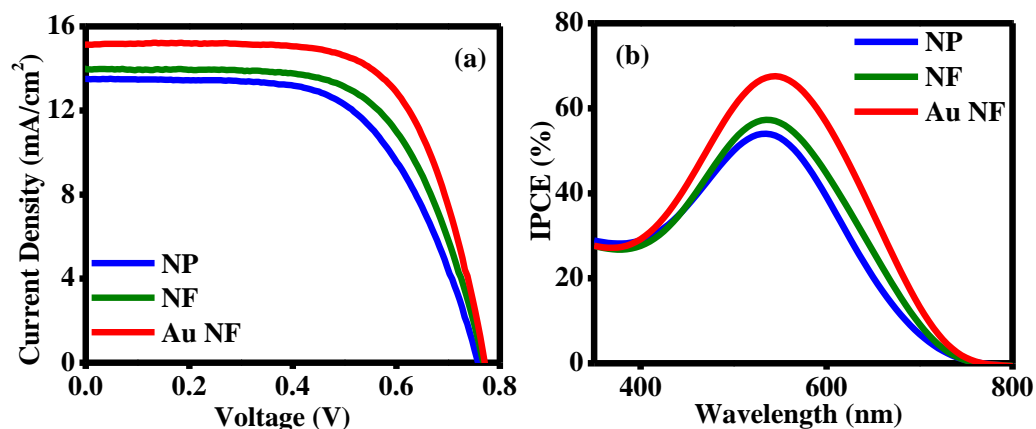


Figure 3.5 (a) shows the J-V curves for NP Cell, NF cell and Au NF cell, (b) shows the Incident Photon to Current Conversion (IPCE) analysis for NP Cell, NF cell and Au NF cell.

Name	V_{oc} (V)	J_{sc} (mA/cm ²)	FF %	η (%)
NP Cell	0.74	13.47	60.6	6.03
NP + Au NF Cell (3 mol%)	0.76	16.51	51.4	6.42
NP + Au NF Cell (5 mol%)	0.75	16.45	50.5	6.29

Table 2: Photocurrent Density (J) – Voltage (V) Characteristics for NP Cell and NP + Au NF Cell with 3 mol% and 5 mol% as Au: Ti ratio

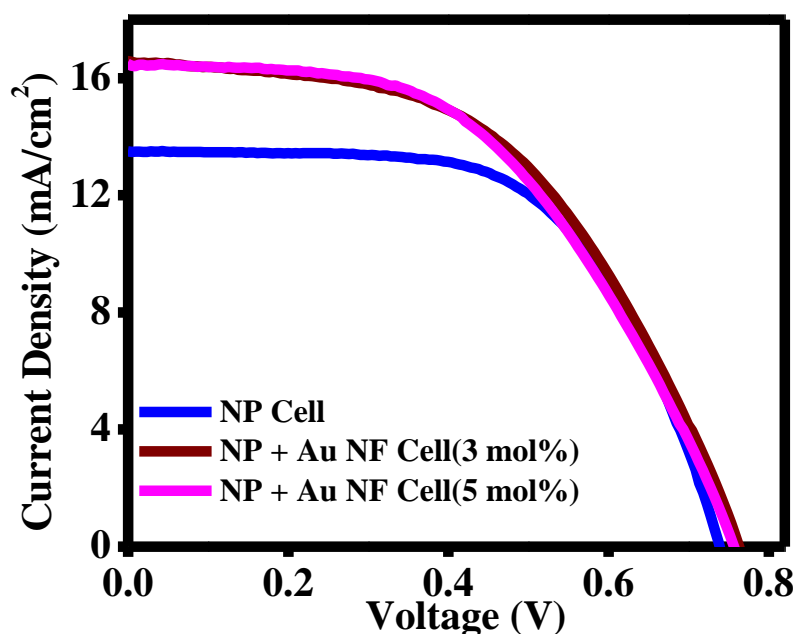


Figure 3.6 shows J-V characteristics for TiO₂: Au nanofibers with 3 mol% and 5 mol% Au: Ti ratio.

We have also checked the effect of gold nanoparticle concentration in TiO₂ NFs by varying the gold precursor ratio to 3 mol % and 5 mol %. The enhanced concentration showed enhancement in the current density (JSC) but the fill factor values of the devices were found to decrease dramatically. Increase in gold ions concentration results in larger particle size. Gold nanoparticles with

larger diameters mainly act as recombination centers. Hence decrease in fill factor is mainly because of enhanced recombination of charges in the device interior. The solar cell parameters and J-V curves are given in **Table 2** and **Figure 3.6**. Hence we decided to carry out our further studies on 1 mol % case. The dye loading in the cells with light harvesting (LH) layers was found to decrease marginally as compared to the only NP layer cell, yet the performance was seen to improve due to LH effects. The harvesting layer(s) comprise of nanofibers film(s) which basically have lower effective surface area as compared to TiO₂ nanoparticles and hence less number of binding sites for dye molecule (Please note that the total thickness of all three films is the same). Moreover, when we compare Au TiO₂ NF case with only TiO₂ NF case, presence of some Au NPs on the surface of the TiO₂ nanofibers decreases the overall available surface area for dye molecule attachment. **Figure 3.5(b)** shows the incident photon to current conversion efficiency (IPCE) for the photoanodes. By addition of the NF scattering layer the peak IPCE value in the spectrum is seen to have increased by about 6%. On the other hand when an Au: TiO₂ NF layer is used as a top LH layer the peak maximum is seen to be enhanced by 25%, which confirms the significant optoelectronic benefits of the Au: TiO₂ NF LH layer in the cell design and is reflected in the significant efficiency enhancement. Additionally we have noticed slight red shift in peak maximum in Au: TiO₂ NF based cell. This red shift is mainly due to the enhanced light absorption by dye molecules and gold nanoparticles in the red part of solar spectrum. The presence of gold nanoparticles in the scattering layer also helps in enhancing the solar radiation absorption in the higher wavelength range.^[19] This suggests that Au: TiO₂ NFs to be the best candidate for light harvesting as compared to TiO₂ NFs. Moreover these beneficial effects can be clearly noted over the entire spectral range. We will return to discuss the possible origins of these observed effects.

3.4.4 Impedance Spectroscopy:

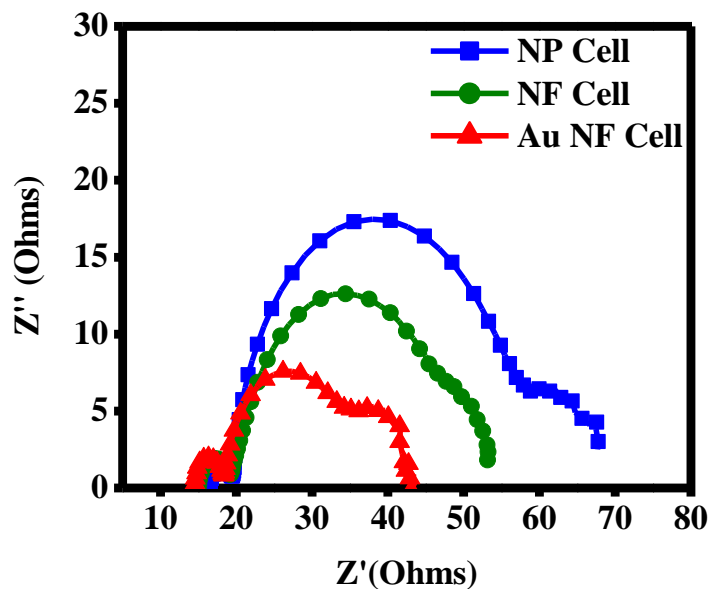


Figure 3.7 shows Nyquist plots for NP Cell (blue), NF cell (olive and Au NF cell (red) at V_{oc} .

To understand the role of AuNPs in the performance improvement, electrochemical impedance spectra (EIS) were recorded under different applied bias voltages under 1 Sun illumination. The Nyquist plot for these solar cells is given in **Figure 3.7**

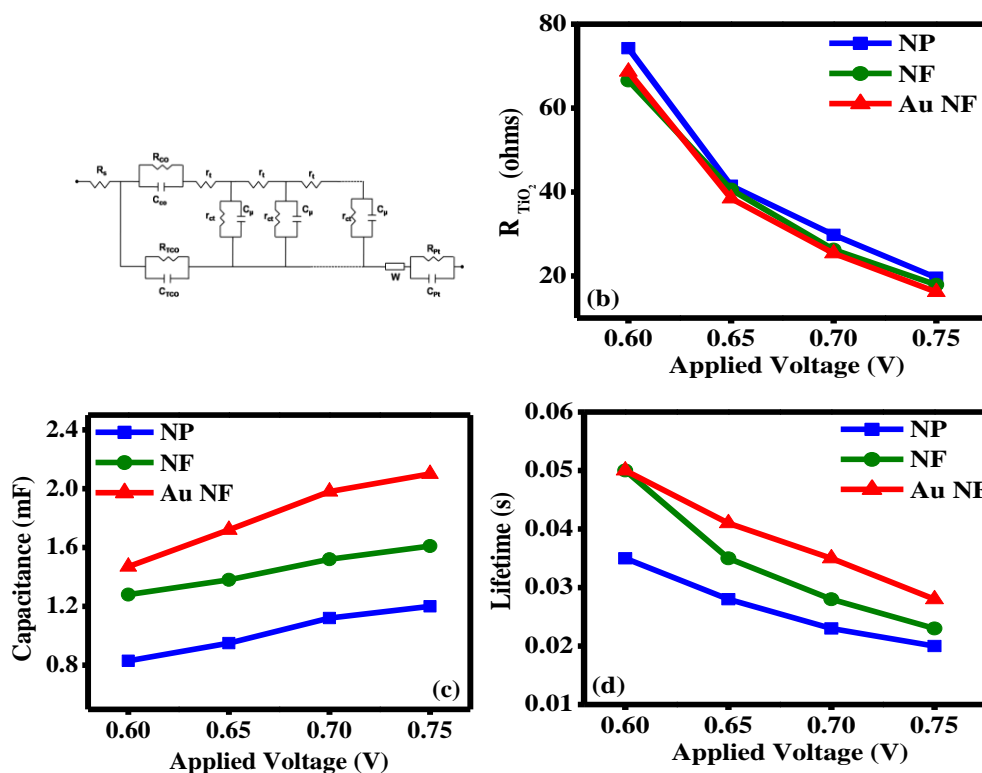


Figure 3.8(a) shows the Transmission Line model used for fitting the EIS curves, (b) Show the variation of transport resistance (R_{TiO_2}), (c) shows the variation of Chemical Capacitance (C_{μ}) Vs applied Bias Voltage for NP Cell, NF cell and Au NF Cell, (d) shows the Life time obtained from the Bode phase plots over the applied bias range for NP cell, NF cell and Au NF Cell.

The EIS spectra can be used to derive the information regarding interfacial and transport processes, and the kinetics of diffusion and recombination. The generally accepted transmission line model was used to fit the plots as shown in **figure 3.8 (a)**.^[37] In Impedance spectroscopy the three semicircles are observed accounting for three different processes: a) the higher frequency region corresponds to the platinum/electrolyte interface (Z1), b) information regarding TiO_2 /dye/electrolyte can be obtained with the middle semicircle (Z2) and c) the lower frequency region gives information about the percolation of electrolyte in

the TiO₂ films (Z3). The parameters such as photoanode resistance (R_{TiO_2}), life time (τ) and Capacitance (C_{μ}) are also derived from the Nyquist plots.

Figure 3.8 (b) shows the graph of R_{TiO_2} vs applied bias voltage. The charge transport resistance (R_{ct}) is seen to decrease when the LH layer is employed over the entire range of applied bias potential. In the case of Au: TiO₂ NFs LH cell the R_{ct} is even lower as compared to the NF LH cell without Au NPs. This implies an increase in the charge transfer rate from dye to TiO₂ in the presence of the Au TiO₂ NF LH layer. This is consistent with the improvement in the fill factor which also suggests the lowering in charge recombination process.

From **figure 3.8 (c)** it can be clearly observed that in the presence of Au:TiO₂ NF LH layer the chemical capacitance (C_{μ}) in the photoanode is enhanced. In dye sensitized solar cells the chemical capacitance means the TiO₂ photoanode connected to working electrode and the whole electrolyte connected to the counter electrode.^[38] The capacitance observed in this study mainly attributes to the total density of electronic states in the conduction band as well as in the band tail states.^[39] The chemical capacitance also indicates the recombination with electrolyte and the electron density in the active layer. Hence the enhancement in C_{μ} in the LH layer employed devices indicates better charge storing ability of TiO₂ NFs and Au:TiO₂ NFs. As revealed by SEM/TEM data the nanofibers are composed of assembled TiO₂ nanoparticles where the grain boundaries of TiO₂ nanoparticles are connected. The electrons can be rapidly driven from one end to another in the TiO₂ nanofibers as compared to the TiO₂ nanoparticle films. The grain-connected TiO₂ nanoparticles in nanofibers can carry higher charge carriers as compared to the randomly connected nanoparticles, hence the capacitance in the case of nanofibers is greater as compared to the only nanoparticle cell.^[40] But in Au: TiO₂ NF LH cell the capacitance is even higher than the TiO₂ NF cell. The enhancement in the capacitance can be attributed to formation of randomly distributed Au:TiO₂ Schottky barriers in the Au: TiO₂ NFs. These Schottky barriers can store the charge effectively leading to an enhancement in the life time. The Fermi energy level of gold nanoparticles is below to the conduction band of TiO₂. Hence such

Au/TiO₂ interfaces form the charge trapping centers leading to higher electrochemical capacitance. The PL spectra also show an enhancement in the non-radiative decay of excited charges suggesting alternate pathways for the photo-generated carriers. The overall capacitance is enhanced almost by 90% as compared to TiO₂ NP case with Au:TiO₂ NFs and by 40% with the TiO₂ NFs. The enhancement in the capacitance is in good agreement with the enhanced life time of the charges. The frequency maximum (ω_{\max}) of the middle semicircle in the Nyquist plot represents the life time of photogenerated charges. **Figure 3.8 (d)** shows that the life time of photogenerated charges is enhanced by employing the light harvesting layers. In the presence gold nanoparticles the life time is higher as compared to only TiO₂ NF case over the entire range of applied bias potentials. This ensures the better performance of the devices even under ambient light conditions.

3.4.5 Optical Characterization of NF Cell and Au NF Cell:

In order to understand the optical effects responsible for the observed performance improvements specific to Au NP incorporation in the quasi-1D TiO₂ nanofibers, we performed additional optical measurements. Specifically, to gain a direct access to the optical effects in the active layer, active layer-LH interface and the LH layer without the interference of the supporting glass, we chose to make inverted cell structure as shown in the **Figure 3.9 (a)**. We prepared a completely inverted assembly of the device structure as shown in the figure. In actual solar cells light enters through the FTO side and then passes through the active layer and finally interacts with the light scattering layer. The light reaching to the active layer is diffused due to the almost 10 μm thick active layer. In order to get more insight about the light scattering ability of LH layer one needs to understand that the scattered light should reach to the detector of the integrated sphere. Additionally the transparent conducting oxide used here as a working electrode has highest transparency to the light. Hence to observe the effect of scattering layer we first deposited the LH layer (2 μm) and on the top of this layer we deposited the active layer of TiO₂ NP (thickness \sim 10 μm).

This film with inverted assembly of the real solar architecture was used to record the diffuse reflectance spectra (DRS).

The DRS of films (without dye loading) were recorded using integrated sphere geometry. **Figure 3.9 (b)** shows that as compared to the TiO₂ NP Cell without any LH layer; the LH layer-incorporated cells (TiO₂ NF cell and Au: TiO₂ NF cell) show significantly higher reflectance which can be attributed to better light scattering abilities of TiO₂ NFs and Au:TiO₂ NFs. It should be noted that the peculiar nature of diffuse reflectance of the NP cell is due to the semitransparent nature of the film on transparent glass substrate. Interestingly, in the case of the Au: TiO₂ NF LH cell, the reflectance is found to be lower as compared to the TiO₂ NF cell.

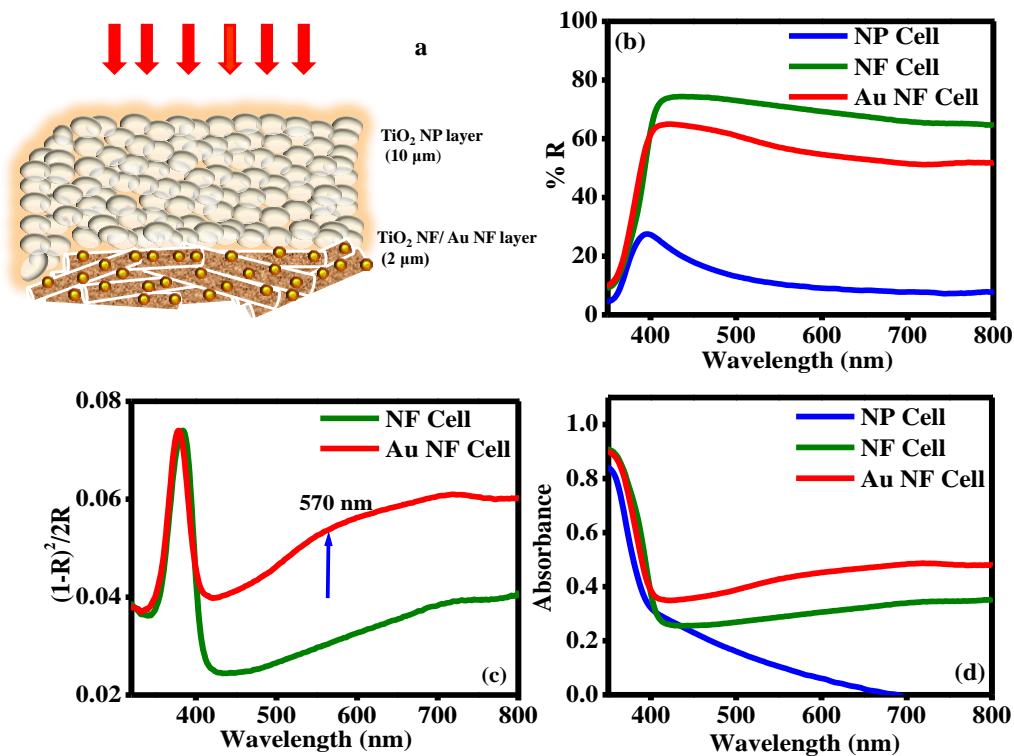


Figure 3.9 (a) shows the schematic diagram to show the specially prepared films for Diffuse reflectance spectrum study, **(b)** shows the reflectance data of NP Cell, NF cell and Au NF cell recorded using integrated sphere **(c)** shows the graph of ratio (K/S) Vs Wavelength (nm), **(d)** Shows the Absorbance of these films calculated using Equn $(A = 100 - \%R - \%T)$.

In order to elucidate the effect of light harvesting layer more clearly we used equation (1) and the ratio of K/S was evaluated from the reflectance data shown in **Figure 3.9 (b)**. The $K/S = [(1-R)^2/2R]$ values are presented in **Figure 3.9 (c)**. It may be noted that in the NF-cell case as well as in the Au-NF-cell case, the K/S gradually increases towards higher wavelength. This is due to better light scattering ability afforded by nanofibers. It may be recalled that for diffuse reflectance study we had purposefully prepared films with inverted cell assembly. Noting that the y-axis in **Figure 3.9 (c)** is actually $K/S = (1-R^2)/2R$, decreasing R (which is the diffuse reflectance) increases the K/S ratio. Since R is seen to decrease progressively with increase of wavelength in the sub-band gap region due to semitransparent nature of the NP component of the film in all three cases. [**Figure 3.9(b)**], the K/S contribution is seen to increase gradually towards the higher wavelengths in **Figure 3.9 (c)**. The presence of gold nanoparticles in the LH layer enhances the optical path length in the device interior over the entire visible wavelength region, as shown in **Figure 3.9 (b and c)**. A plasmon related hump near 570 nm may also be noted in **Figure 3.9 (c)**. We could not apply equation (1) for only NP cell without LH as the reflectance of that film is very less and the approximation holds true only in case of opaque films. These data and the foregoing discussion indicate that the presence of tiny gold nanoparticles in the TiO₂ matrix serve as additional light harvesting centers which can scatter/absorb the visible spectrum more efficiently. When light interacts with the Au NPs there is local enhancement in the electric field which enhances the absorption in the surrounding semiconductor.^[41] This concept is very well documented for various kinds of solar cells using metal nanostructures in the active layers of devices.^[42-43] Additionally for thin film solar cells, in order to enhance the light absorption with the same semiconductor thickness, use of metal nanoparticles on the rear side of the device has been suggested.^[44-45] We have basically followed the same strategy with the novelty that the Au NPs are matrix embedded forming distributed nanoscale Schottky junctions.

We also measured the transmittance of light through the different configurations (only TiO₂ NP cells, and TiO₂ NP cells with TiO₂ NF or Au: TiO₂ NF LH layers in an inverted geometry) and then calculated absorbance of light in the device interior using an equation [Absorbance (A) = 1-R-T]. **Figure 3.9 (d)** shows that the absorbance in the case of Au:TiO₂ NF cell is higher than that in the TiO₂ NF cell suggesting an effectively higher optical path length in the device interior. This confirms that Au:TiO₂ NF is better light harvesting agent as compared to TiO₂ NF. This can be attributed to the compounded effect of the nanoscale distributed Schottky barriers formed in harvesting region. These Schottky barriers act collectively as additional light harvesting centers.^[46] As the size of gold nanoparticles is about 5 nm, their Schottky interfaces with TiO₂ can render an antenna effect and lead to enhancement in the light trapping in the device interior.

The possible mechanism of enhanced light trapping can be described with reference to the schematic of **Figure 3.10**. Admittedly, this is speculative in the absence of a detailed simulation study which is out of scope of this work.

It may be remembered that when the light reaches the LH layer in an actual solar cell, it is randomized in terms of directions by scattering in the active layer. It can get back-scattered (dashed red arrows) due to a better light scattering ability of TiO₂ nanofibers as reported in previous works.^[9] This LH effect will be present also in the case of the cells with Au: TiO₂ NF LH layer (dashed red arrows). However an additional interesting effect can make a positive LH contribution in this case emanating from the absorption (and re-emission) of light by the surface plasmon-polariton modes at the nanoscale Au:TiO₂ interfaces. Indeed, when light interacts with the embedded tiny Au NPs it can generate surface plasmon-polariton modes (SPP modes) at the Schottky barriers and such modes can concentrate electromagnetic fields leading to trapping of the incident light effectively. These SPP modes redirect the incident solar radiations at 90° angles. Hence the radiations incident on the LH layer from the active layer travels back to the active layer. The nanofibers in the harvesting layer are randomly oriented hence the generated SPP modes will get

redirected in all directions. This random propagation of SPP modes leads to additive interference leading to higher energy dissipation in the active layer. These coupled SPP modes can travel about micron distances from their origin point. Hence the energy transfer to the dye molecules also enhances. In the case of only TiO₂ NF the enhancement in the dye absorption is only due to backscattered light. Although the light scatters back and enhances the absorption in the active layer, dye molecules can absorb only that part of the visible spectrum where the dye absorption is maximum. But in the case of Au loaded TiO₂ nanofibers these coupled SPP modes provide additional energy to enhance the light absorption even in the sub-wavelength region. Thus the use of gold loaded TiO₂ nanoparticles helps in enhanced light trapping in the active as well harvesting regions. Au/TiO₂ Schottky interface dispersion in Au:TiO₂ NF is random; hence the distribution of nanoscale interfaces in the microscopic fibers provides an additional benefit over the normal surface plasmon enhancement. The location of interfaces leads to coupling of the plasmon generated in LH layer. Additionally it helps in concentrating the light in the device interior. These SPP modes are thus mainly responsible for the observed enhancement in the photogenerated charges by dye molecules. Additionally these SPP modes also help enhance the transport rate of photogenerated charges in the device interior. Nailiang Yang et al have shown the use of ordered gold nanoparticle array as an effective counter electrode to achieve optical path enhancement along with the efficiency.^[8] However, the enhancement in efficiency was mainly attributed to better reflection and plasmonic effects.

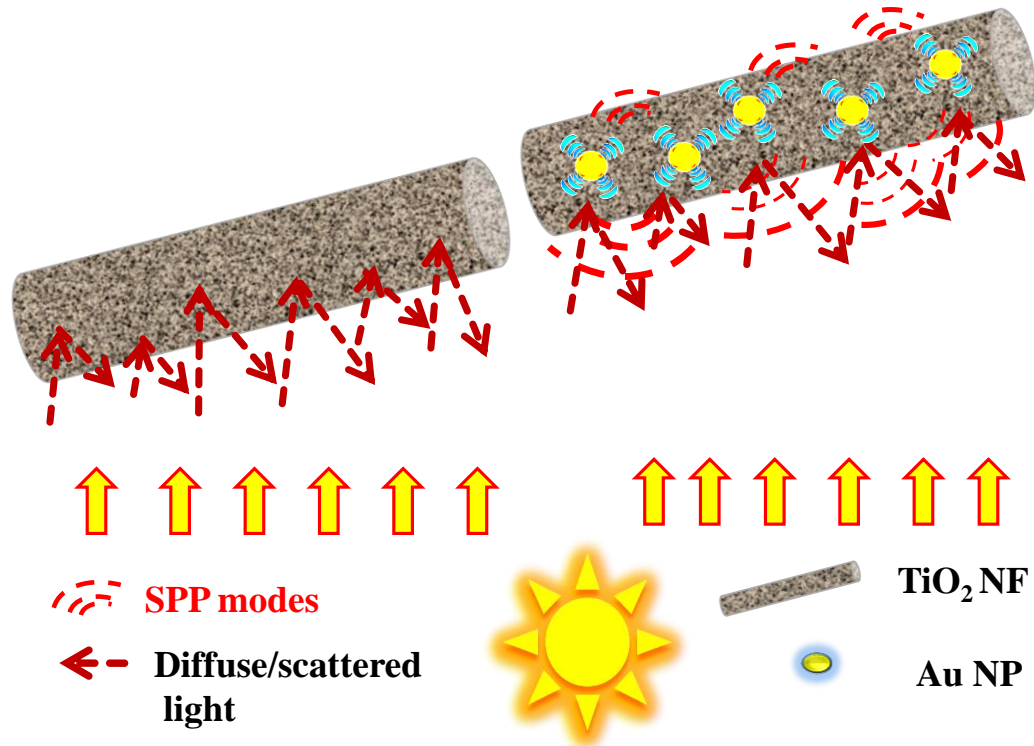


Figure 3.10 shows the Mechanism of Light harvesting in case of TiO₂ NF and TiO₂ Au NF respectively.

3.5 Conclusion

In this paper we have demonstrated a significant enhancement in the solar cells parameters with the use of Au NP loaded TiO₂ nanofibers in the light harvesting layer. The use of gold loaded fibers shows improvements mainly in the current density and the fill factor of the devices which is mainly attributed to the lower charge recombination. Additionally impedance analysis reveals an enhancement in the chemical capacitance by almost 75%. The higher capacitance is due to the enhanced charge trapping density of states in the conduction band as well as below the conduction band due to favorable band alignment of the Au/TiO₂ Schottky interfaces. These enhanced trapping states were also revealed by the photoluminescence study. We have also established that in case of Au: TiO₂ NF cell the optical path length in the device interior was higher than that of only TiO₂ NF based Cell. Coupled SPP modes generated at the randomly distributed

Au/TiO₂ interfaces in the LH layer are suggested to play a key role in these phenomena.

3.6 References

- [1] Barnes W.L., Dereux A., Ebbesen T.W. *Nature*. 2003, 424, 824-830.
- [2] H. A. Atwater, A. Polman. *Nat. Mater.*, 2010, 9, 205 - 213.
- [3] J.A. Schuller, E.S. Bernard, W. Cai, Y.C. Jun, J.S. White, M.K. Brongersma. *Nat. Mater.* 2010, 9, 193 - 204.
- [4] M. A. Green, S. Pillai. *Nature Photonics*. 2012, 6, 130 - 132.
- [5] M. D Brown, T. Suteewong, U. Weisner, H. Snaith. *Nano letters*. 2011, 11, 438 - 445.
- [6] S. Pillai, M.A. Green. *Solar Energy Materials & Solar cells*. 2010, 94, 1481 - 1486.
- [7] V.E. Ferry, L.A. Sweatlock, D. Pacifici, H.A. Atwater. *Nano Letters*, 2008, 8, 4391 - 4397.
- [8] N. Yang, Q. Yuan, D. Wang, L. Jiang. *ChemSusChem*, 2012, 5, 572 - 576.
- [9] L. Yang, W. Woon-Fong Leung. *Adv. Mater.*, 2011, 23, 4559 - 4562.
- [10] J. Du, J. Qi, D. Wang, Z. Tang. *Energy Environ Sci*, 2012, 5, 6914 - 6918.
- [11] Y. Li, H. Wang, G. Zhou, Z.S. Wang. *Energy Environ Sci*, 2013, 6, 2156 - 2165.
- [12] H.S. Kim, C.R. Lee, T. Moehl, S.J. Moon, J.E. Moser, M. Gratzel, N.G. Park. *Scientific Reports*, 2012, 2, 591, 1.
- [13] M.M. Lee, J. Teuscher, T. Miyasaka, T.N. Murakami, H.J. Snaith. *Science*, 2012, 10.1126, 1.
- [14] J. Burschka, N. Pellet, S.J. Moon, M.K. Nazeeruddin, M. Gratzel. *Nature*, 2013, 499, 316 - 319.
- [15] J. Qi, X. Dang, P. Hammond, A. Belcher. *ACS Nano*, 2011, 7108 - 7116.

- [16] N. C. Jeong, C. Prasittichai, J. T. Hupp. *Langmuir*, 2011, 27, 14609 - 14614.
- [17] V. E. Ferry, J. N. Munday, H. Atwater. *Adv. Mater.*, 2010, 22, 4794 - 4808.
- [18] C. Nahm, H. Choi, J. Kim, D. R. Jung, C. Kim. *Appl. Phys. Lett.*, 2011, 99, 253107.
- [19] S. Chang, Q. Li, X. Xiao, K. Y. Wong, T. Energy Environ Sci, 2012, 5, 9444 – 9448.
- [20] S. Muduli, K. Vijayamohanan, N.Valanoor, S. B.Ogale. *Solar Energy*, 2012, 86,1428 – 1434.
- [21] S.Chuangchote, T.Sagawa, S.Yoshikawa. *Applied Physics Letters*, 2008, 93, 033310.
- [22] P. Zhu, A.Sreekumar Nair, S. Yang, Seeram Ramakrishna. *J.Mater.Chem*, 2011, 21, 122210 - 122212.
- [23] S. Ito, T. N. Murakami, P. Comte, M.K.Nazeeruddin, M. Gratzel. *Thin Solid Films*, 2008, 516, 4613 - 4619.
- [24] S. Ito, P. Chen, P. Comte, M.K.Nazeerudding, P. Liska, M. Gratzel. *ProgPhotovolt : Res. Appl*, 2007, 15 (7), 603.
- [25] D. Li, Y. Xia. *Adv. Mater.*, 2004, 16 (14), 1151 - 1170.
- [26] N. Shibata, A. Goto, K.Matsunga, T. Mizoguchi, S.D.Findlay, T. Yamamoto, Y.Ikuhara. *Phys.Rev.Lett*, 2009, 102, 136105 - 136108.
- [27] Zhang W.F., Y.L.He, M.S.Zhang, Z.Yin, Q.Chen. *J. Phys D: Appl. Phys*, 2000, 33, 912 .
- [28] H. Li, Z. Bian, J. Zhu, Y. Huo, H, Li, Y. Lu. *J.Am.Chem. Soc*, 2007, 129, 4538 - 4539.
- [29] Kubelka P. *J.Opt Soc. Am*, 1948, 38, 448 - 448.
- [30] Y. Borensztein, L. Delannoy, A. Djedidi, R.G. Barrera, C. Louis. *J.Phys.Chem.C*, 2010.114, 9008.
- [31] Eric D. Smolensky, Michelle C. Neary, Yue Zhou, Thelma S. Berquoa and Valérie C. Pierre *Chem. Commun.*, 2011, 47, 2149–2151.

- [32] Susie Eustis and Mostafa A. El-Sayed. *Chem. Soc. Rev.*, 2006,35, 209–217
- [33] B. Liu, L. Wen, X. Zhao. *Materials Chemistry and Physics*, 2007, 106, 350 -353 .
- [34] M. Jakob, H. Levanon. *Nano Letters*, 2003, 3, 353 - 358.
- [35] B. E. Hardin, H. J Snaith, M. D. McGehee. *Nature Photonics*, 2012, 6, 162 - 169.
- [36] X. Yang,A. Wolcott, G. Wang, A. Sobo, R. Carl, J. Z. Zhang, Y. Li. *Nano Letters*, 2009, 2331 - 2336.
- [37] Q.Wang, S.Ito, M.Gratzel, F.Fabregat-Santiago, I.Mora-Sero, J.Bisquert, T.Bessho, H.Imai. *J.Phys.Chem.B*, 2006, 110, 25210 - 25221.
- [38] Bisquert J. *Physical Phys.Chem.Chem.Phys*, 2008, 10, 49 - 72.
- [39] Bisquert J. *Phys ChemChem Phys*, 200,3 5, 5360 - 5364.
- [40] K. Mukherjee, T. H. Teng, R. Jose, *App.Phys.Lett*, 2009, 95, 012101
- [41] Raether H. 1998 *Springer Tracts In Modern Phycis III*, Springer.
- [42] C. Hagglund, M.Zach, B. Kasem. *Appl.Phys.Lett*, 2008, 92, 013113.
- [43] T. Kume, S.Hayashi, H. Ohkuma, K.Yamamoto. *Jpn. J.Appl. Phys*, 1995, 34, 6448 - 6451.
- [44] F.J. Beck, A.Polman, K.R.Catchepol*J.Appl.Phys*, 2009, 105, 114310 - 114316.
- [45] F.J. Beck, S. Mokka pati, K.R.Cathpole. *Appl.Phys.Lett*, 2010, 96, 033113.
- [46] T. Wijensinghe, M. Premaratne. *Optics Express*, 2012, 20 (7), 7151.

Chapter 4

Hybrid perovskite quantum nanostructures synthesized by electrospray antisolvent-solvent extraction and intercalation.

Perovskites based on organometal lead halides have attracted great deal of scientific attention recently in the context of solar cells and optoelectronic devices due to their unique and tunable electronic and optical properties. Herein we show that the use of electrospray technique in conjunction with the antisolvent-solvent extraction leads to novel low-dimensional quantum structures (especially 2-D nanosheets) of $\text{CH}_3\text{NH}_3\text{PbI}_3$ - and $\text{CH}_3\text{NH}_3\text{PbBr}_3$ -based layered perovskites with unusual luminescence properties. We also show that the optical bandgaps and emission characteristics of these colloidal nanomaterials can be tuned over a broad range of visible spectral region by compositional tailoring of mixed-halide (I and Br based) perovskites.

*The content of this chapter has been published in “*ACS applied Materials and Interfaces*, 2016, 8(1), 854-861. Reproduced by permission of American Chemical Society

4.1. Introduction

Organometal-halide perovskites have been receiving significant attention recently due to their distinctive electronic and optical properties, which have led to record high power conversion efficiency (PCE) of >20% in solution-processed perovskite solar cells (PSCs).^[1-5] These properties include strong broad-band absorption, tunable optical properties, and the ambipolar nature of charge carriers with long lifetimes, which are under intense scientific investigations at this time. The 3-D perovskite structure, with a general formula ABX_3 , is versatile and allows substitutions of a variety of organic cations (A), divalent metal ions (B), and halogens (X), resulting in tunable changes in their optical and electronic properties. More recently researchers have been developing synthesis approaches to create a variety of nanostructures of organolead-halide hybrid perovskites to expand the property space and to achieve altogether new properties through quantum effects.^[6-7] These nanostructures possess high quantum yield and strong optically-tunable fluorescence with narrow emission bandwidths, making them suitable for diode and lasing applications.^[8] Some research groups have used antisolvent crystallization approach^[9-11] to obtain 0-D (quantum dots or QDs), 1-D (nanorods, nanobelts, nanowires), 2-D (nanosheets) of $CH_3NH_3PbX_3$ (MAPbX₃) based perovskites. This antisolvent crystallization approach has also been used to obtain films of 3D hybrid perovskite (without any organic moiety for intercalation) and shown to improve the photovoltaic performance of hybrid solar cells.^[12]

Recently, Zhou et. al.^[13] demonstrated a room-temperature antisolvent-solvent extraction (ASE) process for the synthesis of dense, ultra-smooth MAPbI₃ perovskite thin films. In that approach, the MAPbI₃ precursor solution in N-Methyl-2-Pyrrolidone (NMP) solvent was spin-coated on a substrate, and then the wet film was immediately dipped in a bath of a second solvent, diethyl ether (DEE), to facilitate rapid nucleation and growth of perovskite crystals. Planar PSCs fabricated from those films delivered up to 15% PCE.

In this work, we build upon this simple, scalable antisolvent-solvent extraction (ASE) approach for the synthesis of unusual, low-dimensional MAPbX₃-based perovskite colloidal nanostructures in a single step. This is accomplished by combining the ASE technique with the electro-spray process. Electro-spray is a versatile method for materials growth.^[14] in which fine liquid droplets are dispensed from a sharp tip onto a metal or a metal-supported substrate under an applied electric field between the tip and the substrate. In this method no polymers (or macromolecules) are used; instead only fine liquid droplets are dispensed.

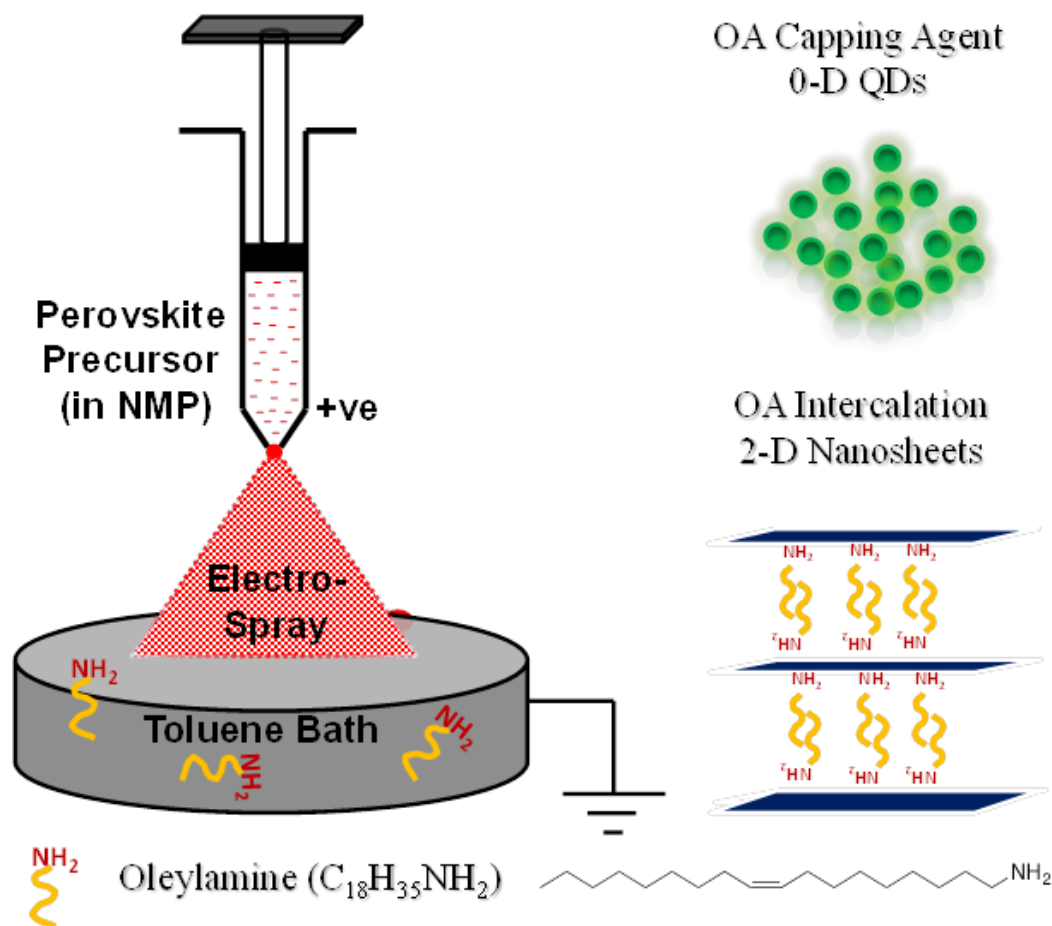


Figure 4.1. Schematic illustration of the synthesis of MAPbX₃ perovskite quantum structures by electro-spray antisolvent-solvent extraction (ASE) route.

In the present work, we use a novel variant of the commonly used electrospinning or electrospray method, where instead of a solid substrate a bath of the antisolvent (without and with a capping agent) in a metal-electrode container is used as the substrate. A schematic illustration of this process is shown in **Figure 4.1**. In this process, under the high electric field the surface tension of a droplet breaks it into a jet of nano-droplets of the precursor solution which fall into antisolvent (toluene) bath, resulting in rapid crystallization of the perovskite leading to uncapped 0-D nanoparticles. In related experiments, we have also used oleylamine (OA) as a capping agent in the toluene bath to arrest the nanoparticle growth. OA ($C_{18}H_{35}NH_2$) is a long-chain neutral alkyl molecule with amine ($-NH_2$) functionality, which not only serves as a capping agent but, more interestingly, also contributes to the formation of 2-D sheet-like quantum structures of layered perovskites by intercalation via host-guest chemistry. This leads to anisotropic quantum confinement of excitons which influences their luminescence properties.

Recently, it has been shown that mixed-halide-based perovskites hold great promise for applications in the area of laser diodes and light emitting diodes (LEDs).^[15] The mixed-halide perovskite compositions offer advantages of bandgap tuning over a wide visible spectrum.^[16] Thus, we have also synthesized mixed-halide perovskite ($MAPbI_{(3-x)}Br_x$) nanostructures using this method by simply mixing the $MAPbI_3$ and $MAPbBr_3$ precursor solutions in different proportions. We show that the optical bandgaps and photoluminescence (PL) of these colloidal solutions can be tuned over a wide wavelength range of 500 nm to 700 nm.

4.2. Experimental Section

4.2.1. Materials.:

All chemicals and solvents were used as-received without further purification, which included: PbI_2 (lead iodide 99% pure Alfa Aesar), PbBr_2 (lead bromide. 99% pure, Alfa Aesar), hydroiodic acid (HI; 57 wt.% in water, Sigma Aldrich), hydrobromic acid (HBr; 48 wt.% in water, Sigma Aldrich), methylamine (CH_3NH_2 ; 33 wt.% solution in absolute ethanol, Sigma Aldrich), oleylamine (OA; Sigma Aldrich), N-methyl-2-pyrrolidone (NMP; Analytical Grade Chem Labs), and toluene (Analytical Grade Chem Labs).

4.2.2. Synthesis of MAPbX_3 Nanomaterials:

For MAPbI_3 , 1 mM of PbI_2 and 1 mM of MAI were dissolved in 2 ml of NMP for about 6 h. After ensuring the homogeneity of the solution, it was fed into the 1 ml DISPO VAN syringe (26 gauge). This solution was dispensed at a flow rate of 0.6 ml/h under a very high electric field of 1.8 kV/cm. The distance between the needle and collector was kept at 10 cm. The jet of droplets thus formed was directed into an antisolvent bath of liquid held in a metal container used as the ground terminal. This bath contained either toluene or toluene with the OA capping agent dissolved in it. The MAPbBr_3 -based nanostructures were also fabricated using the same strategy with 1 mM of PbBr_2 and 1 mM of MABr as the precursors. The amount of OA in toluene was varied systematically to prepare MAPbI_3 QDs. For the synthesis of mixed-halide-based layered perovskites separate precursor solutions of MAPbI_3 and MAPbBr_3 were mixed in 1:3, 1:1, and 3:1 ratios. The experimental conditions for these electrospaying experiments were the same as above. In additional experiments, the MAPbI_3 precursor was directly electrospayed into 100 mL of toluene bath without OA for about 20 min, followed by the quick addition of 100 μL of OA to the toluene bath.

4.3 General Characterization:

X-ray diffraction (XRD) patterns were recorded using a powder diffractometer (Xpert 1712, PANalytical) using monochromatic Cu K α X-ray radiation ($\lambda=1.5402$ Å). An ultraviolet-visible (UV-vis) spectrophotometer (LAMBDA 950, Perkin Elmer) was used to collect the absorption spectra. PL spectra (Fluoromax 4C, Horiba) and PL life-time (FLS980, Edinburgh Instruments) measurements were also performed on the nanostructures produced. Surface properties of the nanostructures were characterized using X-ray photoelectron spectroscopy (XPS; Phi 5000 versa Probe 2, Physical Electronics, ULVAC PHI) equipped with a monochromatic Al K α ($\lambda=1486.6$ eV) x-ray radiation and a hemispherical analyzer. Here the specimens were prepared in a glove box and hermetically sealed. Just before the XPS characterization, the specimens were opened and immediately loaded into the XPS chamber to avoid any ambient degradation. For recording the XRD and XPS data the specimens were prepared by drop-casting the colloidal dispersion in toluene on a Si wafer and drying. In the case of transmission electron microscopy (TEM) characterization (300 T-30 Tecnai, FEI Corp.), the colloidal dispersion in toluene was drop-cast on carbon-coated TEM copper grids and dried.

4.4 Result and discussion:

4.4.1 MAPbI₃ and MAPbBr₃ 3-D Perovskites Grown without Oleylamine:

Initially, the MAPbI₃ precursor solution was electrosprayed directly into the toluene bath which contained no capping agent. This resulted in the formation of nanoparticles of average size 50 ± 15 nm [Figures 4.2(a) and 4.2(d)]. The indexed XRD pattern in Figure 4.2(b) confirms the tetragonal phase of MAPbI₃ (space group I4/mcm). The UV-vis spectrum in Figure 4.2(c) shows a broad absorption feature over the entire visible range. Similarly, the PL spectrum shows broad fluorescence centered at ~ 760 nm. This is blue-shifted by ~ 20 nm as compared to the bulk perovskite case.¹⁷ In the case of MAPbBr₃ [Figure 2(d) and 2(e)] the nanoparticles (~ 50 nm) are of cubic phase (space group Pm3m), with a narrower PL peak centered around 550 nm. It has been

reported that long alkyl-chain-based ammonium salts can be used to create different types of perovskite nanostructures.^[9] Here we have used OA as a neutral ligand^[18] in the antisolvent toluene bath to serve a dual purpose, namely capping agent and intercalation agent, for the spray of the perovskite precursors falling into the bath. Note that other long alkyl-chain-based ammonium salts such as, n-octylammonium bromide and n-butylammonium bromide salts,^[19,20,21] can also be used in this method.

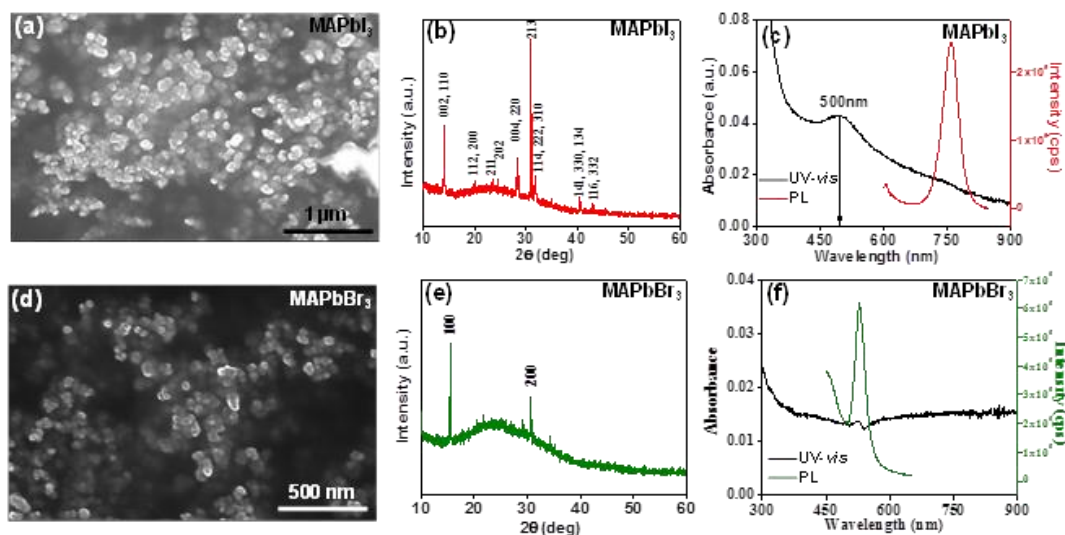


Figure 4.2 SEM images of the nanoparticles: (a) MAPbI₃ and (d) MAPbBr₃. Indexed XRD patterns of the nanoparticles: (b) MAPbI₃ and (e) MAPbBr₃. UV-vis and PL spectra (excitation wavelength 510 nm for MAPbI₃ and 400nm for MAPbBr₃) of the nanoparticles: (c) MAPbI₃ and (f) MAPbBr₃.

Initially, experiments were performed using OA quantity varying over the range of 50-100 μl in 100 ml toluene bath to determine the effect of OA concentration on the nature of quantum structures formed. **Figure 4.3** shows the FE-SEM images for three such cases. With 50 μl of OA we observed the assembly of nanoparticles, along with sheet-like structures. As the amount of OA was increased to 80 μl, the sheet-like structures were found to increase. However, some nanoparticles-assembly was still seen to be present in that sample. For the case of 100 μl OA only sheet-like structures were observed. We also measured

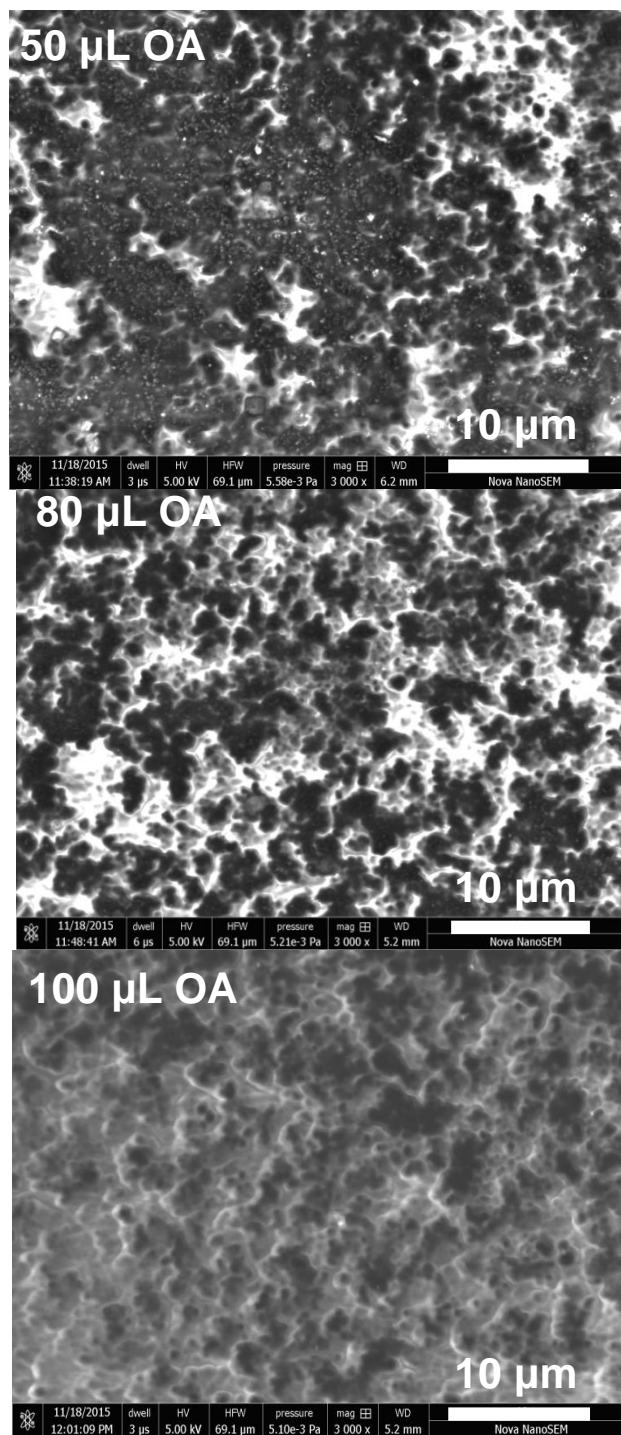


Figure 4.3 shows FE-SEM images for change in morphology of MAPbI₃ based layered perovskite w.r.t. change in concentration of OA.

Photoluminescence (PL) spectra of the colloidal solutions obtained for the cases of different OA concentrations. A strong blue shift in the PL-peak maximum,

with additional shoulder between 700 nm and 730 nm is observed for 50 μl and 80 μl OA amounts. Zhang et al.¹⁰ have reported similar PL peak at 734 nm for MAPbI₃ quantum dots. However, the shoulder disappears as the amount of OA is increased to 100 μl in the toluene bath, with the PL-peak maximum occurring at 630 nm as shown in **figure 4.4**. This large blue-shift of ~ 130 nm suggests that the OA is not only acting as a capping agent but it also plays a role in modifying the perovskite crystal structure itself. Thus, all further experiments used 100 μl of OA in 100 ml of toluene bath.

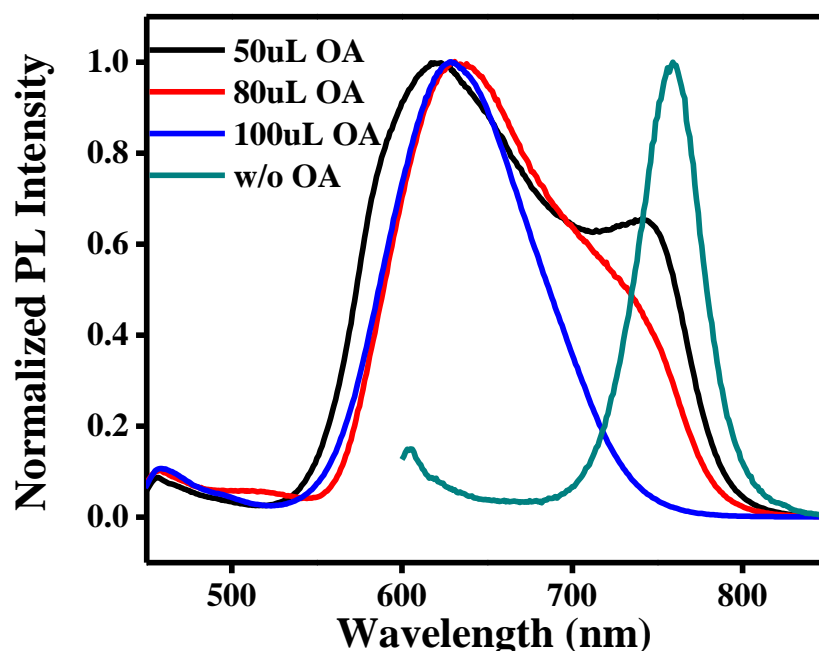


Figure 4.4 shows the photoluminescence spectra of MAPbI₃ based perovskite colloidal solutions obtained with variation in concentration of oleylamine in toluene bath.

4.4.2 MAPbI₃-Based Layered 2-D Perovskites Grown with Oleylamine:

The TEM image in **Figure 4.5(a)** shows nanosheet-like 2-D layered perovskite. The areal sizes of these nanosheets are quite large, in the micron range. Additionally, the ‘spot’ selected-area electron diffraction pattern (SAEDP) in **Figure 4.5(a)** inset confirms the single-crystal nature of the 2-D perovskite

nanosheets. The structure of this 2-D perovskite comprises ordered hexagonal arrangement of PbI_2 octahedrons in a sheet, with these sheets stacked together through the organic ligand.^[22,23] As mentioned earlier, when the MAPbI_3 precursor solution falls into toluene bath it crystallizes immediately leading to the perovskite formation. The presence of OA in the same bath can act as a guest molecule, and it can intercalate between the thin layers of PbI_2 . This OA intercalation results in distortion of PbI_6^{4-} octahedra, and hence the as-formed perovskite is stabilized in the 2D perovskite structure.

The OA intercalation can be further confirmed by the XRD results in **figure 4.5(b)** where high intensity peaks at very low values of $2\theta=5.8^\circ$ and $2\theta=9.6^\circ$ are observed. This implies high inter-planar spacing, corresponding to $00l$ and $00(2l)$ reflections, respectively, where $l = 2, 4, 6, \dots$, for layered perovskite with monoclinic symmetry.^[24] The interlayer spacings (d_{00l}) for $2\theta=5.8^\circ$ and ($d_{00(2l)}$) for $2\theta=9.6^\circ$ are 15.22 Å and 9.21 Å, respectively. The crystal orientation of this 2-D perovskite suggests periodic arrangement of inorganic layers comprised of PbI_2 sheets formed by series of PbI_6^{4-} based octahedra and OA-based organic ligands intercalated in between, oriented along the c-axis. In addition to sharp peaks at low 2θ , a hump at 2θ in the range 20° - 30° is also observed, which can be attributed to broadened (002) reflections from the PbI_2 nanosheets. Thus, the TEM and XRD results confirm the formation of highly-oriented single-crystalline intercalated layered 2-D perovskite along with the formation of PbI_2 nanosheets comprising PbI_6^{4-} octahedrons. Note that Mitzi and co-workers^[25] had shown occurrence of a series of such Sn-based layered 2-D perovskite phases at low temperatures.

The UV-vis data in **figure 4.5(c)** shows strong absorption edge at $\lambda = 428$ nm, which has a large blue-shift as compared with bulk MAPbI_3 .^[26] In addition, a broad absorption peak around ~ 365 nm is observed in the UV region, which also confirms the presence of nanosized PbI_2 quantum dots.^[27] It has been reported that since the inorganic framework is separated by organic molecule intercalation in layered 2-D perovskites, such systems show high oscillator

strength at room temperature due to large dielectric mismatch, resulting in naturally formed quantum well structures with stable exciton binding energies.^[28] From Tauc plot [**Figure 4.5(d)**] the band gap of this layered perovskite was found to be 2.8 eV, which is much higher than that of the bulk MAPbI₃ perovskite (1.55 eV). This significant increase in the band gap can be attributed to strong anisotropic quantum confinement effects arising from the naturally formed quantum well structures. The PL spectrum in **figure 4.5(c)** also shows a broad emission centered at ~630 nm with a full-width half-maximum (FWHM) of ~102 nm, in addition to a very large Stokes shift.

Recently Wu et al.^[29] have hypothesized that the formation of “self-trapped exciton” is facilitated by going from 3-D perovskite to 2-D perovskites, and the corresponding density increases. Self-trapped exciton can be ascribed to the formation of excited state as a result of the highly covalent nature of lead-iodide backbone. Ahmad et al.^[30] have also discussed the formation of self-trapped exciton in the case of lead-halide-based layered structures formed by using long alkyl-chained amines as intercalating agents. Another cause for large Stokes shift may be stacking of a few 2-D sheets leading to the formation of stable low energy band states contributing to the exciton emission.^[29] A large Stokes shift is also reported very recently in the case of hybrid-perovskite QDs.^[10]

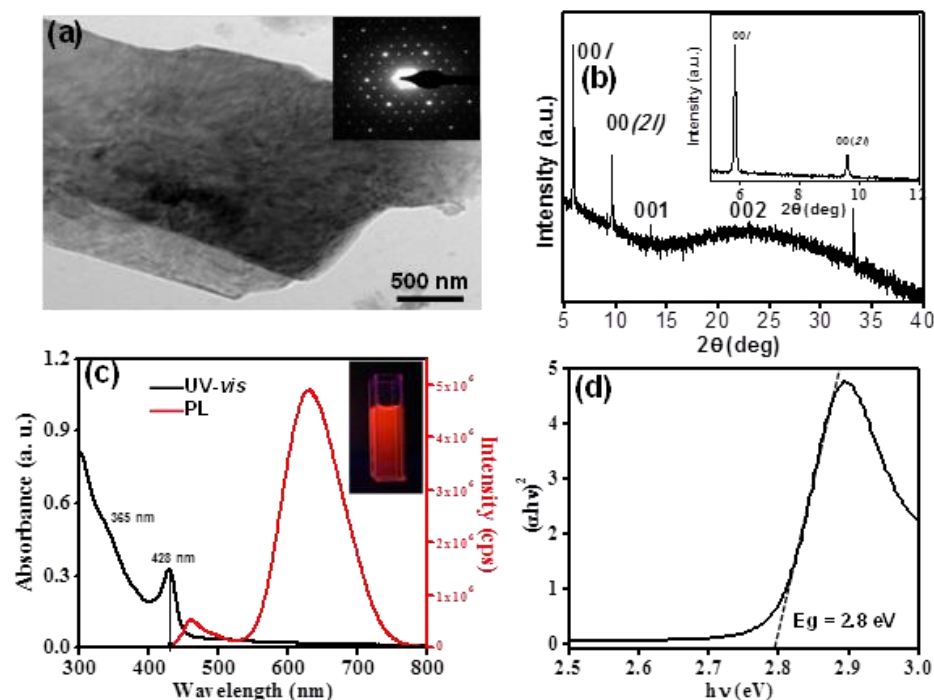


Figure 4.5. MAPbI₃-based layered 2-D perovskite nanostructures: (a) TEM image, (b) XRD pattern, (c) UV-vis and PL spectra (excitation wavelength 365 nm) (inset: photograph of the colloid), and (d) Tauc plot obtained from the UV-vis data.

Further we performed the AFM analysis to quantify the minimum thickness of 2-D sheets when the corresponding dilute solution is drop casted onto a silicon wafer surface. As may be seen from **figure 4.6** the minimum thickness is about 3-4 nm. At some places, the sheets have clearly stacked up enhancing the height, as expected. The lateral width of the thinnest sheets is of the order of 400-500 nm.

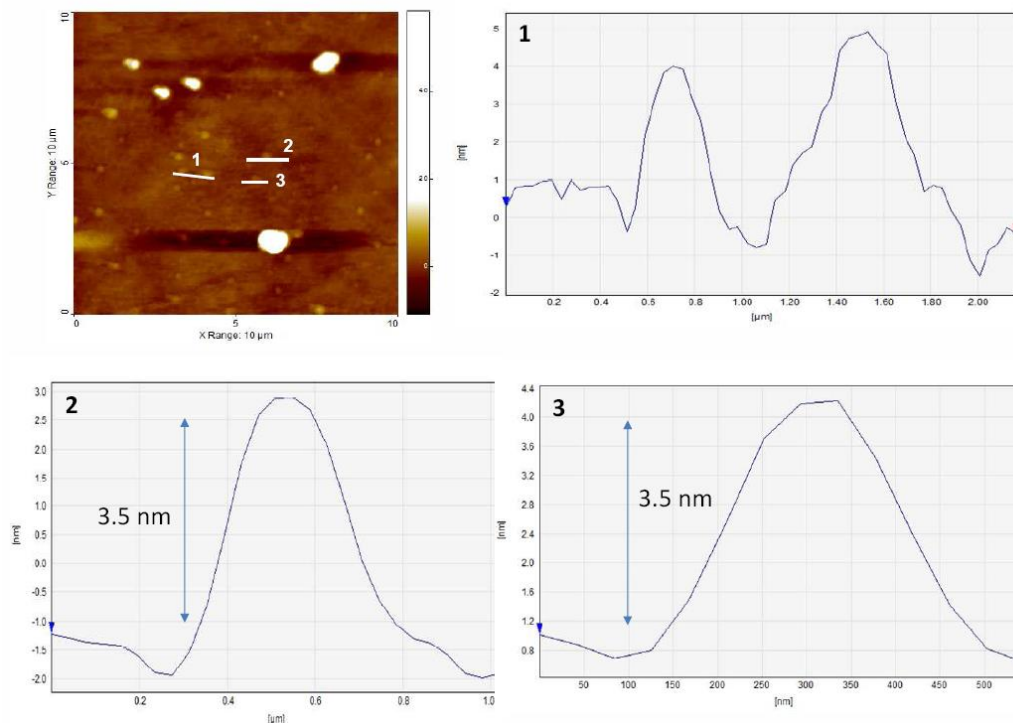


Figure 4.6 shows the AFM image and height profile data for MAPbI₃ based layered perovskite.

Because crystallization of the perovskite phase and intercalation of OA in-between the PbI₂ layers are kinetically competing processes in the bath, to gain deeper insight into the OA intercalation process, OA was added to the anti-solvent bath after perovskite crystallization. The UV-vis spectrum for those samples shown in **figure 4.7** reveals multiple absorptions at 365 nm, 510 nm, and 571 nm. The peaks at 510 nm and 571 nm are due to the 3-D MAPbI₃ perovskite, and the peak at 365 nm is due to nanosized PbI₂ particles. These results suggest that the OA addition after electro spray affects the as-formed perovskite nanoparticles by decomposing them into PbI₂ QD, and that only the presence of OA in the toluene bath during electro spray results in its intercalation leading to formation of layered 2-D perovskite.

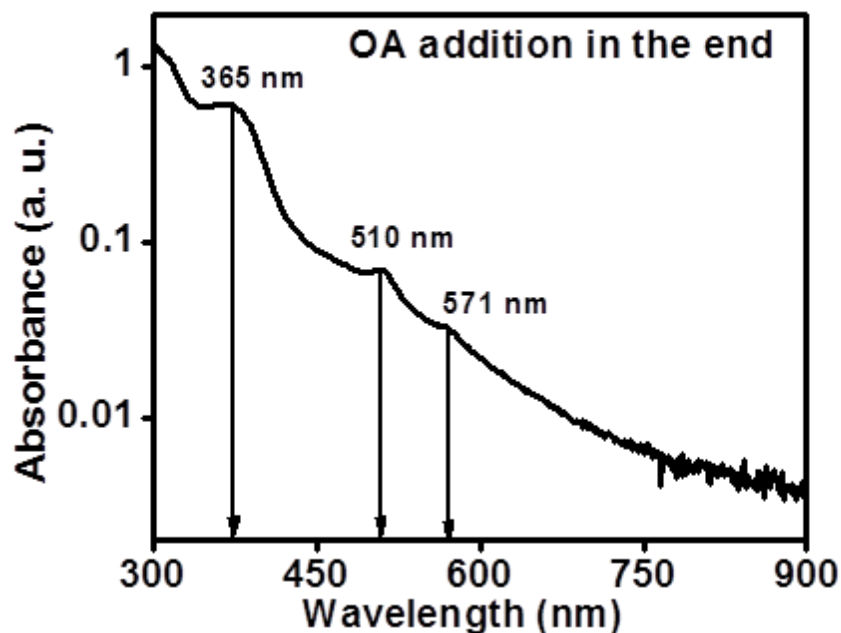


Figure 4.7 UV-vis spectrum of MAPbI₃-based nanostructures formed in Toluene bath where the OA is added after the crystallization is complete.

The PL decay dynamics for the case of MAPbI₃-based layered 2-D perovskite is shown in **figure 4.8**. The PL decay was fitted with bi-exponential decay resulting in lifetimes of $\tau_1=20$ ns (35.5%) and $\tau_2=74$ ns (64.5%). Such bi-exponential decay confirms the presence of two different species involved in the recombination process. The relatively long lifetimes confirm the presence of surface trap states produced by the isolated PbI₂-based octahedra.^[31] Such defect centers are mainly responsible for the large Stokes shift and the longer lifetime decays.

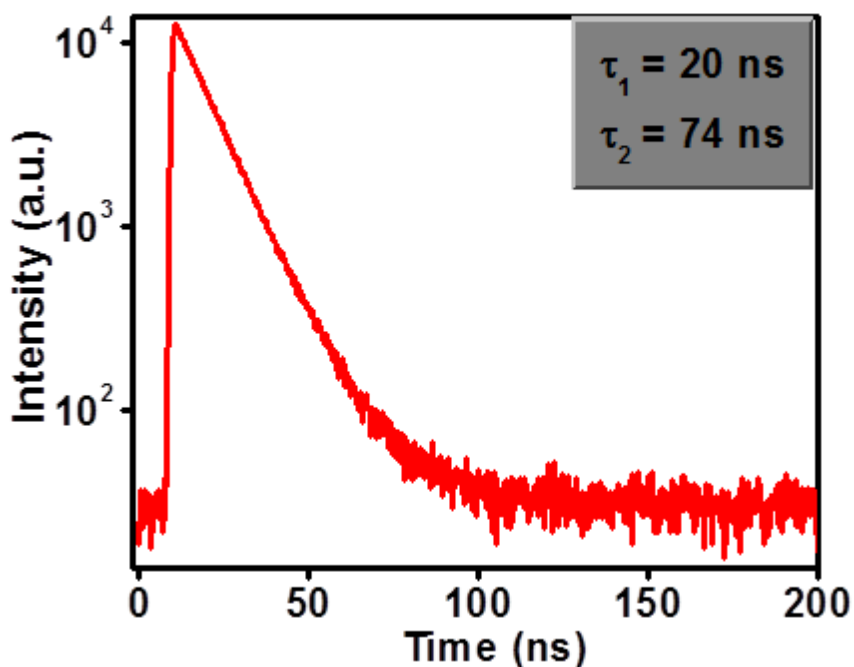


Figure 4.8 PL (excitation wavelength 400 nm) lifetime decay for MAPbI₃-based layered 2-D perovskite nanostructures (bi-exponential fit).

4.4.3 MAPbBr₃-Based Layered 2-D Perovskites Grown with Oleylamine:

The TEM images in **figures 4.9(a) and 4.9(b)** show the presence of 2-D nanosheets and 0-D QDs, respectively, of the MAPbBr₃-based perovskite. The size of the monodispersed quantum dots [**Figure 4.9 (b)**] is ~2-3 nm. The XRD pattern in **figure 4.9(c)** shows the corresponding peak broadening, and sharp peaks at small 2θ (5° - 10°) similar to what is observed in **figure 4.5(b)**. The PL spectrum in **figure 4.9(d)** shows a single emission centered at ~520 nm.

The strong quantum confinement effect is primarily responsible for the observed blue-shift vis-a-vis the bulk 3-D perovskite.^[32] This sharp PL emission is mainly an excitonic emission with a narrow line width of ~25 nm. It should be noted that the Pb-I bond is more polar than the Pb-Br bond, hence the precursor droplets falling in the bath are stabilized more rapidly in the Pb-Br case leading to higher density of capped QDs.^[33] Thus, in the bromine-based

perovskite case, the role of OA as capping agent is more effective in stabilizing the 0-D QD, although some 2-D sheets are also seen due to its role as the intercalating organic moiety. The Tauc plot in **figure 4.9(e)** shows two distinctive band gaps of $E_g=2.2$ eV for QDs and $E_g=2.9$ eV for the layered 2-D perovskite.

The PL decay dynamics for MAPbBr₃-based colloidal solution was also studied for recombination lifetimes [**Figure 4.9(d)**]. The PL decay is fitted using a tri-exponential function, with lifetimes $\tau_1=5.7$ ns (40.4%), $\tau_2=16.2$ ns (41.5%), and long-lived carriers with $\tau_3=125$ ns (18.1%). The relative contribution of long-lived carriers is significantly less as compared to the earlier reported work.^[10]

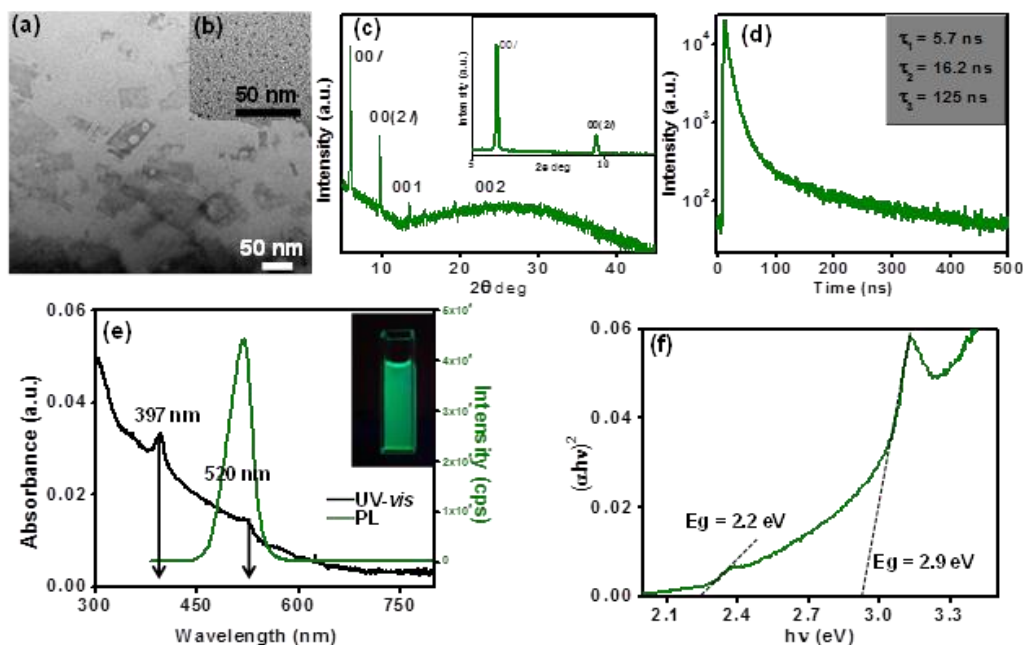


Figure 4.9. MAPbBr₃-based layered 2-D perovskite nanostructures: (a) and (b) TEM images, (c) XRD pattern, (d) PL lifetime decay (tri-exponential fit), (e) UV-vis and PL spectra (excitation wavelength 365 nm) (inset: photograph of the colloid), and (f) Tauc plot obtained from the UV-vis data.

4.4.4 MAPbI_(3-x)Br_x Mixed-Halide Layered 2-D Perovskites Grown with Oleylamine:

The TEM image of mixed-halide MAPbI_{1.5}Br_{1.5}-based layered 2-D perovskite in **figure 4.10(a)** shows a nanosheet (wrinkled), and the ‘spot’ SAEDP (inset) confirms its single-crystal nature. **figure 4.10(b)** shows the XRD pattern of this mixed-halide material, along with the XRD patterns from MAPbI₃ [**Figure 4.5(b)**] and MAPbBr₃ [**Figure 4.9(c)**]. This inset in **figure 4.10(b)** shows that the maximum in the broad hump for MAPbI_{1.5}Br_{1.5} is in-between those for MAPbI₃ and MAPbBr₃, as expected. It is reported that for mixed-halide based layered 2-D perovskite structures, Br⁻ preferentially occupies the apical positions in the Pb-X octahedra.^[28] Since the ionic radius of Br⁻ is smaller than the I⁻,^[34] overall structure of MAPbI_{1.5}Br_{1.5} is dominated by the Br-based layered 2-D perovskite. Also, this results in the smaller $d_{(00l)}$ and $d_{[00(2l)]}$ interlayer spacing of 14.8 Å and 9 Å, respectively, in MAPbI_{1.5}Br_{1.5} based nanostructures compared to those in MAPbI₃ based nanostructures. **Figure 4.10(c)** shows the normalized absorbance spectra for mixed-halide layered 2-D perovskites: MAPbI₃, MAPbI_{2.25}Br_{0.75}, MAPbI_{1.5}Br_{1.5}, MAPbI_{0.75}Br_{2.25}, and MAPbBr₃. Sharp excitonic features corresponding to single absorption peak are seen in each case, and the photographs of the colloids (inset) show the corresponding colors. The normalized PL peaks [**Figure 4.10(d)**] are systematically blue-shifted with increasing Br content. Additionally, the PL linewidth is also seen to decrease considerably from full width at half maximum (FWHM) from 102 nm down to 30 nm with increasing Br content. In the case of MAPbBr₃ perovskites the emission characteristics are mainly excitonic in nature, while in the case of MAPbI₃ perovskites they are mainly observed due to “self-trapped excitonic” character which results in the PL-peak broadening. Thus, in the mixed-halide-based perovskites, the increasing substitution of I- by Br- progressively reduces the self-trapping effect. Since the electronegativity of Br- is higher than that of I-, in the mixed halide cases the Br atom substitution in

lead iodide crystal framework affects the overall band structure allowing the effective band gap tuning over the broad visible range.

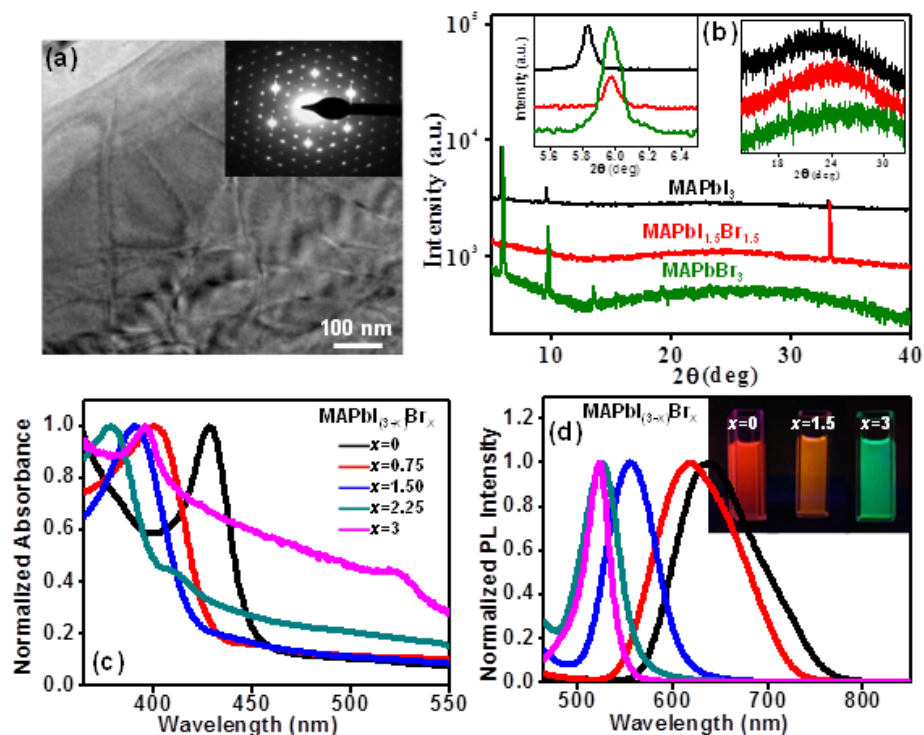


Figure 4.10. Mixed-halide MAPbI_{1.5}Br_{1.5}-based layered 2-D perovskite: (a) TEM image (inset: SAEDP) and (b) XRD pattern. Layered 2-D perovskites: MAPbI₃, MAPbI_{2.25}Br_{0.75}, MAPbI_{1.5}Br_{1.5}, MAPbI_{0.75}Br_{2.25}, and MAPbBr₃ (c) normalized UV-vis spectra (inset: photographs of the colloids of indicated compositions), and (d) normalized PL spectra (excitation wavelength 365 nm).

4.4.5 X-ray photoelectron spectroscopy (XPS) Studies:

The XPS data in **figures 4.11(a)-4.11(d)** provide further insights into the structural aspects of these as-formed hybrid nanomaterials. In the XPS data in **figure 4.11(a)** for the three compositions, MAPbI₃, MAPbI_{1.5}Br_{1.5}, and MAPbBr₃, two symmetric peaks of Pb 4f_{7/2} and Pb 4f_{5/2} are observed at binding energy (B.E.) values of 138.2 and 143.0 eV, respectively. The energy difference

due to spin-orbit splitting of 4f orbital is 4.8 eV, which is in agreement with the literature values.^[35] No sign of metallic Pb was observed in these three compositions. The XPS data in **figure 4.11(b)** show two peaks corresponding to I 3d_{5/2} and I 3d_{3/2} at B. E. values of 618.4 eV and 629.9 eV, respectively, with the spin-orbit splitting energy of 10.5 eV. The peak positions for MAPbI₃ and MAPbI_{1.5}Br_{1.5} are almost overlapping. The N_{1s} XPS data for all the three compositions are plotted in **figure 4.11(c)**. For MAPbI₃, the N_{1s} data can be fitted to two peaks at 399.3 eV and 401.1 eV. The peak at 399.3 eV can be attributed to the presence of free amine (-NH₂) group of OA capping the 0-D QDs, while the peak at 401.1 eV can be attributed to NH₃⁺ in MAI,^[36] confirming the two types of nitrogen attached to the lead-halide framework. The NH₃⁺ occupies the corner positions of perovskite unit cells and -NH₂ group intercalates and separates the inorganic lead iodide sheets. However, in the case of MAPbI_{1.5}Br_{1.5}, and MAPbBr₃ three peaks can be deconvoluted at 399.3 eV, 400.4 eV, and 401.3 eV as shown in **figure 4.11(c)**. Since Br-containing perovskite crystallizes into 2-D nanosheets as well, the additional 400.4 eV B.E. peak can be attributed to the -NH₂ group of the intercalated OA. In the MAPbBr₃ XPS data in **figure 4.11(d)** the B.E. peak positions for Br 3d_{5/2} and Br 3d_{3/2} are at 68.0 and 69.0 eV, respectively, which are at somewhat higher B.E. compared to MAPbI_{1.5}Br_{1.5}. This can be attributed to the changes caused to the electron density distribution in the bond by the more electronegative Br.

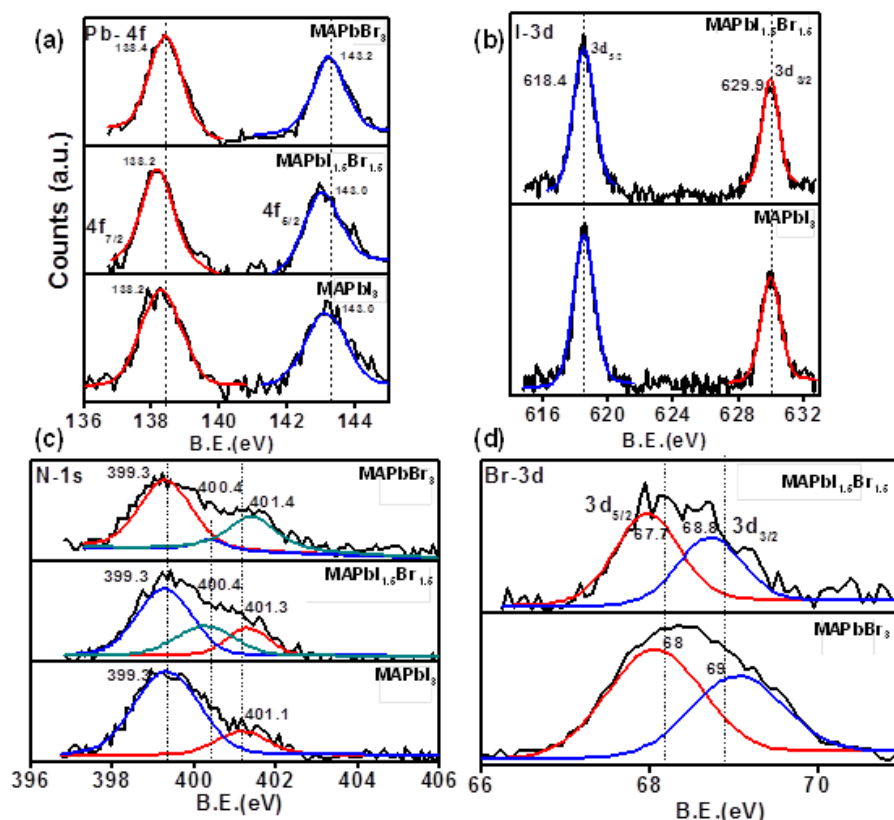


Figure 4.11. XPS data: (a) Pb-4f (MAPbI₃, MAPbI_{1.5}Br_{1.5}, MAPbBr₃), (b) I-3d (MAPbI₃, MAPbI_{1.5}Br_{1.5}), (c) N-1S (MAPbI₃, MAPbI_{1.5}Br_{1.5}, MAPbBr₃), and (d) Br-3d (MAPbBr₃, MAPbI_{1.5}Br_{1.5}).

4.5 Conclusion

We have demonstrated the use of modified electrospray-assisted antisolvent-solvent extraction protocol for the synthesis of 0-D QDs and 2-D nanosheets of I and Br based as well as mixed halide hybrid perovskite systems. The 0-D QDs result via oleylamine (OA) capping, while the 2D nanosheets are realized via OA intercalation. The MAPbI₃ and MAPbBr₃ 0-D QDs show interesting optical properties, whereas the mixed-halide 2-D layered perovskite nanostructures show unusual luminescence properties. The optical band gaps and emission characteristics of these colloidal mixed-halide nanomaterials can be tuned over a broad range of visible spectral region via compositional tailoring.

4.6 References

- 1) Green, M. A.; Ho-Baillie, A.; Snaith, H. *Nat. Photonics* 2014, 8, 506-514.
- 2) Park, N.G. *J.Phys.Chem.Lett.* 2013, 4, 2423-2429.
- 3) Kojima, A.; Teshima, K.; Shirai, Y.; Miyasaka, T.; *J. Am. Chem. Soc.* 2009, 131, 6050-6051.
- 4) Stranks, S.D.; Eperon, G.; Grancini, G.; Menelaou, C.; Alcocer M.J.P.; Leijtens, T.; Herz, L.M.; Petrozza, A.; Snaith, H.J. *Science* 2013, 342, 341-344.
- 5) Xing, G.; Mathews, N.; Sun, S.; Lim, S.S.; Lam, Y.M.; Grätzel, M.; Mhaisalkar, S.; Sum, T. C. *Science* 2013, 342, 344-347.
- 6) Fu, Y.; Meng, F.; Rowley, M. B.; Thompson, B. J.; Shearer, M. J.; Ma, D.; Hamers, R. J; Wright, J.C.; Jin, S. *J. Am. Chem. Soc.* 2015, 137, 5810-5818.
- 7) Di, D.; Musselman, K.P.; Li, G.; Sadhanala, A.; Ievskaya, Y.; Song, Q.; Tan, Z.K.; Lai, M.L. MacManus-Driscoll, J. L.; Greenham, N.C.; Friend, R.H. *J. Phys. Chem. Lett.* 2015, 6, 446-450.
- 8) Zhu, H.; Fu, Y.; Meng, F.; Wu, X.; Gong, Z.; Ding, Q.; Gustafsson, M.V.; Trinh, M.T.; Jin, S.; Zhu, X.Y. *Nat. Mater.* 2015, 14, 636-642.
- 9) Schmidt, L.C.; Pertegás, A.; Carrero, S. G.; Malinkiewicz, O.; Agouram, S.; Espallargas, G. M.; Bolink, H. J.; Galian, R.E.; Prieto, J. P. *Nontemplate J. Am. Chem. Soc.* 2014, 136, 850-853.
- 10) Zhang, F.; Zhong, H.; Chen, C.; Wu, X.G.; Hu, X.; Huang, H.; Han, J.; Zou, B.; Dong, Y.; *ACS Nano* 2015, 9, 4533-4542.
- 11) Kollek, T.; Gruber, D.; Gehring, J.; Zimmermann, E.; Schmidt-Mende, L.; Polarz, S. *Angew. Chem. Intl. Ed.* 2015, 54, 1341-1346.
- 12) Jeon, N. J.; Noh, J. H.; Kim, Y. C.; Yang, W. S.; Ryu, S.; Seok, S. *Nat. Mater.* 2014, 13, 897-903.

- 13) Zhou, Y.; Yang, M.; Wu, W.; Vasiliev, A. L.; Zhu, K.; Padture, N. P. *J. Mater. Chem. A.* 2015, 3, 8178-8184.
- 14) Kumar, P. S.; Sundaramurthy, J.; Sundarrajan, S.; Babu, V. J.; Singh, G.; Allakhverdiev, S. I.; Ramakrishna, S. *Energy Environ. Sci.* 2014, 7, 3192-3222.
- 15) Kumawat, N.; Dey, A.; Narasimhan, K.L.; Kabra, D. *ACS Photon.* 2015, 2, 349-354.
- 16) Eperon, G. E.; Stranks, S.D.; Menelaou, C.; Johnston, M. B.; Herz, L.M.; Snaith, H. J. *Energy Environ. Sci.* 2014, 7, 982-988.
- 17) Burschka, J.; Pellet, N.; Moon, S.J.; Baker, R.H.; Gao, P.; Nazeeruddin, M.K.; Graetzel, M. *Nature* 2013, 499, 316-319.
- 18) Mourdikoudis, S.; Liz-Marzán, L.M. *Chem. Mater.* 2013, 25, 1465-1476.
- 19) Tyagi, P.; Averson, S.M.; Tisdale, W.A. *J. Phys. Chem. Lett.* 2015, 6, 1911-1916.
- 20) Sichert, J.A.; Tong, Y.; Mutz, N.; Vollmer, M.; Fishcer, M.; Milowska, K.Z.; Cortdella, R.G.; Nickel, B.; Cardenas-Daw, C.; Stolarczyk, J.K.; Urban, A.S.; Feldmann, J. *Nano Lett.* 2015, 15, 6521-6527.
- 21) Dou, L.; Wong, A.B.; Yu, Y.; Lai, M.; Kornienko, N.; Eaton, S.W.; Fu, A.; Bischak, C.G.; Ma, J.; Ding, T.; Ginsberg, N.S.; Wang Wang, L.; Alvisatos, A.; Yang, P. *Science* 2015, 349, 1518-1521.
- 22) Cheng, Z.; Lin, J.; *Cryst. Eng. Comm.* 2010, 12, 2646-2662.
- 23) Zheng, Z.; Liu, A.; Wang, S.; Wang, Y.; Li, Z.; Lau, W. M.; Zhang, L. *J. Mater. Chem.* 2005, 15, 4555-4559.
- 24) Venkataraman, N. V.; Bhagyalakshmi, S.; Vasudevan, S.; Seshadri, R. *Phys. Chem. Chem. Phys.* 2002, 4, 4533-4538.
- 25) Mitzi, D. B.; Feild, C. A.; Harrison, W. T. A.; Guloy, A. M. *Nature* 1994, 369, 467-469.

- 26) Navas, J.; Coronilla, A. S.; Gallardo, J. J.; Hernandez, N. C.; Calleja, J. M.; *Nanoscale* 2015, 7, 6216-6229.
- 27) Papagiannouli, I.; Maratou, E.; Koutselas, I.; Couris, S. J. *Phys. Chem. C.* 2014, 118, 2766-2775.
- 28) Ahmad, S.; Prakash, G.V. *Opt. Mater. Express* 2014, 4, 101-110.
- 29) Wu, X.; Trinh, M.T.; Zhu, X.Y. *J. Phys. Chem. C.* 2015, 119, 14714-14721.
- 30) Ahmad, S.; Baumberg, J.; Prakash, G.V. *J. Appl. Phys.* 2013, 114, 233511-233513.
- 31) Caramona, C. R.; Gratia, P.; Zimmermann, I.; Grancini, G.; Gao, P.; Grätzel, M.; Nazeeruddin, M. K. *Energy Environ. Sci.* 2015, 8, 3550-3556.
- 32) Takeoka, Y.; Fukasawa, M.; Matsui, T.; Kikuchi, K.; Rikukawa, M.; Sanui, K. *Chem. Comm.* 2005, 378-380.
- 33) Tanaka, K.; Takahashi, T.; Ban, T.; Kondo, T.; Uchida, K.; Miura, N.; *Solid State Comm.* 2003, 127, 619-623.
- 34) Aharon, S.; Cohen, B.E.; Etgar, L. *J. Phys. Chem. C.* 2014, 118, 17160-17165.
- 35) Morgan, W. E.; Van Wazer, J. R. *J. Phys. Chem.* 1973, 77, 964-969.
- 36) Chen, S.; Goh, T. W.; Sabba, D.; Chua, J.; Mathews, N.; Huan, C. H. A.; Sum, T. C. *APL Mater.* 2014, 2, 081512-081517.

Chapter 5

Hybrid perovskite films with highly enhanced optical and electrical properties by addition of quaternary alkyl ammonium salt.

In this work, we report significant enhancement in the luminescence and electrical properties of MAPbBr₃ thin films prepared via simple single step spin coating process by a novel additive mediated solvent extraction route. This process also improves the electronic properties due to less disordered structure formation which was confirmed through Photo thermal deflection spectroscopy. Herein we have used quaternary alkyl ammonium halide based salt as additive which was dissolved in chloroform as an anti-solvent. The salt treated films possess less electronic disorder which was measured in terms of Urbach energy. The Urbach energy was reduced from 38meV to 18meV. This decrement suggests that these films are far superior for optoelectronic applications as compared to the untreated samples. Indeed, the Photoluminescence (PL) quantum yield for these films was enhanced from 1% (w/o additive treatment) to 30% (w additive treatment). Further the light emitting diode was fabricated which showed 0.3% external quantum efficiency at 11V. Our device showed around 5V turn on voltage.

5.1. Introduction

Solution processible hybrid organic inorganic perovskites have shown promising outcomes in the field of optoelectronics and photovoltaics towards the end of the last decade.^[1-5] Now the solar cells efficiencies have reached up to 22% which holds great promise for future photovoltaic technology advancement.^[6] The intrinsic properties of these semiconductors possess high photoluminescence quantum yield, easy band gap tailoring, low lasing thresholds^[7-8] which make them more suitable for light emitting diodes (LEDs) and lasing applications.^[9-10] Methyl ammonium lead bromide (MAPbBr₃) based perovskite has shown remarkable success in LED applications as emission layer.^[11-15] This material possesses high exciton binding energy (90-170 meV) and it has greater air stability as well.^[16-17]

These semiconductors can be easily solution processed and hence spin coating is widely accepted method for perovskite thin film preparation. There are various other routes which have also been explored in terms of making uniform and smooth perovskite films.^[18-23] Recently Himchancho et al. has mentioned that the film fabrication goal for perovskite based light emitting diodes is completely different from the perovskite based solar cells. In solar cells, faster exciton dissociation and diffusion are required hence uniform films with larger grain size are essential. However for LED applications, uniform smooth films with lower exciton diffusion length (LD) are needed. Many attempts have been reported such as solvent engineering, supramolecular passivation, vapour assisted crystal growth for preparation of uniform and smooth perovskite films with good optoelectronic properties.^[24-26]

In this work we demonstrate a novel additive mediated solvent engineering approach to form highly luminescent perovskite films with significantly less electronic disorder. We apply Tetrabutylammonium bromide (TBAB) solution in chloroform as anti-solvent on to the perovskite film while spin coating. Such treated films exhibits smooth uniform film nature with smaller grain size and

additionally possess very high photoluminescence quantum yield (PLQE about 30%). These films were characterized using X-ray diffraction (XRD), UV-Visible spectroscopy (UV-Vis), time resolved photoluminescence (TRPL) and photo thermal deflection spectroscopy (PDS) techniques. Furthermore this TBAB treated perovskite layer was employed as emission layer in perovskite based LEDs which has shown promising results.

5.2. Experimental Section

5.2.1. MAPbBr₃ film formation:

MAPbBr₃ perovskite precursor solution was prepared by dissolving lead acetate (PbAc₂) and methyl ammonium bromide (MABr) in 1:3 molar ratio in DMF to get 40wt% solution. 0.1M Tetrabutylammonium bromide (TBAB) solution was prepared by dissolving 161.2mg of TBAB in 5mL of chloroform. Perovskite solution was spin coated on glass at 200 rpm for 60 seconds. For TBAB treated films, during spin coating after 10 seconds 100μL of TBAB solution was dripped onto the rotating film surface. Further the films were annealed at 100⁰C for 5 minutes, washed with chloroform and dried at room temperature. We have also made control films under the same conditions without additive treatment. These films are called as ‘w/o additive’ while TBAB treated films are called as ‘w additive’.

5.2.2. Light emitting diode (LED) device fabrication:

Patterned ITO glass was washed by sonicating in Acetone and isopropanol sequentially for 15 minutes. Oxygen plasma treatment was given for about 1 minute to cleaned substrate. 50nm PEDOT-PSS compact layer was deposited by spin coating aqueous PEDOT-PSS solution at 5000 rpm for 30 seconds. Further films were annealed at 100⁰C for 30 minutes. A very thin layer of Al₂O₃ was deposited by spin coating ethanolic solution of Al₂O₃. Further the films were annealed at 100⁰C for 15 minutes. Later TBAB treated perovskite films were deposited as mentioned in the film fabrication protocol [Process B]. A 50 nm electron injection layer comprised of 2:1 blend of 2,2',2''-(1,3,5-Benzinetriyl)-

tris(1-phenyl-1-H-benzimidazole) (TPBi) and poly{[N,N'-bis(2-octyldodecyl)-naphthalene-1,4,5,8-bis(dicarboximide)-2,6-diyl]-alt-5,5'-(2,2'-bithiophene)}(N2200) was then deposited. Later LiF/Al (2-3nm/100nm) electrodes were thermally evaporated as top electrode.

5.3 General Characterization:

The morphology of MAPbBr₃ films was studied by the scanning electron microscope (FE-SEM, Nova Nano SEM 450). The XRD pattern was recorded using Xpert 1712 PANanalytical diffractometer with source radiation of Cu K_α ($\lambda = 1.542 \text{ \AA}$). The absorption data for MAPbBr₃ films was recorded using Perkin Elmer Lambda 950 spectrometer. The blank quartz plate was used as reference. PDS measurements were carried out on the MAPbBr₃ films. The details of PDS set up and measurements, and calculation for Urbach energy are given in Sadhanala et al. ^[27]. The Photoluminescence (PL) and time resolved PL measurements were carried out on FLS980, Edinbrough instruments. The PLQE was measured directly using integrated sphere accessory.

5.4 Results and discussion:

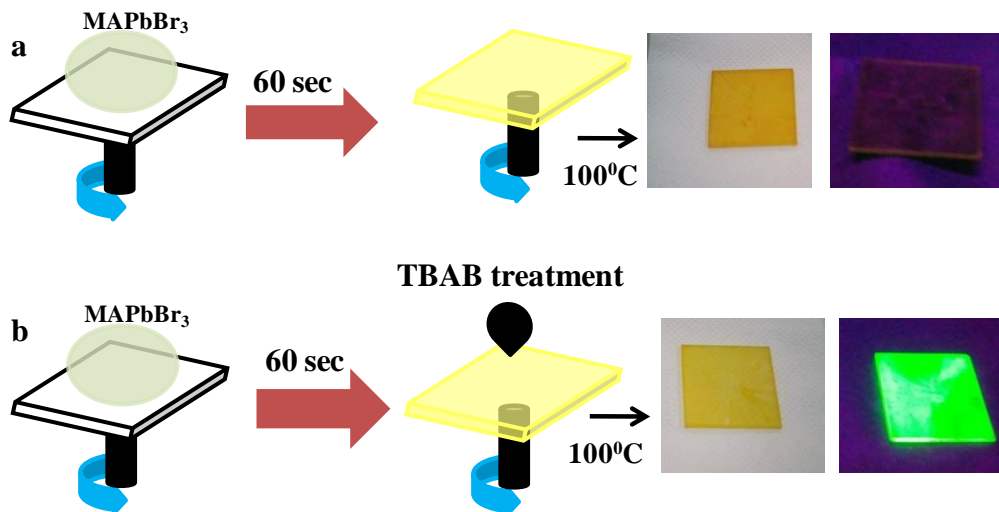


Figure 1 shows the schematic diagram of perovskite thin film formation with additive mediated solvent extraction process.

Figure 1 shows the schematic of the additive mediated solvent engineering approach process. Process (A) shows the conventional perovskite film formation route while process (B) depicts our modified method. Here we have used 0.1M TBAB solution which was dispensed during the spin coating on to the perovskite film. This addition was carried out after 10 seconds of initiation. The concentration of perovskite precursor solution is mentioned in the experimental section. This precursor solution gives faster perovskite crystal growth with uniform pin hole free films. This process also takes very short annealing time. For comparative study we have annealed both the films at 100⁰C for 5 minutes after spin coating. The films prepared with the process (A) show uniform film with no luminescence under UV-lamp ($\lambda_{exc} = 365 \text{ nm}$) whereas the films with process (B) gives very bright green luminescence. During spin coating, in the initial stage the solvent evaporation starts and the overall composition gets concentrated. The sudden dripping of anti-solvent helps in quick removal of DMF leading to homogenous film formation. In addition, we have employed TBAB which is quaternary ammonium salt as an additive. TBAB is used as phase transfer catalyst and as capping agent in the synthesis of gold nanoparticles. ^[28-29] In our case, TBAB helps in passivation of the perovskite surface. Details of this luminescence origin are discussed later.

In order to understand the role of TBAB treatment on the crystal size and film morphology we performed FE-SEM analysis of these films. Figure 2(a) shows the FE-SEM image of MAPbBr₃ perovskite film obtained through process (A). This film shows the full coverage without pin holes. Figure 2(b) shows the high resolution image of Figure 2(a) in which the crystalline grains are of the order of a few hundreds of nanometers. Whereas the films obtained via process (B) shows a uniform coverage but with a very small crystalline size. Figure 2(c) shows the full coverage with rough surface of perovskite film. The TBAB treatment has clearly affected overall crystal growth during perovskite film formation and a dense film consisting nanocrystals of MAPbBr₃ perovskite is obtained.

Figure 2(d) shows the high resolution image of Figure 2(b) which confirms that the TBAB treated film is composed of tiny crystals of MAPbBr₃ in the range of 50-70 nm.

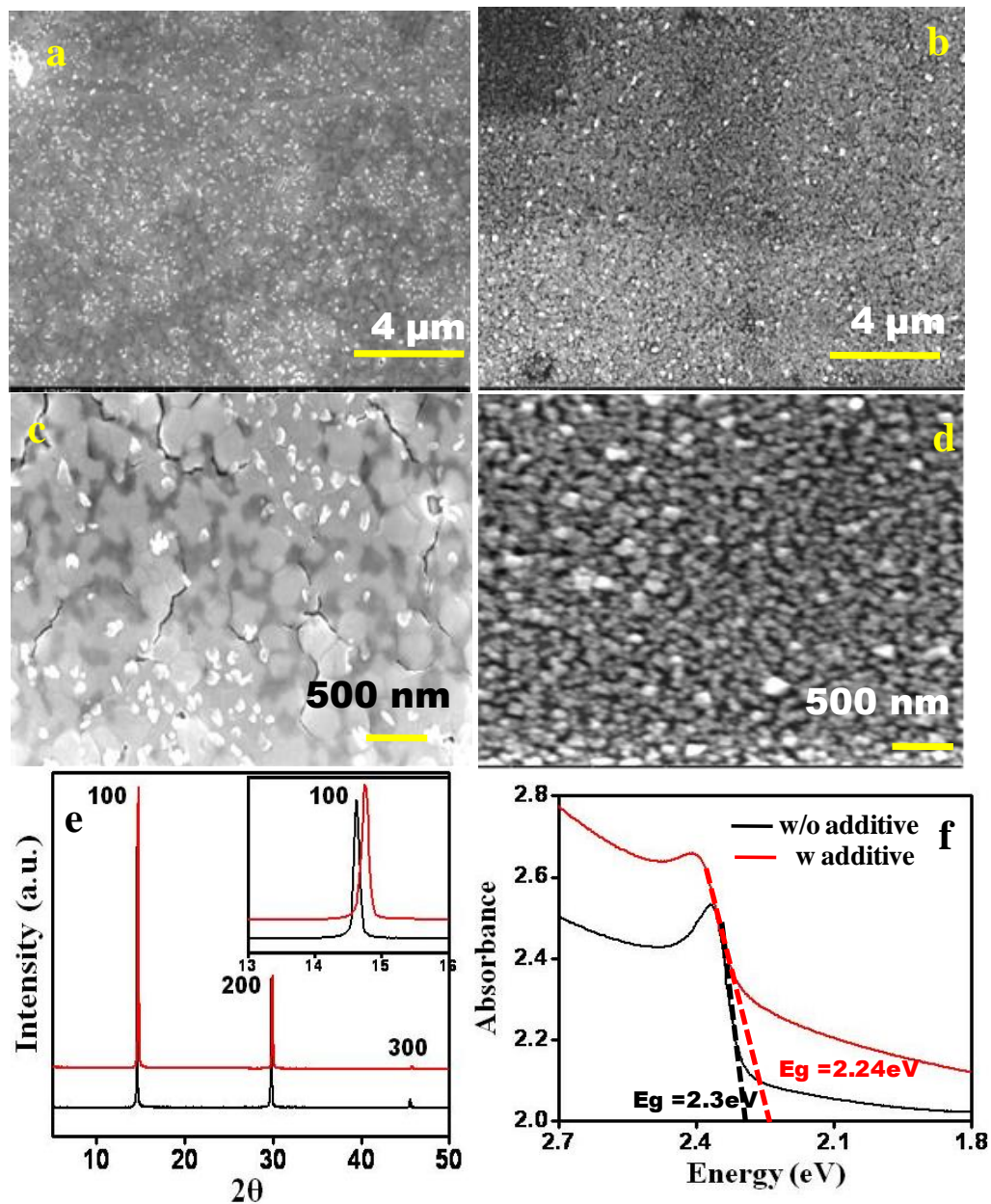


Figure 2 shows the FE-SEM images for MAPbBr₃ thin films. (a and c) shows the films obtained with process (A) and (b and d) shows the films obtained with process (B). Figure 2(e) shows the X-ray diffraction pattern and figure 2(f) shows the UV-Vis absorption spectrum for MAPbBr₃ films with process (A) and (B).

Thus the TBAB solution dripping arrests the overall crystal growth of MAPbBr₃ while film formation. The tiny crystals with the surface passivation by TBAB mainly contribute towards the major enhancement of the photoluminescence of MAPbBr₃ film.

In Figure 2(e) we show the XRD pattern for MAPbBr₃ films with and without TBAB treatment. It shows the formation of cubic phase MAPbBr₃ with space group Pm3m.^[21] The XRD pattern reflects the peaks at $2\theta = 15^\circ$, 30° and 46° which can be assigned to (100), (200) and (300) planes MAPbBr₃ films. The inset of figure 2(e) shows the shift in (100) reflection towards higher 2θ values suggesting the decrease in lattice parameter of TBAB treated films as compared to the conventionally processed ones. Additive treatment in our case results in rapid nucleation of perovskite crystals in the presence of TBAB. The as formed perovskite has a charged surface and hence the halide ions on the surface of perovskite crystals have charge imbalance. The Tetrabutylammonium ion is a quaternary cation which can bind to the uncompensated halide ions on the surface of perovskite crystals. Such binding can cause a strain gradient in the crystal structure of MAPbBr₃ with decrement in the lattice parameter. In our case we believe that this shift in the peak position mainly arises due to such binding.

Figure 2(f) shows the UV-Vis data for the MAPbBr₃ films. The absorption spectrum shows the overall enhancement in the absorption for TBAB treated film as compared to the conventionally processed film. The absorption spectrum shows sub-band gap absorption tail and strong exciton peak. For TBAB treated samples the exciton peak is broadened as compared to the conventional film. It has been reported that such broadening can be attributed to structural disorder in the system and not the compositional disorder. In our case, TBAB treated film is composed of tiny MAPbBr₃ nanocrystals. Such crystals can contribute in enhanced light scattering effects as compared to the conventional film. Similarly the positive slope of band edge is enhanced in the case of TBAB treated

samples. N. Kumawat et al. have shown that in the case of MAPbBr₃ films, the overall absorption enhancement near the band gap region is mainly due to the excitonic absorption.^[30]

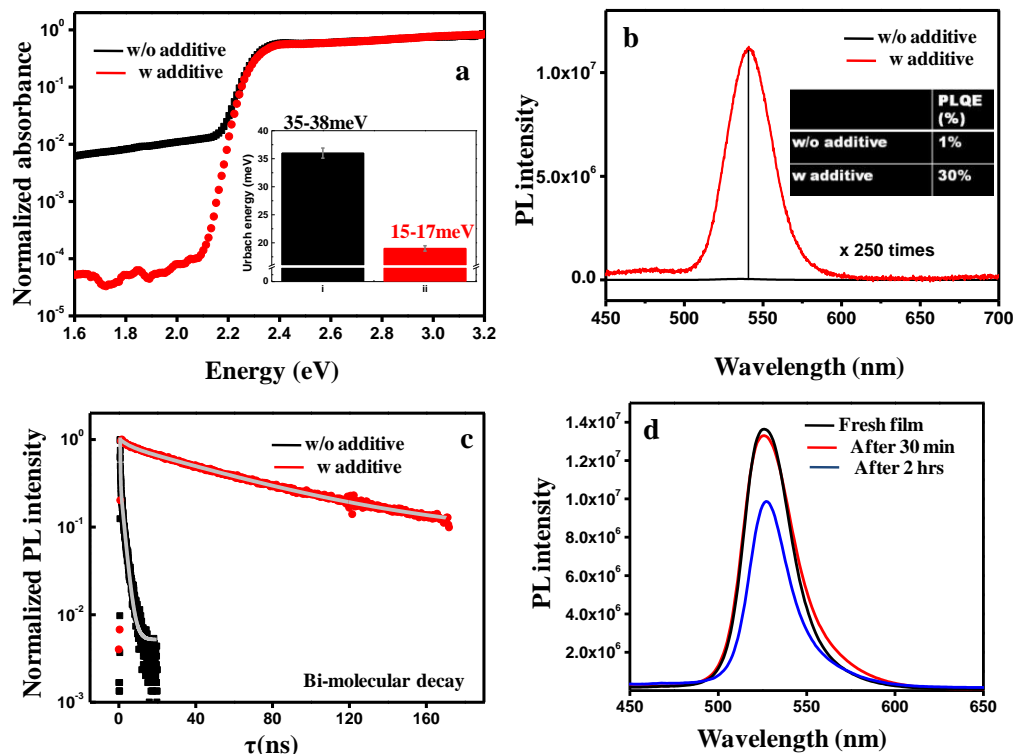


Figure 3(a) shows the PDS spectra; (b) shows the Photoluminescence spectra for thin films of MAPbBr₃ obtained through Process (A and B). Figure 3(c) shows the time resolved photoluminescence spectra for MAPbBr₃ films. Figure 3(d) shows the PL stability for MAPbBr₃ thin film obtained through process (B) at 100⁰C for 30 mins (red) and 2 hrs (blue) annealing time.

To understand the effect of TBAB treatment in detail we performed PDS measurements on our samples. PDS is a very sensitive absorption technique to measure the absorption near the band edge and the measurements is less affected by light scattering effects.^[8] The PDS spectra for MAPbBr₃ films with and without additive treatment are shown in Figure 3(a). The absorption of TBAB treated perovskite film is enhanced by two orders of magnitude as

compared to the one without TBAB treatment. Moreover, the band edge for TBAB treated film is sharp indicating that the sub-band gap defect density is reduced significantly. This suggests that upon TBAB treatment the electronic disorder in this semiconductor film is dramatically decreased. Based on these data we have further calculated Urbach energy by considering the slope of Urbach tail. The estimate of Urbach energy mainly gives a quantitative measure of the electronic disorder in a semiconductor.^[31] In our case the Urbach energy for w/o additive treated film is about 35-38meV whereas for TBAB treated sample it is just 15-17meV. This substantial reduction in Urbach energy confirms the less electronic disorder in the TBAB treated MAPbBr₃ semiconductor film.

Figure 3(b) shows Photoluminescence spectra of MAPbBr₃ films. Upon TBAB treatment the PL intensity of the film is enhanced dramatically by a factor of 250. The inset of figure 3(b) shows the PLQE measured for these films using integrated sphere assembly. The PLQE of w/o additive treated film is about 1% which has been significantly enhanced to 30% upon TBAB addition. Such enhancement in the PLQE can be attributed to the lowering of nonradiative recombination pathways inside the MAPbBr₃ films. TBAB used in this work binds strongly to the surface of perovskite crystals to stabilize the uncoordinated halide ions.

Time resolved PL intensity decay for MAPbBr₃ films was also measured to further study radiative recombination in this system. TBAB treated film shows a higher PL life time as compared with untreated film. The PL life time curves were fitted by a bi-molecular exponential decay scheme. Upon TBAB treatment the PL life time is enhanced from 20 ns to 160 ns indicating that non-radiative recombination was suppressed in TBAB treated MAPbBr₃ films due to the less defect density which is also consistent with previous discussion.

In order to study the effect of temperature on the luminescence properties of TBAB treated MAPbBr₃ films, we annealed these films at 100⁰C for prolonged

time. The data were recorded immediately after taking out the films from hot plate. Figure 3(d) shows the stability of PL intensity data recorded after different time intervals. Even after annealing film for 30 mins at 100°C the PL intensity remains the same. The PL intensity drops to 75% of initial after annealing this film for about 2 hrs. This result suggests that TBAB treated perovskite films possess higher PLQE even after long time annealing treatment.

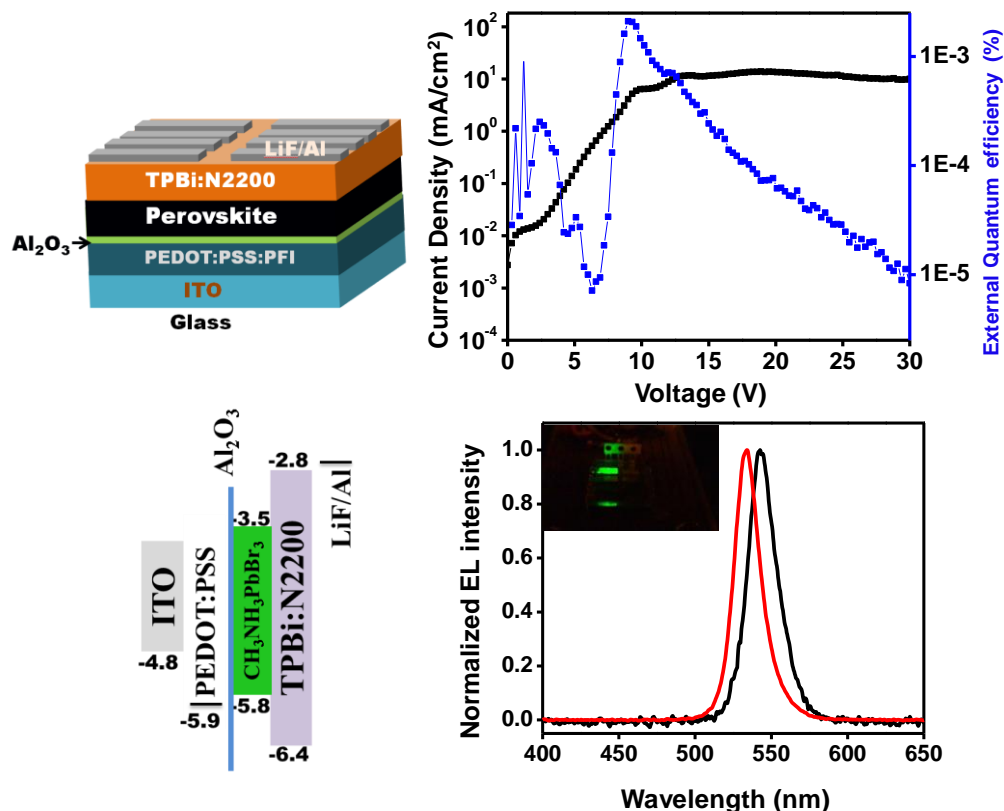


Figure 4(a) shows the schematic of LED device (b) shows the graph of current density and external quantum efficiency curves at room temperature. Figure 4(c) shows the band alignment schematic for LED device. Figure 4(d) shows the normalized EL intensity as a function of wavelength.

We have further demonstrated the potential of such treatment in the real device application. We have fabricated perovskite based light emitting diodes using TBAB treated MAPbBr₃ films. The device was fabricated by depositing 50nm PEDOT:PSS on to the ITO coated glass substrate, then 1nm of Al₂O₃ was

deposited on top of PEDOT:PSS followed by the TBAB treated perovskite. A 50nm electron injection layer comprised of 2:1 blend of 2,2',2''-(1,3,5-Benzinetriyl)-tris(1-phenyl-1-H-benzimidazole) (TPBi) and poly{[N,N'-bis(2-octyldodecyl)-naphthalene-1,4,5,8-bis(dicarboximide)-2,6-diy]-alt-5,5'-(2,2'-bithiophene)}(N2200) was then deposited followed by LiF/Al (1nm/100nm).

We measured electroluminescence spectra (EL) for such TBAB treated perovskite based devices. We obtained external quantum efficiency (EQE) of 0.3% at 11V. Our LED device showed turn on voltage is around 5V. The LEDs based on our material show promising results with low turn on voltage and narrow emission widths.

5.5 Conclusion

In conclusion, we report a novel and easily scalable additive mediated solvent extraction process for the fabrication of highly luminescent and electronic disorder free MAPbBr₃ based perovskite thin films. Our method shows the enhancement in the luminescence of perovskite thin films by factor of 250. Similarly the PLQE values are enhanced from 1% (for untreated samples) to 30% (treated samples). Later these highly luminescent perovskite films are used to demonstrate the LED application. Our LED devices showed 0.3% external quantum efficiency at 11V, and a turn on voltage of 5V.

5.6 References

- 1) Lee, Michael M., Joël Teuscher, Tsutomu Miyasaka, Takuro N. Murakami, and Henry J. Snaith. *Science* 338, **2012**, 643-647.
- 2) Burschka, Julian, Norman Pellet, Soo-Jin Moon, Robin Humphry-Baker, Peng Gao, Mohammad K. Nazeeruddin, and Michael Grätzel. *Nature* 499, **2013**, 316-319.
- 3) Nie, Wanyi, Hsinhan Tsai, Reza Asadpour, Jean-Christophe Blancon, Amanda J. Neukirch, Gautam Gupta, Jared J. Crochet, Manish Chhowalla,

Sergei Tretiak, Muhammad A Alam, Hsing-Lin Wang, Aditya Mohite. *Science* 347, **2015**, 522-525.

4) Stranks, Samuel D., and Henry J. Snaith. *Nature nanotechnology*, 10, **2015**, 391-402.

5) Zhang, Wei, Miguel Anaya, Gabriel Lozano, Mauricio E. Calvo, Michael B. Johnston, Hernán Míguez, and Henry J. Snaith. *Nano letters*, 15,**2015**, 1698-1702.

6) NREL chart, www.nrel.gov/ncpv/images/efficiency_chart.jpg

7) Deschler, Felix, Michael Price, Sandeep Pathak, Lina E. Klintberg, David-Dominik Jarausch, Ruben Higler, Sven Hüttner, Tomas Leijtens, Samuel D. Stranks, Henry J. Snaith, Mete Atatüre, Richard T. Phillips, and Richard H. Friend. *The journal of physical chemistry letters*, 5, **2014**, 1421-1426.

8) Sadhanala, Aditya, Shahab Ahmad, Baodan Zhao, Nadja Giesbrecht, Phoebe M. Pearce, Felix Deschler, Robert LZ Hoye, Karl C. Gödel, Thomas Bein, Pablo Docampo, Siân E. Dutton, Michael F. L. De Volder, and Richard H. Friend. *Nano letters*, 15,**2015**, 6095-6101.

9) Xing, Guichuan, Nripan Mathews, Swee Sien Lim, Natalia Yantara, Xinfeng Liu, Dharani Sabba, Michael Grätzel, Subodh Mhaisalkar, and Tze Chien Sum. *Nat. Mater*, 13, **2014**, 476-480.

10) Kim, Young-Hoon, Himchan Cho, Jin Hyuck Heo, Tae-Sik Kim, NoSung Myoung, Chang-Lyoul Lee, Sang Hyuk Im, and Tae-Woo Lee. *Advanced Materials*, 27,**2015**, 1248-1254.

11) Tan, Zhi-Kuang, Reza Saberi Moghaddam, May Ling Lai, Pablo Docampo, Ruben Higler, Felix Deschler, Michael Price, Aditya Sadhanala, Luis M. Pazos, Dan Credgington, Fabian Hanusch, Thomas Bein, Henry J. Snaith Richard H. Friend *Nature nanotechnology*, 9,**2014**, 687-692.

12) Cho, Himchan, Su-Hun Jeong, Min-Ho Park, Young-Hoon Kim, Christoph Wolf, Chang-Lyoul Lee, Jin Hyuck Heo, Aditya Sadhanala, NoSung Myoung, Seunghyup Yoo, Sang Hyuk Im, Richard H. Friend and Tae-Woo Lee *Science*, 350, **2015**, 1222-1225.

- 13) Ling, Yichuan, Zhao Yuan, Yu Tian, Xi Wang, Jamie C. Wang, Yan Xin, Kenneth Hanson, Biwu Ma, and Hanwei Gao. *Advanced Materials* 28, **2016**, 305-311.
- 14) Byun, Jinwoo, Himchan Cho, Christoph Wolf, Mi Jang, Aditya Sadhanala, Richard H. Friend, Hoichang Yang, and Tae-Woo Lee. *Advanced Materials*, **2016**, DOI: 10.1002/adma.201601369.
- 15) Wong, Andrew Barnabas, Minliang Lai, Samuel Wilson Eaton, Yi Yu, Elbert Lin, Letian Dou, Anthony Fu, and Peidong Yang. *Nano letters*, 15, **2015**, 5519-5524.
- 16) Tanaka, Kenichiro, Takayuki Takahashi, Takuma Ban, Takashi Kondo, Kazuhito Uchida, and Noboru Miura. *Solid state communications* 127, **2003**, 619-623.
- 17) Green, Martin A., Anita Ho-Baillie, and Henry J. Snaith. *Nature Photonics* 8, **2014**, 506-514.
- 18) Li, Xiong, Dongqin Bi, Chenyi Yi, Jean-David Décoppet, Jingshan Luo, Shaik Mohammed Zakeeruddin, Anders Hagfeldt, and Michael Grätzel. *Science*, **2016**, DOI: 10.1126/science.aaf8060.
- 19) Liu, Mingzhen, Michael B. Johnston, and Henry J. Snaith. *Nature*, 501, **2013**, 395-398.
- 20) Bansode, Umesh, Rounak Naphade, Onkar Game, Shruti Agarkar, and Satischandra Ogale. *The Journal of Physical Chemistry C* 119, **2015**, 9177-9185.
- 21) Jeon, Nam Joong, Jun Hong Noh, Young Chan Kim, Woon Seok Yang, Seungchan Ryu, and Sang Il Seok. *Nature materials*, 13, **2014**, 897-903.
- 22) Abate, Antonio, Michael Saliba, Derek J. Hollman, Samuel D. Stranks, Konrad Wojciechowski, Roberto Avolio, Giulia Grancini, Annamaria Petrozza, and Henry J. Snaith. *Nano letters*, 14, **2014**, 3247-3254.
- 23) Chen, Qi, Huanping Zhou, Ziruo Hong, Song Luo, Hsin-Sheng Duan, Hsin-Hua Wang, Yongsheng Liu, Gang Li, and Yang Yang. *Journal of the American Chemical Society*, 136, **2013**, 622-625.

- 24) Zhang, Wei, Michael Saliba, David T. Moore, Sandeep K. Pathak, Maximilian T. Hörantner, Thomas Stergiopoulos, Samuel D. Stranks et al. *Nature communications*, 6, **2015**,
- 25) Noh, Jun Hong, Sang Hyuk Im, Jin Hyuck Heo, Tarak N. Mandal, and Sang Il Seok. *Nano letters*, 13, **2013**, 1764-1769.
- 26) Kumawat, Naresh K., Amrita Dey, Aravindh Kumar, Sreelekha P. Gopinathan, K. L. Narasimhan, and Dinesh Kabra. *ACS applied materials & interfaces*, 7, **2015**, 13119-13124.
- 27) Sadhanala, Aditya, Felix Deschler, Tudor H. Thomas, Siân E. Dutton, Karl C. Goedel, Fabian C. Hanusch, May L. Lai *The journal of physical chemistry letters* 5, **2014**, 2501-2505.
- 28) H.J. Ledon, *Org. Synth.*, **1979**, 59, 66-69.
- 29) Zhi-Chuan Xu, Cheng-Min Shen, Tian-Zhong Yang, Huai-Ruo Zhang, Hu-Lin Li, Jian-Qi Li, Hong-Jun Gao, *Chemical Physics Letters*, **2005**, 415 342-345.
- 30) Naresh K. Kumawat, Amrita Dey, Aravindh Kumar, Sreelekha P. Gopinathan, K. L. Narasimhan, and Dinesh Kabra, *ACS applied materials and interfaces*, **2015**, 13119-13124.
- 31) De Wolf, Stefaan, Jakub Holovsky, Soo-Jin Moon, Philipp Löper, Bjoern Niesen, Martin Ledinsky, Franz-Josef Haug, Jun-Ho Yum, and Christophe Ballif. *The journal of physical chemistry letters*, 5, **2014**, 1035-1039.

Chapter 6

Summary and Future work

In this chapter we present the closing comments on the work presented in this thesis. Towards end, we present new approaches for future work in this exciting field of research.

6.1 Summary

The need for energy production using renewable resources is currently explored worldwide. The demand and the growth of human kind has made scientist to extensively investigate the alternate clean and renewable energy sources. Solar energy has tremendous potential in the current era. The use of solar energy offers environmentally friendly solutions and sustained growth. Currently in the photovoltaic (PV) technology the high efficiency silicon solar cells offers the large scale implementations. However, this technology is relatively expensive and therefore a new approach for cheaper PV systems using solution processible routes is currently under investigation. In parallel the growth of nanotechnology field has offered interesting solutions and hence variety of new concepts and design of solar cell devices have emerged out.

The research in optoelectronic devices is currently aimed at making high efficiency low cost solar cells and highly luminescent light emitting diode (LED) based devices. Functional inorganic oxides and organic-inorganic hybrid perovskites based systems clearly offer promising solution with an added advantage of low temperature processing conditions.

In this thesis we have presented use of metal nanoparticles loaded one dimensional nanostructure for applications in the field dye sensitized solar cells. We have also shown the novel approach of solvent-solvent extraction for the synthesis of organic inorganic perovskites based nanostructures with unusual optical properties. Later we have demonstrated a simple and easily scalable method to produce highly luminescent perovskite thin films which was used for light emitting diode applications.

Summary of each topic

1. In our first research work, we have synthesized gold (Au) nanoparticles loaded TiO₂ nanofibers using electrospinning method. Later these nanofibers were characterized for structural and optical properties. We have used these nanofibers as light harvesting agent in Dye sensitized solar cell architecture. we have

discussed the role of plasmonic light harvesting in dye sensitized solar cells (DSSC). Au loaded TiO₂ nanofibers have shown promising results in terms of light harvesting ability in DSSC. The presence of Au nanoparticles contributed in enhancement in efficiency by 25%. However the only TiO₂ nanofibers have achieved only 12% increment in efficiency. The IPCE and impedance study of these devices showed commensurate results. Impedance study of devices has demonstrated decrease in transport resistance and increment in chemical capacitance of DSSC solar cell. The systematic optical analysis of photoanodes prepared using Au NF and TiO₂ NF as scattering layer revealed the role of surface plasmon polariton modes distributed at the nanoscale schottky junctions in Au-TiO₂ nanofibers.

2. In the second piece of work, We have explored the novel idea of electrospray process in liquid bath as collector. Here we used the advantage of solvent-solvent extraction process for synthesis of low dimensional organic inorganic perovskite quantum nanostructures. We carried out the electrospray process of perovskite precursor solutions in toluene bath which contained oleylamine as capping agent. In the case of MAPbI₃ based systems, we observed the formation of two dimensional nanosheets of perovskites. The as synthesized perovskite was mainly stabilized in layered structure with oleylamine as intercalating agent. Later we explored the same method for MAPbBr₃ based perovskite precursor. In this, we observed formation of MAPbBr₃ based 0-D quantum dots and 2-D nanosheets. The optical properties of these as formed colloidal nanostructures have shown very high luminescence. Later we have demonstrated the tunability of optical band gaps in these perovskite systems by mixing the precursor solutions. In mixed halide case, these systems demonstrated the luminescence tunability over the broad range of visible spectrum. The structural and morphological characterization revealed the role of oleylamine in MAPbBr₃ and in MAPbI₃ based nanostructures.

3. In the third research work, we have explored the novel additive mediated solvent extraction approach. In this, we demonstrate the formation of perovskite thin film with high luminescence property and less electronic disorder. Here we have used quaternary alkyl ammonium salt as an additive which was dissolved in chloroform. Chloroform acts as an anti-solvent in this case. This salt solution was dripped over the perovskite film during formation process. The as obtained films had 250 times higher luminosity as compared to untreated films. We have also studied the electronic nature of this film by Photothermal deflection spectroscopy. PDS analysis revealed less electronic disorder in terms of Urbach energy which was reduced from 38meV to 18meV. Similarly photoluminescence quantum yield was enhanced from 1% to 30% after this treatment. Later we have demonstrated the use of such method to produce light emitting diode (LED). The LED's made using our approach showed external quantum efficiencies of 0.3% with narrow emission width maximum suggesting high color purity of the device.

6.2 Future work

During the course of the research work presented here several interesting and outstanding development in the field of optoelectronics have occurred on the international front. Recent advances in the field of organic-inorganic perovskites have certainly boosted the hopes to develop high efficiency PV panels at low cost compared to silicon technology. Due to interesting intrinsic properties of such semiconductors it has also shown promising applications in light emitting diode based devices and optical lasers as well. Based on the insight gained in past couple of years the following points appear important for further research in this field.

1. Recently the growth of **organic inorganic based hybrid perovskites** as light harvesting agent has shown promising efficiencies (above 20%) in last couple of years. Although high efficiencies are realized in short span of efforts, the

stability and sustainability of such solar cells is the important factor to address. Hence we see the following research opportunities in near future.

- a) The methods to optimize crystal growth of perovskites are very essential in terms of getting high efficiencies in devices. Various physical vapor deposition processes such as thermal evaporation, pulsed laser deposition are currently explored. These methods offer promising outcomes in recent time in terms of getting smooth uniform thin films of perovskites.
 - b) After recent development in stability of perovskite solar cells, use of 3D-2D mixed perovskites which are called as Ruddlesden- proper phases of perovskites for solar cell applications is of current interest. Synthesis of layered perovskite with novel functional amine based molecules along with methylammonium or formamidinium ion is of great scientific interest.
2. Hybrid organic inorganic perovskite possess excellent optoelectronic properties. The materials have potential to give a breakthrough performance in solar cells and light emitting diode applications. In this context, exploring the possibilities of novel additives to increase the photostability of perovskite thin films can be explored. Addition of small molecules which can effectively passivate the perovskite surface to improve the environmental stability. Understanding the role of crystal growth on perovskite solar cell performance is very important aspect from scientific and technological point of view.
 3. Solution phase growth of perovskite based low dimensional nanostructures such as quantum dots (QD), layered perovskites (nanosheets) have been explored in recent years. In this context, the use of antisolvent solvent extraction route offers very simple and easily scalable approach for the development of variety of perovskite low dimensional nanostructures. Exploring the various organic amine based molecules as an intercalation agent for tuning the photo-physical properties of perovskites is a matter of immediate scientific interest. Extending over this simple idea, the attempts has to be made in making smooth and uniform thin films composed of low dimensional perovskites. Good quality of thin films of these materials can be used in optoelectronic devices

In summary, we conclude that there are many research directions that have opened up due to recent progresses in terms of material choice, device engineering. All these scientific achievements offer the great promises in the clean energy sector. With the progress of research in optoelectronics along these lines we can hope a green and sustainable living for future generations.

List of Publications

1. **Rounak Naphade***, Satyawan Nagane, Shiva Shankar, Rohan Fernandes, Dushyant Kothari, Yuanyuan Zhou, Nitin Padture, Satishchandra Ogale*, Hybrid perovskite quantum nanostructures synthesized by electrospray antisolvent-solvent extraction and intercalation, *ACS applied Materials Interfaces*, **2016**, 854-861
2. **Rounak Naphade**, Mukta Tathavadekar, Jyoti Jog, Shruti Agarkar, Satishchandra Ogale*, Plasmonic light harvesting of Dye sensitized solar cells by Au-nanoparticle loaded TiO₂ nanofibers, *Journal of Material Chemistry A*, **2014**, 2(4), 975-984.
3. **Rounak Naphade**, Jyoti Jog, Electrospinning of PHBV/ZnO membranes: Structure and properties, *Fibers and Polymers*, **2012**, 13(6), 692-697.
4. Umesh Bansode, **Rounak Naphade**, Onkar Game, Shruti Agarkar, Satishchandra Ogale*, Hybrid Perovskite films by a new variant of Pulsed Excimer Laser Deposition: A Room-Temperature Dry process, *The Journal of Physical Chemistry C*, **2015**, 119 (17) 9177-9185.
5. Rupali Patil, Sarika Kelkar, **Rounak Naphade**, Satishchandra Ogale*, Low temperature grown CuBi₂O₄ with flower morphology and its composite with CuO nanosheets for Photoelectrochemical water splitting, *Journal of Material Chemistry A*, **2014**, 2(10), 3661-3668.
6. RK Bhosale, SA Agarkar, I Agrawal, **Rounak Naphade**, S Ogale* Nanophase CuInS₂ nanosheet/CuS composite grown by SILAR method leads to high performance as a counter electrode in dye sensitized solar cells, *RSC Advances*, 4 (42), **2014**, 21989-21996.
7. Badadhe, S. S., Suryawanshi, S. **Rounak Naphade**, R. A., Chaudhary, M. V., More, M. A., Shelke, M. V., & Ogale, S. B. Synthesis, microstructure, optical and field emission studies of iron vanadium oxide nanosheets. *Journal of Physics D: Applied Physics*, **2016**, 49(14), 145301.